

Measurement of Something

by

Kiyotaka Akabori

Submitted in partial fulfillment of the

requirements for the degree of

Doctor of Philosophy

at

Carnegie Mellon University

Department of Physics

Pittsburgh, Pennsylvania

Advised by Professor John F. Nagle
and Professor Stephanie Tristram-Nagle

July 17, 2014

Contents

1	Introduction	1
2	Structural Perturbation of Lipid Bilayers Due to Tat Peptide	3
2.1	Introduction	3
2.2	Materials and Methods	6
2.2.1	Stock Solutions	6
2.2.2	Thin Film Samples	6
2.2.3	Volume Measurements	7
2.2.4	X-ray setup	9
2.2.5	Analysis of Diffuse Scattering	9
2.2.6	Modeling the Bilayer Structure	15
2.2.7	Molecular Dynamics Simulation	21
2.3	Analysis of Molecular Dynamics Simulation Data	24
2.3.1	SIMtoEXP program	24
2.3.2	Local Thinning of Membranes	24
2.3.3	Lateral Decay Length of Membrane Thinning	26
2.4	Results	28
2.4.1	Bending and Bulk Modulus	28
2.4.2	Volume results	30
2.4.3	Electron Density Profile Modeling	31
2.4.4	Hard Wall Constrain Fits	41
2.4.5	Summary of Electron Density Profile Modeling	42
2.4.6	Molecular Dynamics Simulations	44
2.5	Discussion	53
2.6	Conclusion	56

3 Ripple Phase	58
3.1 Introduction	58
3.2 Materials and Methods	62
3.2.1 Sample Preparation	62
3.2.2 Instrumental Resolution	63
3.2.3 Low Angle X-ray Scattering Experiment	71
3.2.4 Near Grazing Incidence Wide Angle X-ray Scattering Experiment	72
3.2.5 Transmission Wide Angle X-ray Scattering Experiment	72
3.3 LAXS: analysis	77
3.3.1 Lattice Structure	77
3.3.2 Sample q-space	78
3.3.3 Lorentz Correction	80
3.3.4 Absorption Correction for LAXS	85
3.3.5 Correction due to mosaic spread	89
3.4 LAXS: model	93
3.4.1 Contour Part of the Form Factor	93
3.4.2 Transbilayer Part of the Form Factor	93
3.5 LAXS: results	97
3.6 nGIWAXS: results	103
3.6.1 Fluid and gel phase	103
3.6.2 Ripple phase	106
3.7 TWAXS: results	112
3.8 Discussion	117
3.9 Conclusion	120
Appendices	121
A	122
A.1 Mosaic Spread for NFIT analysis	122
A.1.1 Mosaic Spread: Calculation	122
A.1.2 Mosaic Spread: Near Equivalence of Two Methods	127
A.1.3 NFIT	130
A.2 More results from LAXS models	132
A.3 Derivation of the contour part of the form factor	134
A.4 Rotation of a Two-Dimensional Function	137

A.5	Derivation of the transbilayer part of the form factor in the 2G hybrid model	138
A.6	Correction due to refractive index	140
A.7	Thin Rod Model of the ripple phase	141

List of Tables

2.1	Some Amino Acids Data	8
2.2	Number of electrons per lipid and volume per lipid.	20
2.3	Some structural parameters for each component. n_i^e is the number of electrons and ρ_i is the average electron density.	20
2.4	Tat basic structural parameters. The notations are the same as in Table 2.3. $x_{\text{Tat}} = \text{Tat}/(\text{Tat}+\text{Lipid})$	20
2.5	Volume results at 37 °C	31
2.6	Fitting Results for DOPC membranes for the THG (Tat in headgroup) model. $z_{\text{PC}} - z_{\text{CG}} = 3.1 \text{ \AA}$ and $z_{\text{CG}} - z_{\text{HC}} = 1.3 \text{ \AA}$ in all fits.	32
2.7	Fitting Results for DOPC:DOPE (3:1) membranes for the THG model. $z_{\text{PC}} - z_{\text{CG}} = 3.1 \text{ \AA}$ and $z_{\text{CG}} - z_{\text{HC}} = 1.3 \text{ \AA}$ in all fits.	35
2.8	(Numbers are wrong) Fitting Results for DOPC:DOPE (1:1) membranes for the THG model. $\Delta z_1 = z_{\text{PC}} - z_{\text{CG}}$ and $\Delta z_2 = z_{\text{CG}} - z_{\text{HC}}$	35
2.9	Fitting Results of the bound THG model for DOPC membranes. $\Delta z_1 = z_{\text{PC}} - z_{\text{CG}}$ and $\Delta z_2 = z_{\text{CG}} - z_{\text{HC}}$	42
2.10	Comparison of the simulated form factors to the experimental form factors.	49
2.11	Summary of simulation results. $\langle D_{\text{PP}} \rangle$, phosphorus-phosphorus distance averaged over all lipids; D_{PP} , Tat-perturbed phosphorus atoms; x , thickness away from Tat; Δt , $\langle D_{\text{PP}}^{\text{DOPC}} \rangle - D_{\text{PP}}$; H_{Tat} , Tat height; R_{Tat} , radius of Tat cylinder; R_2 , radius of the calculated in-plane Tat-perturbed region; R_3 , effective radius of the simulation box.	50
2.12	Summary of weighted average results. The caption is the same as Table 2.11.	50

3.1	Lattice constants for DMPC at $T = 18.0$ °C reported by Wack and Webb [8] except the one colored in blue. The data collected and analyzed in this thesis are colored blue.	61
3.2	Beam divergence	63
3.3	Energy dispersion	64
3.4	Geometric broadening	70
3.5	Definitions of Z_{CH_2} and Z_{W}	95
3.6	Comparison of form factor obtained in two different methods. *Unoriented data are from Wack and Webb [8].	98
3.7	Observed intensity for $h = 1$ to 4 at $D = 57.8$, $\lambda_r = 145$, and $\gamma = 98.2^\circ$	99
3.8	Observed intensity for $h = 5$ to 9 at $D = 57.8$, $\lambda_r = 145$, and $\gamma = 98.2^\circ$ (continued from Table 3.7).	100
3.9	Model parameters. Fit1 and Fit2 were performed with the M1G model while Fit3 to 7 were with the M2G model. *Parameters were fixed to the values shown.	101
3.10	Ripple structural quantities.	101
3.11	Summary of peak properties	111
A.1	Form factors for $h = 1$ to 4	132
A.2	Form factors for $h = 5$ to 9	133

List of Figures

1.1	Experimental phase diagram of DMPC from Ref. [11].	2
2.1	LAXS of DOPC:DOPE (1:1) with $x_{\text{Tat}} = 0.034$ at 37 °C. White lobes of diffuse scattering intensity have large grey numbers, while lamellar orders and beam are shown to the left of the molybdenum beam attenuator (short, dark rectangle). q_z and q_r are the cylindrical coordinates of the sample q -space, where q_z -axis is along the bilayer normal and q_r -axis is along the in-plane direction. The lamellar repeat spacing was $D = 66.2 \text{ \AA}$	10
2.2	Schematic of an oriented stack of lipid bilayers. Thick green curves represent an instance of thermally fluctuating bilayers. The dashed lines show the thermally averaged positions $z = nD$ of the centers of each bilayer and $u_n(x, y)$ gives the instantaneous deviation from the average. Each bilayer extends in the $\mathbf{r} = (x, y)$ plane.	11
2.3	Expanded view of a fluctuating bilayer. Along the two black solid lines, the electron density profile is identical in an incompressible bilayer. Along the dashed line, the bilayer appears thicker by a factor $1/\cos \alpha$. This apparent thickness variation along the z direction is corrected by the undulation correction.	12
2.4	Schematic of DOPC showing each lipid component. The dash lines show where the lipid is divided into different components. The lipid headgroup is divided into two components, phophate-choline (PC) and carbonyl-glycerol (CG). The hydrocarbon chain region is also divided into two components, methylene+methine (CH_2+CH) and terminal methyl groups (CH_3).	16
2.5	A model electron density profile for DOPC with Tat.	17

2.6 Our simple model to extract the local bilayer thickness from simulation trajectories. Tat is modeled as a cylinder with its height H_{Tat} and radius R_{Tat} . The local thickness is defined as $D'_{\text{phos-phos}}$. The thickness of the unperturbed DOPC bilayer is $D_{\text{phos-phos}}$. Blue highlighted lipids fall within the imaginary cylinder extended from the Tat. Unperturbed lipids are highlighted in green.	25
2.7 Simple model of the lateral decay of the membrane thickness perturbation due to Tat.	27
2.8 Bilayer bending modulus, K_c , vs. Tat mole fraction x_{Tat} . D -spacings for DOPC/Tat mixtures varied from 64 to 68 Å, for DOPC/DOPE/Tat mixtures from 64 to 69 Å, for DOPC/DOPS/Tat (3:1) mixtures from 57 Å to 100 Å (pure DOPS was unbound), and for nuclear mimic/Tat mixtures from unbound (nuclear mimic) to 64 Å. Estimated uncertainty in all values is about ± 2	29
2.9 Form factors of lipid mixtures (arbitrarily scaled and vertically displaced) with increasing Tat mole fractions x_{Tat} indicated on figure legends. Lipid mixtures: A. DOPC B. DOPC/DOPE (3:1) C. DOPC/DOPE (1:1) D. DOPC/DOPS (3:1) E. Nuclear mimic. The entire q_z range is shown in C, while others show partial ranges. Solid vertical lines indicate the q_z values where the form factors equal zero between the lobes of diffuse data.	30
2.10 The best fits to DOPC form factors (left) and the corresponding electron density profiles (right) with $x_{\text{Tat}} = 0, 0.016, 0.034$, and 0.059 (from top to bottom).	33
2.11 The best fits to DOPC:DOPE (3:1) form factors (left) and the corresponding electron density profiles (right) with $x_{\text{Tat}} = 0, 0.016, 0.034$, and 0.059 (from top to bottom).	34
2.12 The best fits to DOPC:DOPE (1:1) form factors (left) and the corresponding electron density profiles (right) with $x_{\text{Tat}} = 0, 0.016, 0.034$, and 0.059 (from top to bottom).	36
2.13 Modeling results for absolute electron density profiles and for the Tat location as a function of distance z along the bilayer normal. A. DOPC B. DOPC:DOPE (3:1), and C. DOPC:DOPE (1:1).	37

2.14 A. Bilayer thickness, D_{PP} ; B. Bilayer thickness, D_{HH} ; C. Area/lipid, A_L ; D. Twice the Tat location, $2z_{\text{Tat}}$: all plotted vs. Tat mole fraction x_{Tat} . Error bars are standard deviations from imposing Tat Gaussian widths, $\sigma_{\text{Tat}} = 2.5, 3.0$ or 3.5 \AA . Inverted blue triangles connected with dotted line are results from MD simulations, averaging the best fits to the X-ray data for each parameter, with standard deviations shown.	39
2.15 χ^2 as a function of z_{Tat} for DOPC, DOPC:DOPE (3:1), and DOPC:DOPE (1:1) (from left to right) with $x_{\text{Tat}} = 0.016, 0.034$, and 0.059 (from top to bottom). $\sigma_{\text{Tat}} = 3.0$. The THG model (black squares) and the THC model (red circles).	40
2.16 χ^2 as a function of z_{Tat} for DOPC with $x_{\text{Tat}} = 0.016, 0.034$, and 0.059 (from top to bottom). $\sigma_{\text{Tat}} = 3.0$. The bound THG model was used.	43
2.17 DPP graph with bound fits	44
2.18 DHH graph with bound fits	44
2.19 AL graph with bound fits	44
2.20 zTat graph with bound fits	44
2.21 MD simulated form factors for DOPC at $A_L = 68 \text{ \AA}^2$ (blue solid line), 70 \AA^2 (red solid line), and 72 \AA^2 (green solid line) compared to the experimental form factor (open circles) scaled vertically to best match the form factor for 70 \AA^2	45
2.22 The simulated, symmetrized electron density profile for DOPC at $A_L = 70 \text{ \AA}^2$ as a function of the distance away from the bilayer center. Each component profile is labeled with its name: PC (phosphate-choline), CG (carbonyl-glycerol), CH ₂ +CH (methylene-methine combination), CH ₃ (terminal methyl). The sum of all the components is labeled as total.	46
2.23 MD simulated form factors for DOPC with $x_{\text{Tat}} = 0.015$ at $A_L = 72 \text{ \AA}^2$ (top) and 74 \AA^2 (bottom), with $z_{\text{Tat}} = 18 \text{ \AA}$ (red solid lines), 16 \AA (green solid lines), and 14 \AA (blue solid lines) compared to the experimental form factor (open circles) scaled vertically to best match the form factor for $z_{\text{Tat}} = 18 \text{ \AA}$	47

2.24 MD simulated form factors for DOPC with $x_{\text{Tat}} = 0.030$ at $A_L = 74 \text{ \AA}^2$ (top) and 76 \AA^2 (bottom), with $z_{\text{Tat}} = 18 \text{ \AA}$ (red solid lines), 16 \AA (green solid lines), and 14 \AA (blue solid lines) compared to the experimental form factor (open circles) scaled vertically to best match the form factor for $z_{\text{Tat}} = 18 \text{ \AA}$	48
2.25 Electron density profiles of guanidinium groups from the four best matched simulations for DOPC with $x_{\text{Tat}} = 0.015$ (one Tat on each leaflet). Tat on the lower and upper leaflets are shown on the left and right plots, respectively.	51
2.26 MD simulated form factors (red solid lines in A and C) of Tat/(DOPC+Tat), $x_{\text{Tat}}=0.030$, with Tat fixed at $z_{\text{Tat}}= 18 \text{ \AA}$ (panel A) and 5 \AA (panel C) from the bilayer center compared to experimental form factors (open circles) scaled vertically to provide the best fit to the simulations. Corresponding snapshots are shown in Panels B and D in which the lipid chains are represented as grey sticks on a white background, Tats are yellow, phosphate groups are red and water is blue.	52
2.27 Location of Tat in DOPC bilayer. Tat is represented as a cylinder, z is the distance from the bilayer center, and R is the in-plane distance from the center of Tat. The average z of the lipid phosphates as a function of R and the arginine guanidiniums are shown in red and blue, respectively.	53
3.1 Lattice structure of the asymmetric ripple phase. Unit cells are shown in dash lines. Center of bilayers are shown by thick, solid lines. Notations in the figure are (\mathbf{a} and \mathbf{b} : lattice unit vectors), (D : D -spacing along z), ($\lambda_r = \mathbf{b} $: ripple wavelength), (γ : oblique tilt angle), (A : ripple amplitude), (ψ : chain tilt angle with respect to the z direction), and (x_M : projected length of the major arm).	59
3.2 Pictures of an annealing chamber	62
3.3 The horizontal profile of the beam used in the 2013 low resolution study. Each pixel was 0.07113 mm, which gave a CCD angular resolution $\Delta\theta$ of 0.0057° , corresponding to $\Delta q = 0.0011 \text{ \AA}^{-1}$ at the sample to detector distance of 359.7 mm. The beam FWHM = 1.7 pixels, giving $\Delta\theta = 0.010^\circ$ or $\Delta q = 0.0019 \text{ \AA}^{-1}$	65

3.4	The vertical profile of the beam used in the 2013 low resolution study. The beam height = 15 pixels = 1.1 mm.	65
3.5	In-plane geometric broadening due to the sample width w_s and the beam width Δx_{beam} . A top view of the sample (green) on the Si wafer (gray) and the incoming and diffracted X-rays (bounded by red solid lines) are shown. The total in-plane scattering angle for a lipid chain-chain correlation is labeled as 2θ , and the geometric broadening as Δx	67
3.6	The horizontal profile of the beam used in the 2013 high resolution experiment. The CCD angular resolution $\Delta\theta = 0.0092^\circ$ corresponding to $\Delta q = 0.0017 \text{ \AA}^{-1}$, at the sample to detector distance of 220.6 mm. The beam FWHM = 3.7 pixels = 0.26 mm, giving $\Delta\theta = 0.034^\circ$ or $\Delta q = 0.0063 \text{ \AA}^{-1}$	67
3.7	The vertical profile of the beam used in the 2013 high resolution experiment. The beam height = 9 pixels = 0.64 mm.	68
3.8	Geometric broadening in TWAXS	69
3.9	Top and side view of the beam on the sample in TWAXS	70
3.10	Projection of rectangular beam on the detector. Scattered beam appears as a parallelogram on the CCD.	70
3.11	(top panels) CCD images of X-ray scattering taken with (left) and without (right) a nominally 25 μm thick Mo attenuator. These data were taken at a fixed angle of incidence $\omega = 0.8^\circ$. The sample was an oriented film of DOPC:DOPE (3:1) in the fluid phase at 37 °C. The wavelength was 1.175 \AA , the same as the one used for the ripple phase experiment. The same gray scale is used in both images. 100 pixel = 0.11 \AA^{-1} in q . A small dot located about $(p_x, p_z) = (520, 170)$ between the first and second orders is a specular reflection from the substrate. The exposure times were 1 second. (bottom panels) Vertical p_z slices of the X-ray images shown in the top panels (left). The scattering intensity measured with the attenuator (red solid circles) was multiplied by a factor of 6.9 and compared to the intensity measured without the attenuator (black solid circles, right).	73

3.12 1 second exposure (left) and 60 second exposure (right) of the low angle X-ray scattering from the DMPC ripple phase in gray log scales. The index h is labeled in green. $(3, k)$ reflections are identified in cyan. The shadow cast by 100 μm thick molybdenum attenuator blocking strong $(1,0)$ and $(2,0)$ orders in the right image is labeled as attenuator and extends from $q_z = 0 \text{ \AA}^{-1}$ to 0.2 \AA^{-1} . $D = 57.8 \text{ \AA}$, $\lambda_r = 145.0 \text{ \AA}$, and $\gamma = 98.2^\circ$.	74
3.13 Schematics of the sample holder in the transmission mode. Side (left) and top (right) views are shown. The thickness of the Si wafer = 35 μm . The thickness of the sample $\approx 10 \mu\text{m}$. The distance between the axis of rotation and sample = 21.1 mm.	75
3.14 Circular path followed by the sample as the angle of incidence ω was changed. The sample to detector distance and D -spacing of the sample were measured in the LAXS mode, where $\omega = 1^\circ$. WAXS images were collected at the transmission mode, where $\omega = -45^\circ$. The z position of the sample was slightly higher at the LAXS mode than at the transmission mode, so the sample holder was vertically shifted for different modes.	76
3.15 Picture of the sample holder looking from above. A lead tape was attached to the back of the sample holder to help reduce the background scattering, typically coming from the air gap between the flightpath snout and the mylar window of the chamber.	76
3.16 Experimental reflectivity geometry.	79
3.17 Ewald sphere construction for the ripple phase diffraction in the low angle regime. A ripple $k = 0$ peak is the solid, black circle on the q_z -axis. A ripple $k \neq 0$ ring is the black ring centered about the q_z -axis. The portion of the ring that is inside the Ewald sphere is shown as a red dashed line and the portion of the ring that is outside but behind the Ewald sphere is shown as a black dotted line. The magnitude of the total scattering angle is exaggerated. With a wavelength of 1.175 \AA , the magnitude $ \mathbf{k}_{\text{in}} = 5.35 \text{ \AA}^{-1}$. For a $h = 5$ peak, $q_{50}^z = 0.54 \text{ \AA}^{-1}$, one tenth of k_{in} .	81
3.18 Side view of an arc of $k = 0$ peak shown as a thick blue line.	82

3.19	<i>q</i> -space representations of Bragg peaks and Bragg rings for $h = 1$ and 2 and $k = 0, 1$, and 2 in q_{hk}^z planes. The intersection between the Ewald sphere and a Bragg peak/ring is indicated in red. The observed intensity for the $k \neq 0$ orders is proportional to the fraction of the length of red arcs in the circumference. This fraction is equal to one for $k = 0$ reflections. Because the reflections are not in the same q_z plane, the range of q_y integration indicated by the height of the gray rectangle is different for different h orders. For $\gamma \neq 90^\circ$, the range of q_y integration is slightly different for different k reflections with the same h . The values shown are for $D = 58 \text{ \AA}$, $\lambda_r = 145 \text{ \AA}$, $\gamma = 90^\circ$, and $\lambda = 1.175 \text{ \AA}$. The magnitude of curvature of arcs is exaggerated.	83
3.20	The path of X-rays within the sample. The incident angle is ω and the total scattering angle is 2θ . An X-ray with a penetration depth of z is shown. The total thickness of the sample is t . Refraction correction is smaller than what? for $\theta > 0.5^\circ$ ($h = 1$).	86
3.21	Absorption factors as a function of $q_z \approx 4\pi\theta/\lambda$. Values at $q_z = 2\pi h/D$ corresponding to $D = 57.8 \text{ \AA}$ are shown as squares. $\mu = 2600 \text{ \mu m}$, $t = 10 \text{ \mu m}$, and $\lambda = 1.175 \text{ \AA}$	88
3.22	Eq. (3.30) plotted as a function of ω for $\theta = \theta_B$	89
3.23	Contours of a mosaic spread distribution projected on the $\omega\chi$ -plane, where $\chi - \chi_{hk}$ is an angle measured from a (h, k) reflection on the detector ($\chi = \pi/2 - \phi$ in Fig. 3.16) and θ_{hk} is the Bragg angle for a (h, k) reflection. The distribution function takes a form of Lorentzian centered at $\alpha = 0$. Domains with $\alpha = 0$ are probed at $\omega = \theta_{hk}$ and $\chi = \chi_{hk}$. Integrated intensity of $(1, k)$ reflection arises from domains in the green shaded area while that of $(3, k)$ reflection is from the blue shaded area, which is three times larger.	90
3.24	Mosaic factor given by Eq. (3.37) as a function of $q_z \approx 4\pi\theta/\lambda$	92
3.25	title goes here	94
3.26	Electron density profile calculated using the phases obtained from the M2G model and experimental form factors	102
3.27	Electron density profile calculated using the phases obtained from the M2G model and experimental form factors	102
3.28	Transformation of wide angle scattering data from the CCD to <i>q</i> -space	104

3.29 Fluid phase WAXS plotted along q_r at $q_z = 0.012 \text{ \AA}^{-1}$. The red solid line is a Lorentzian fit with its FWHM equal to 0.288 \AA^{-1} , centered at $q_r = 1.408$. Extra intensity at larger q_r was due to water scattering, which led to a slightly asymmetric profile.	105
3.30 nGIWAXS of the DMPC gel phase	106
3.31 High resolution nGIWAXS of the DMPC ripple phase for $D = 60.8 \text{ \AA}$. The angle of incidence ω was 0.2° . The stronger peak was at $(q_r, q_z) \approx (1.478 \text{ \AA}^{-1}, 0.20 \text{ \AA}^{-1})$. The weaker peak was at $(q_r, q_z) \approx (1.452 \text{ \AA}^{-1}, 0.12 \text{ \AA}^{-1})$. The scattered intensity along the line slightly above $q_z = 0 \text{ \AA}^{-1}$ is the Vineyard-Yoneda peak [106, 107].	108
3.32 q_r swaths of the ripple WAXS, each averaged over 0.02 \AA^{-1} in q_z . Each curve is shifted by 100 vertically. The central q_z values of swaths are shown in the figure legend.	109
3.33 nGIWAXS of the DMPC ripple phase for $D = 59.2 \text{ \AA}$ (left) and difference between $D = 59.2 \text{ \AA}$ and 60.8 \AA (right). The difference shows no obvious feature, indicating that the ripple WAXS patterns at the two D-spacing were identical within an error. The angle of incidence ω was 0.2° . The data were taken with the high resolution setup.	110
3.34 Peak profile in q_r at $q_z = 0.2 \text{ \AA}^{-1}$ fitted to double Lorentzian functions	110
3.35 Peak profile in q_r at $q_z = 0.12 \text{ \AA}^{-1}$ fitted to double Lorentzian (left) and double pseudo Voigtian functions (right)	111
3.36 Transmission WAXS of the DMPC gel phase	113
3.37 TWAXS image of the DMPC ripple phase	114
3.38 q_r swath of the ripple TWAXS averaged between 0.11 \AA^{-1} and 0.13 \AA^{-1} in q_z . Asymmetric shape of the profile is due to two Bragg rods centered at different q_r values as discussed in Sec. 3.6.	115
3.40 q_z swath averaged between 1.465 \AA^{-1} and 1.481 \AA^{-1} (left) and between 1.465 \AA^{-1} and 1.51 \AA^{-1} (right) in q_r . The left plot is approximately the q_z profile along the weaker peak while the right profile extends over the entire ripple WAXS pattern.	116
3.41 Comparison of the ripple (black) and fluid (red) phase WAXS at $q_z = 0.012 \text{ \AA}^{-1}$. The fluid phase data were taken with the low resolution setup and scaled vertically to enable visual comparison.	118

A.1	Two dimensional view of mosaic spread (left) and notations used in this section (right). The stacking direction of an ideal domain is \mathbf{n} and that of a tilted domain \mathbf{n}' . The deviation of \mathbf{n}' from \mathbf{n} denoted as α quantifies the degree of misorientation of a domain. The x , y , and z -axes are the sample coordinates.	123
A.2	Example of a two dimensional sample consisting of an ideal and tilted domains. $\mathbf{q} = (q_x, q_z)$ is the sample q -space and $\mathbf{q}' = (q'_x, q'_z)$ is the domain q -space. The two q -spaces are related by a rotation of α about the y -axis, which is into the page.	125
A.3	Notations used in this section. The arc originating from the Z -axis is the mosaic arc due to the mosaic spread distribution.	128
A.4	Rocking scan trace in q -space.	129
A.5	Unit cell for chain packing in the major arm	142

Chapter 1

Introduction

Lipids are amphiphilic molecules, consisting of hydrophilic headgroup and hydrophobic chains. There are various kinds of lipids. These can be categorized in terms of headgroup, chain length, and chain saturation.

In water lipids self-assemble into lipid bilayers to shield their hydrophobic cores. Lipid bilayers are the building blocks of cell membranes. Lipid bilayers display a wide variety of thermodynamic phases as a function of temperature and hydration. Figure 1.1 shows a generic phase diagram of phosphatidylcholines (PC). At full hydration, a lamellar phase coexists with excess water. PC lipids constitute a substantial fraction of mammalian cell membranes and have been studied for many decades. In the high temperature, fluid L_α phase, the hydrocarbon chains are conformationally disordered, and intra-membrane molecular correlations are liquid-like [1]. In the low temperature, gel L'_β phase, hydrocarbon chains are stiff and tilted with respect to the membrane normal [2]. Between the fluid and gel phases appears a structurally modulated or rippled membrane phase. This phase has been detected in several lipids (REF: cite as many lipids as possible). The low angle diffraction pattern of this phase conforms to the symmetry of a 2D monoclinic lattice. This phase was termed P'_β and is commonly called the ripple phase. The topography of the membrane ripples has been directly visualized by freeze fracture electron microscopy experiments [3–7]. The wavelength of the modulation is about 140 Å for dimyristoylphosphatidylcholine (DMPC), which has 14 carbons in the hydro carbon chains [8]. There was evidence that molecular conformation in the ripple phase is not unique. NMR signals in the ripple phase [9] were consistent with a superposition of signals observed in the fluid and gel phases. Lateral diffusion measurements found two distinct populations, with

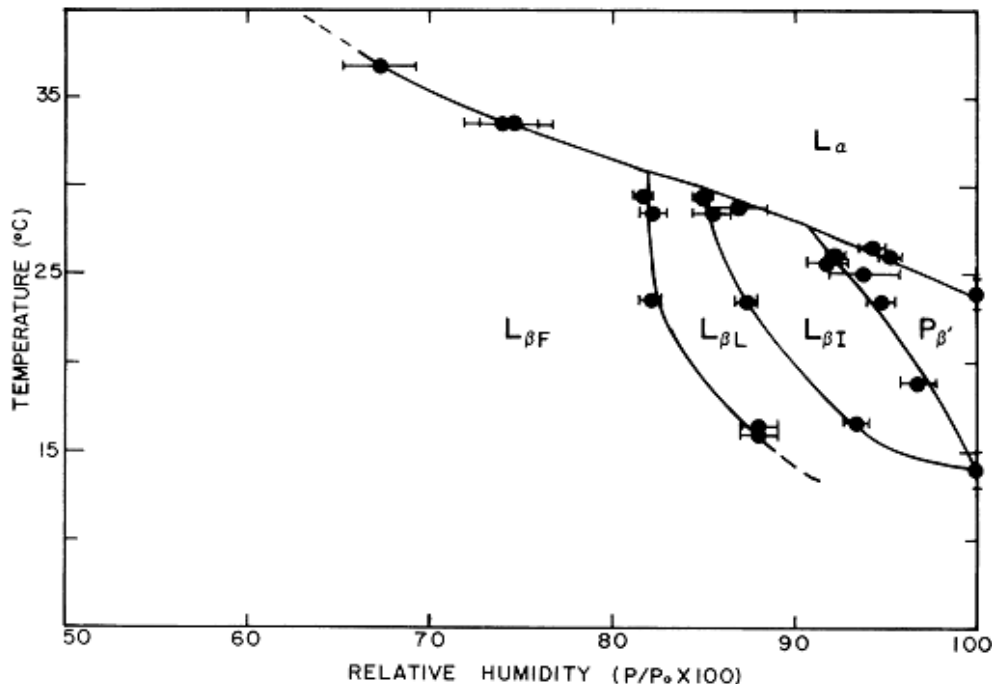


Figure 1.1: Experimental phase diagram of DMPC from Ref. [11].

diffusion coefficients characteristic of fluid and gel phases [10].

At higher temperature, lipids are in fluid phase. In this phase, chains are flexible. Lipid bilayers are also flexible and fluctuating. This flexibility of lipid bilayers make many interesting biological phenomena possible.

As the temperature is reduced, lipid bilayers go into the gel phase. In this phase, chains are straightened out and bilayers are rigid.

Between the fluid and gel phases, some lipids have the ripple phase. This phase is found in saturated lipids. In this phase, the bilayer height is modulated in a periodic manner in the in-plane direction. Each bilayer is registered along its orthogonal direction.

In this thesis, we focus on the fluid and ripple phase. In the former phase, we investigated the interaction of a peptide called Tat with lipid bilayers in the fluid phase. Tat is discussed in chapter 3. Regarding the ripple phase, we measured the electron density profile of the lipid bilayers using a stack of oriented bilayers. Using wide angle x-ray scattering technique, we also investigated the chain packing within a bilayer. The ripple phase is discussed in chapter 4. The appendices show a lot of details that will allow other people to reproduce much of the results shown in this

thesis as well as help readers understand scattering analysis employed in this work. It is my hope that these details will help future researchers, especially students, understand some of the techniques to investigate the structure of lipid bilayers in sub Angstrom resolution.

Chapter 3

Ripple Phase

When the temperature is reduced from the fluid phase, the ripple phase is observed in bilayers consisting of DMPC and DPPC lipids. This chapter discusses X-ray scattering experiments on the ripple phase formed by dimyristolphosphatydylcholine (DMPC) bilayers.

3.1 Introduction

(At some point, do some literature search and write up this section) The ripple phase has been a fascinating thermodynamic phase to many physicists and physical chemists since its discovery. It was originally observed in calorimetry study for alkanes by sturevant. Although this phase has never been reported to occur in a biologically relevant situation, it provides an interesting opportunity to study fundamental lipid interactions and their influence on the bilayer shape. (Let's find some recent papers and see if anyone says anything about biological relevance)

In the first structural study of this phase by Tardieu *et al.*, the X-ray diffraction pattern from DLPC was phased by a pattern recognition technique and the electron density map was calculated. It was shown that the structure corresponds to a 2D oblique unit cell shown in Fig. 3.1. The calculated electron density map showed that DLPC bilayers are height modulated and have a smooth, asymmetric shape. The ripple wavelength λ_r was reported to be 85.3 Å, the lamellar periodicity D 55.3 Å, and the oblique angle γ 110°. The electron density map reported the ripple amplitude $A = 15$ Å in DLPC.

Various experiments have indicated the existence of two types of ripple phases: the

stable asymmetric and the metastable symmetric phase. In the asymmetric phase, a plane of reflection perpendicular to the ripple wave vector is absent. The metastable symmetric phase has been seen in DPPC bilayers, but not in DMPC.

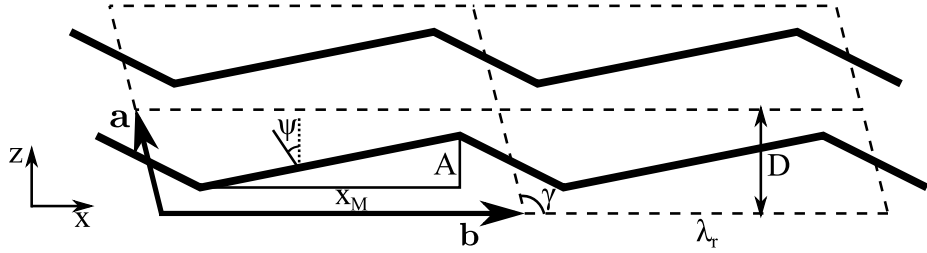


Figure 3.1: Lattice structure of the asymmetric ripple phase. Unit cells are shown in dash lines. Center of bilayers are shown by thick, solid lines. Notations in the figure are (**a** and **b**: lattice unit vectors), (D : D -spacing along z), ($\lambda_r = |\mathbf{b}|$: ripple wavelength), (γ : oblique tilt angle), (A : ripple amplitude), (ψ : chain tilt angle with respect to the z direction), and (x_M : projected length of the major arm).

The equilibrium structure of the ripple phase has been extensively studied by X-ray diffraction [2,8,85–89], neutron diffraction [90,91], AFM [], freeze fracture electron microscopy [92], and freeze fracture scanning tunneling microscopy [] techniques. In the scanning tunneling microscopy experiment [7], the three-dimensional contours of the ripple phase $P_{\beta'}$ of dimyristoylphosphatidylcholine (DMPC) were imaged, and a ripple wavelength of 130 Å and an amplitude of 45 Å were reported.

While many studies used multilamellar samples, the ripple phase was also found in unilamellar vesicles, where a vesicle has only one bilayer [93].

The ripple phase has been detected in a wide variety of lipids, including phosphatidylcholines, phosphatidylacetoyl (PA), and phosphatidylglycerol (PG), but no ripple phase has been observed in bilayers composed of PE headgroups. These studies suggest that the size of headgroup has something to do with the ripple formation.

From X-ray data of the DMPC ripple of unoriented samples, Wack and Webb [8] argued that the ripples have a sawtooth shape, but were unable to phase the observed pattern. Their X-ray form factor data were later phased by employing a modeling and fitting technique by Sun *et al.* [88], and the electron density map was calculated, which indicated that the ripples indeed have a sawtooth shape. The map also showed that the major arm is about twice as long as the minor arm. The bilayer thickness was found to be larger than that of the minor arm. The value of the bilayer thickness in the major arm was comparable to the thickness of DMPC bilayers in the gel phase.

A structural investigation by X-ray diffraction of the ripple phase of oriented dipalmitoylphosphatidylcholine (DPPC) samples indicated that hydrocarbon chains are packed in a hexagonal lattice with chains tilted in the plane perpendicular to the ripple wave vector [94]. In that study, the oblique angle γ was found to be 90° . It is believed that the resolved structure was for the symmetric ripple, which has been shown to be thermodynamically metastable and whose occurrence depends on the sample history [95]. In [94], only symmetric ripple was observed in the low angle X-ray scattering, which seems to contradict with the metastability of this symmetric ripple.

Sengupta et al. [96] has investigated temperature dependence of the average structure of DMPC and concluded that there is no obvious change in the structure as a function of temperature. On the other hand, the ripple phase composed of POPC showed some variation in the average structure. Based on calculated electron density profiles and model parameters, they argued that chains in both major and minor arms are tilted with respect to the stacking z direction by the same amount and that chains are parallel to the local normal in the major arm. This argument was inconsistent with the findings in [88] that the thickness of major arm is almost identical to that of the gel phase where chains are tilted by $\sim 30^\circ$. To circumvent this discrepancy, Sengupta *et al.* speculated that chains might be titled by some amount into the direction perpendicular to the ripple direction. This type of information , however, is not well captured in low angle scattering data, and wide angle scattering is essential.

In a giant unilamellar vesicle composed of a mixture of DPPC and DOPC, co-existing domains of L'_β and P'_β have been found [97]. The P'_β domain had lower concentration of DPPC than the L'_β domain. Addition of anionic lipids (DOPG?) turned the gel phase domain into the ripple phase domains. The authors concluded that reduction of surface tension drove highly stressed gel phase to less stressed ripple phase.

AFM The ripple phase has also been observed in the top layer of solid supported double layers through atomic force microscopy (AFM). The effect of the bottom layer on the top layer in the ripple phase has not been thoroughly studied. It is not clear whether the structure of these ripple formation top layers is the same as that in a bulk sample such as MLVs and oriented samples.

A few MD (molecular dynamics) simulations have shed light on molecular organization in the ripple phase as well. de Vrie *et al.* [98] carried out atomistic simulations

resulting in an assymetric ripple where chains are gel-like in the major arm and interdigititated in the minor side. Coarse-grain simulations performed later essentially found the same results [99].

A theory developed by Chen *et al.* [100] has been successful in describing some features in the ripple phase. In this theory, the divergence of the tilt field of lipids are coupled to the curvature of the bilayer. Increase in the divergence of the lipid tilt is compensated by increase in the curvature, leading to the observed height modulated ripple phase. This theory predicted ripple phases with different symmetry for chiral and achiral lipids. Later, Katsaras and Raghunathan [101] carried out low angle X-ray scattering experiment on regular DMPC and achiral DMPC and found that there was no structural difference between them.

Raghunathan theory (2011)

Schmidt theory (2013)

D (Å)	λ_r (Å)	γ (deg)
55.0	159.4	99.0
57.0	140.8	97.6
57.3	151.6	97.8
57.4	148.4	97.6
57.5	144.1	97.8
57.5	141.9	98.0
58.0	140.1	98.2
57.8	145.0	98.2
58.0	141.7	98.4
59.8	129.6	97.3
60.6	130.1	97.0
61.5	130.8	96.5
62.4	122.0	95.9
63.9	123.1	94.9
64.9	120.3	92.3

Table 3.1: Lattice constants for DMPC at $T = 18.0$ °C reported by Wack and Webb [8] except the one colored in blue. The data collected and analyzed in this thesis are colored blue.

3.2 Materials and Methods

3.2.1 Sample Preparation

DMPC was purchased from Avanti Polar Lipids. Four mg DMPC powder was dissolved in 140 μl chloroform:methanol (2:1 v:v) mixture. The solution was plated onto silicon wafers following the rock and roll procedure [102]. See also Sec. 2.2.3. For all the ripple phase experiments, the temperature of the hydration chamber was set to 18 °C. In 2011 and 2012 synchrotron experiments, the samples were created and annealed more than a week in advance and stored in a refrigerator. The quality of these samples measured by their mosaic spread was found to worsen over time after the samples were annealed. Therefore, to attempt better quality, the samples were annealed for only about 12 hours just before the X-ray experiment. Figure 3.2 shows a picture of the annealing chamber. Annealing is promoted both by hydration and by elevated temperature. To achieve gentle but efficient hydration of a sample, filter papers were installed that exposed a larger surface for evaporation. The temperature was set to 60 °C. It must be emphasized that the annealing chamber should equilibrate in an annealing oven set to 60 °C, prior to putting a sample in the chamber. When a sample was put in the chamber sitting at a room temperature and then the system was placed inside the oven, warmer water vapor inside the chamber condensed on the cooler sample, causing so called flooding of oriented sample. A small drop of water on an oriented film is detrimental for the orientation quality because the entropy-driven formation of unilamellar vesicles causes oriented bilayers to peel off one by one.

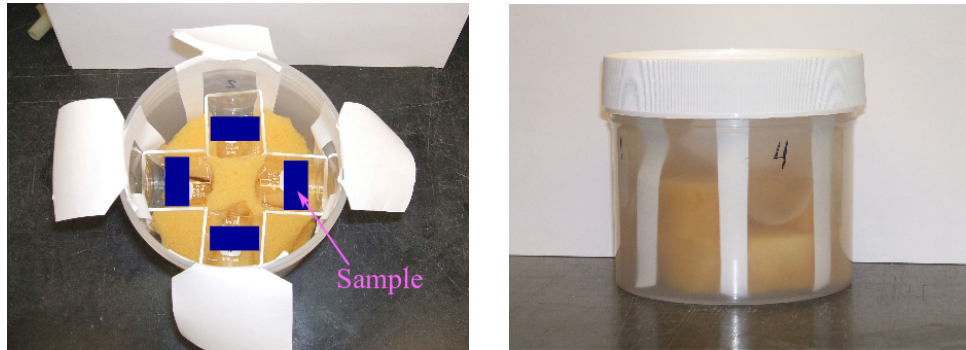


Figure 3.2: Picture of an annealing chamber.

The sample for the grazing incident wide angle study was prepared in the same way as for low angle study. In order to minimize the geometric broadening, the sample

was trimmed to 1 mm in width along the beam direction.

The sample for transmission study was deposited on a thin, 35 micron, silicon wafer, and oriented following the rock and roll procedure [102]. Because the wafer was very fragile, attaching the sample to a sticky thing was impossible. Instead, the sample was attached to a plastic cap on a small vial with a small amount of heat sink compound at a corner of the wafer. The wafer was stable enough for rocking.

3.2.2 Instrumental Resolution

The X-ray scattering experiments were carried out at the Cornell High Energy Synchrotron Source (CHESS) G1 station in three different runs (2011, 2012, and 2013). The low angle X-ray scattering (LAXS) data analyzed in this thesis were collected in 2013. The near grazing incidence wide angle X-ray scattering (nGIWAXS) data were also collected in the 2013 run, but with smaller energy dispersion than in the LAXS experiment. The transmission wide angle X-ray scattering (TWAXS) data were collected in the 2011 run. The ripple phase experiment in the 2012 run was not successful due to low sample quality. The instrumental resolution in these X-ray experiments depended on the beam divergence, energy dispersion, and geometric broadening.

3.2.2.1 Divergence

The beam divergence quantifies an angular spread of the incoming X-ray beam. We estimated the beam divergence by measuring the horizontal and vertical beam widths at two known sample-to-detector S distances with difference ΔS . The beam widths were larger at the further distance, which indicated that the beam was divergent. We calculated the divergence as $\text{div} = \Delta B / \Delta S$, where ΔB is the difference in beam widths at different S distances. Table 3.2 summarizes beam divergence.

year	type of experiment	horizontal (rad.)	vertical (rad.)
2013	LAXS	4.2×10^{-5}	1.6×10^{-4}
2013	nGIWAXS	4.2×10^{-5}	1.6×10^{-4}
2011	TWAXS	2.5×10^{-5}	5×10^{-5}

Table 3.2: Beam divergence

3.2.2.2 Energy dispersion

A W/B₄C multilayer monochromator with energy bandwidth $\Delta E/E$ of 1.3% was used in the LAXS and TWAXS experiments. The energy of the X-ray beam was 10.55 keV, corresponding to a wavelength λ of 1.175 Å, in the LAXS experiment. To achieve a higher instrumental resolution than that for the LAXS experiment, a (111) silicon monochromator was used for the nGIWAXS experiment, which gave $\Delta E/E$ of 0.01%. Due to the geometry of the G1 station, the Si monochromator was placed in the G1 hutch, in series with the multilayer monochromator. Table 3.3 summarizes energy dispersion.

year	type of experiment	$\Delta E/E$ (%)	E (keV)	λ (Å)
2013	LAXS	1.5	10.55	1.175
2013	nGIWAXS	0.01	10.55	1.175
2011	TWAXS	1.5	10.54	1.176

Table 3.3: Energy dispersion

3.2.2.3 Geometric Broadening

The beam footprint on the sample has a finite size and this causes geometric broadening of diffraction peaks on the CCD detector.

LAXS In the LAXS experiment, the geometric broadening in the horizontal x direction is simply the horizontal beam width for $k = 0$ peaks with minor additional broadening for $k \neq 0$ peaks. Geometric broadening in the vertical z direction is due to different heights of the sample along the y direction of the beam at non zero angle of incidence ω . It is given approximately by $w_s \tan \theta$, where w_s is the sample width along the y direction and θ is the scattering angle. The beam shape, measured through a semi-transparent 200 µm thick molybdenum (Mo) beam stop, is shown in Fig. 3.3 and 3.4. The horizontal beam width was 1.7 pixels (0.12 mm). The vertical beam width was approximately 1 mm, tall enough to cover the entire sample if the sample was tilted between 0° and 11.5°. The sample was rocked during X-ray exposure between -1.6° and 7° in order to observe many diffraction peaks in one data collection and keep all the sample in the beam.

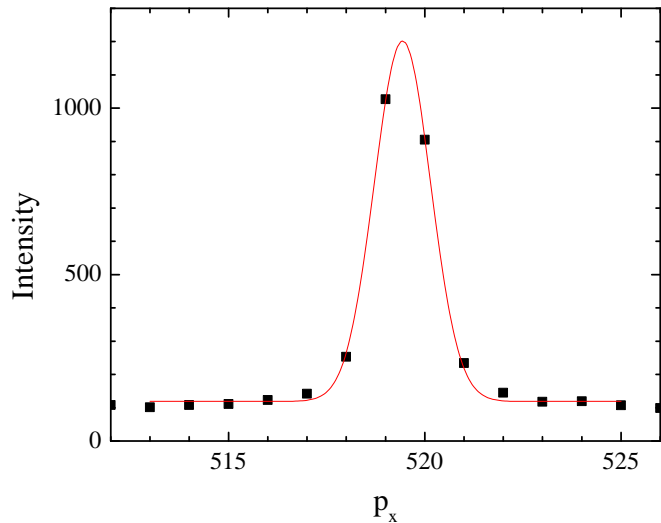


Figure 3.3: The horizontal profile of the beam used in the 2013 low resolution study. Each pixel was 0.07113 mm, which gave a CCD angular resolution $\Delta\theta$ of 0.0057°, corresponding to $\Delta q = 0.0011 \text{ \AA}^{-1}$ at the sample to detector distance of 359.7 mm. The beam FWHM = 1.7 pixels, giving $\Delta\theta = 0.010^\circ$ or $\Delta q = 0.0019 \text{ \AA}^{-1}$.

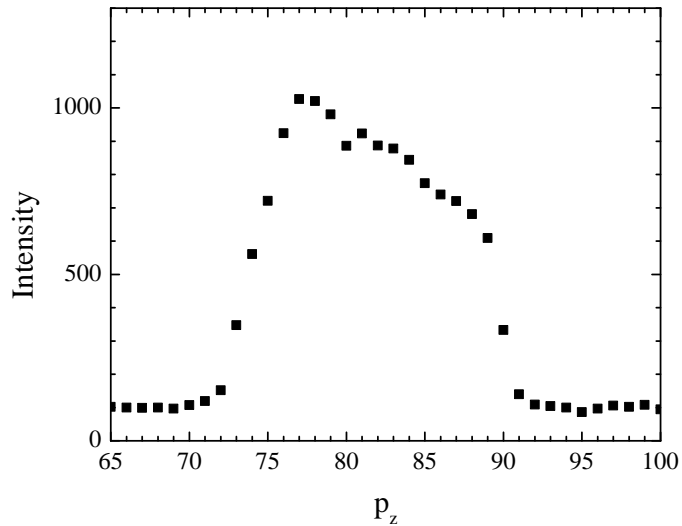


Figure 3.4: The vertical profile of the beam used in the 2013 low resolution study. The beam height = 15 pixels = 1.1 mm.

nGIWAXS In the nGIWAXS experiment, the horizontal geometric broadening was due to the sample width along the beam direction and the horizontal beam width. From the geometry of the experiment shown in Fig. 3.5, the geometric broadening Δx can be estimated, assuming simple additivity,

$$\Delta x = \Delta x_{\text{beam}} + w_s \tan(2\theta),$$

where θ is the in-plane scattering angle. The total scattering angle 2θ for the ripple WAXS was approximately 16° . To minimize the contribution to Δx from the sample, the sample was trimmed to $w_s = 1$ mm along the beam direction. This width was chosen because (1) I could not trim more without a more sophisticated device than a simple razor blade, (2) a very narrow sample would be a weak scattering body, and (3) disordering effect from the sample edge might become too significant to ignore. Given the above reasons and due to limited availability of synchrotron beam time, I considered a 1 mm width to be reasonable. The horizontal beam width was 4 pixels (0.28 mm) as shown in Fig. 3.6. With these experimental parameters, the resolution was estimated to be $\Delta x = 0.57$ mm = 8 pixels, which would be the unresolved width of an intrinsically infinitely sharp wide angle peak. [Comment and refer to the gel phase data shown in the result section of nGIWAXS.](#) The sample to detector distance were 220.6 mm, measured using silver behenate. Then, the minimum peak width measured in q -space would be $\Delta q \approx 0.014 \text{ \AA}^{-1}$. The vertical geometric broadening was negligible because the sample width w_s was narrow and scattering of interest occurred at small q_z .

TWAXS In the TWAXS experiment, geometric broadening in both x and z directions was non-negligible. To calculate the broadening, let us assume that the beam has a rectangular cross section with its height Y_b and width X_b as shown in Figure 3.8. When the sample is tilted by ω , X-rays emerging from the top edge of the sample travel extra distance compared to the distance that X-rays from the bottom edge of the sample travel. This, then, leads to distortion of the scattered beam; namely, the scattered beam will appear on the CCD screen as a parallelogram as shown in Figure 3.8. Figure 3.9 shows the top- and sideview of the projection of the beam on the sample. From simple geometry, it can be shown that $a = Y_b / \tan \omega$, $b = aX/(2S)$, $c = aZ/(2S) + Y_B/2$, and $B = \tan^{-1}(Z/S)$. Since $H = 2c$ and $W = 2b$, H and W in

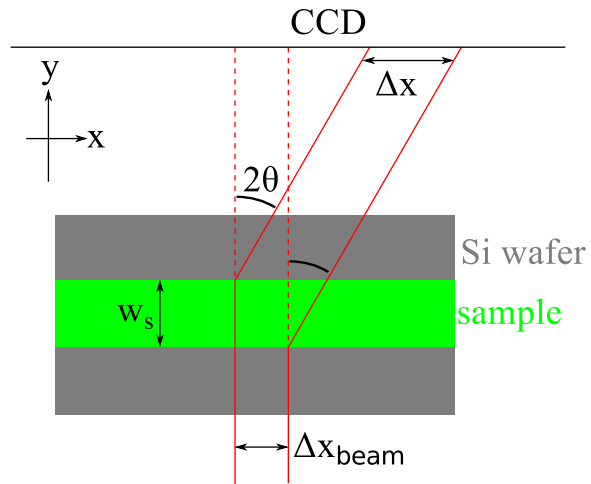


Figure 3.5: In-plane geometric broadening due to the sample width w_s and the beam width Δx_{beam} . A top view of the sample (green) on the Si wafer (gray) and the incoming and diffracted X-rays (bounded by red solid lines) are shown. The total in-plane scattering angle for a lipid chain-chain correlation is labeled as 2θ , and the geometric broadening as Δx .

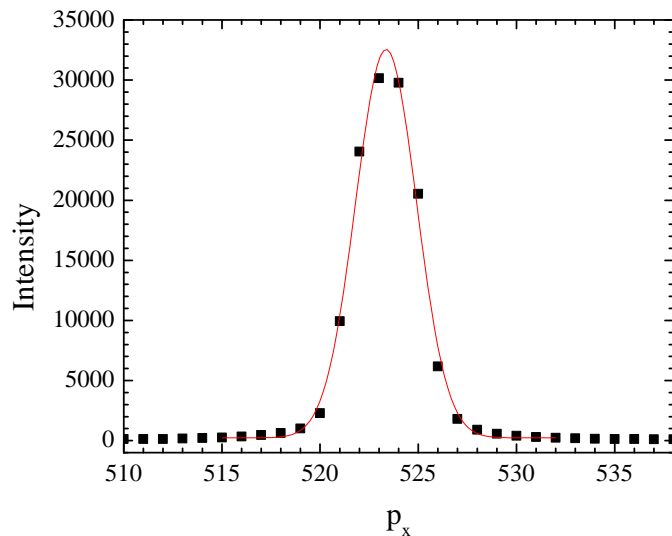


Figure 3.6: The horizontal profile of the beam used in the 2013 high resolution experiment. The CCD angular resolution $\Delta\theta = 0.0092^\circ$ corresponding to $\Delta q = 0.0017 \text{ \AA}^{-1}$, at the sample to detector distance of 220.6 mm. The beam FWHM = 3.7 pixels = 0.26 mm, giving $\Delta\theta = 0.034^\circ$ or $\Delta q = 0.0063 \text{ \AA}^{-1}$.

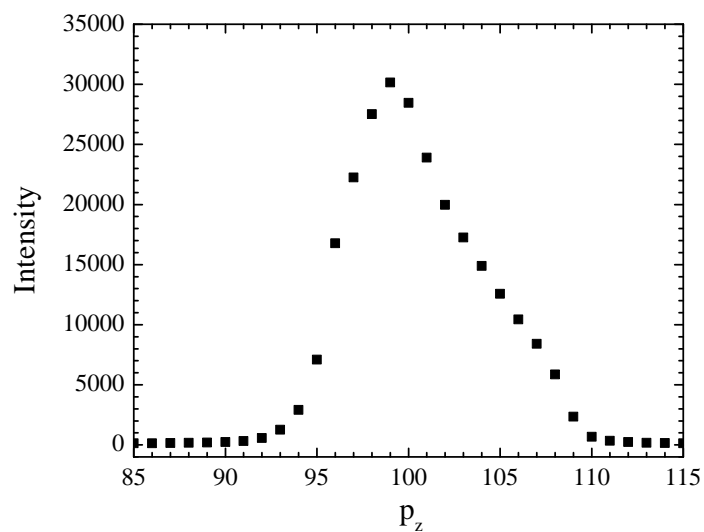


Figure 3.7: The vertical profile of the beam used in the 2013 high resolution experiment. The beam height = 9 pixels = 0.64 mm.

Figure 3.10 are given by

$$H = Y_b \left(1 + \frac{Z}{S \tan \omega} \right) \quad (3.1)$$

$$W = Y_b \frac{X}{S \tan \omega}. \quad (3.2)$$

The sample to detector distance S was 158.6 mm, giving an angular CCD resolution of $0.013^\circ/\text{pixel}$, or $0.0024 \text{ \AA}^{-1}/\text{pixel}$. The observed wide angle peak was at $(X, Z) = (44.0 \text{ mm}, 15.5 \text{ mm})$. The beam width and height were both $0.2 \text{ mm} = 2.8 \text{ pixels}$. With this setup, $W = 0.7 \text{ pixels}$ and $H = 3.1 \text{ pixels}$. Therefore, the distorted shape of the diffraction peak was negligible. Table 3.4 summarizes geometric broadening for our experiments.

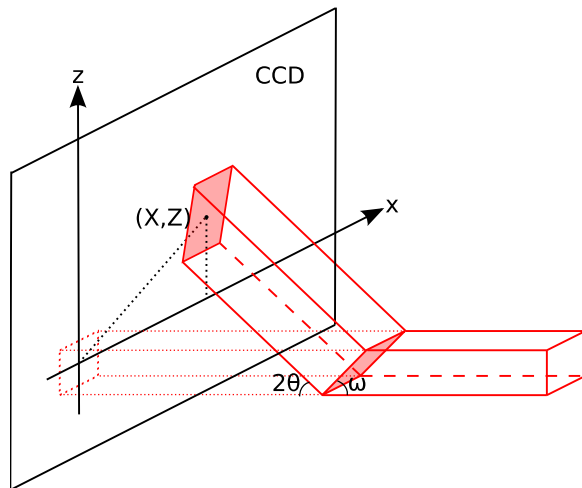


Figure 3.8: Geometric broadening in TWAXS. The cross section of the incoming X-ray with the sample and the CCD detector are both shaded in red. The sample is tilted by ω . The red dots show the transmitted beam. The incoming beam is rectangular but upon scattering appears as a parallelogram on the CCD.

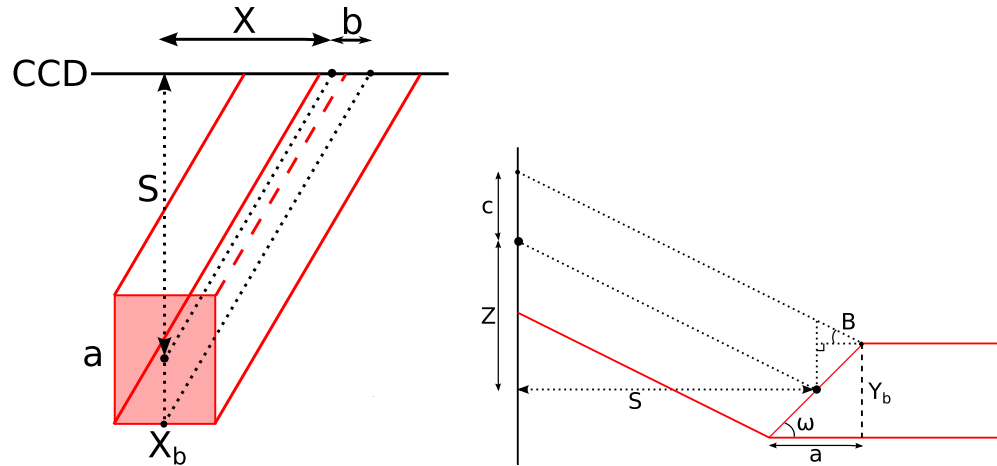


Figure 3.9: Top and side view of the beam on the sample in TWAXS. The cross section of the incoming X-ray with the sample is shaded in red. X_b and Y_b are the beam width and height, respectively. S is the sample to detector distance. (X, Z) is a position of the center of the scattered beam on the detector with respect to the center of the transmitted beam as shown in Figure 3.8.

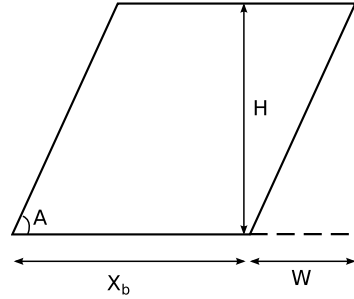


Figure 3.10: Projection of rectangular beam on the detector. Scattered beam appears as a parallelogram on the CCD.

type of experiment	horizontal (pixels)	horizontal (\AA^{-1})	vertical (pixels)	vertical (\AA^{-1})
LAXS	1.7	0.0019	$6.6q_z$	$0.0072q_z$
nGIWAXS	8	0.014		
TWAXS	2.8	0.0067	3.1	0.0074

Table 3.4: Geometric broadening

3.2.3 Low Angle X-ray Scattering Experiment

The X-ray beam for the low angle X-ray scattering (LAXS) experiment was set up by the station scientist, Dr. Arthur Woll. We chose the sample to detector distance to be 359.7 mm, measured by indexing silver behenate Bragg peaks. The D-spacing of silver behenate is known to be 58.367 Å.

Occasionally, sheets of molybdenum (Mo), each nominally 25 μm were used to attenuate the incoming beam. These sheets were installed by Dr. Arthur Woll in the upstream of the sample chamber. The attenuation length μ of 10.55 keV X-ray in Mo is 13.74 μm [103]. For a 25 μm thick Mo attenuator, the attenuation factor is calculated to be $[\exp(-25/13.74)]^{-1} = 6.2$. The exact attenuation factor was determined by comparing X-ray images collected with and without the attenuator, shown in Fig. 3.11. The attenuation factor of the nominally 25 μm thick Mo was found to be 6.9 for the wavelength used (1.175 Å), indicating an actual thickness of 27 μm .

Sheets of Mo were also used as a semi-transparent beam stop downstream of the sample, just outside the hydration chamber, to attenuate the beam and strong orders. 100 and 200 μm were used to attenuate strong orders and either 200 or 225 μm to attenuate the beam. To avoid saturation of CCD pixels by the very intense beam of 10^{11} photons/mm²/second, the beam stop was always set to attenuate the beam.

A few Bragg peaks in the low angle X-ray scattering of the ripple phase were very strong, leading to saturation of CCD pixels for data collection with a long exposure time. In order to probe a wide range of q -space, three images were taken: 1) a short, one second exposure with a nominally 25 micron molybdenum attenuator installed in the upstream of the sample to reduce the intensity of the incoming X-ray beam, 2) one second exposure without the beam attenuator, and 3) 60 second exposure with a beam stop blocking the very intense (1,0) and (2,0) peaks. See Fig. 3.12. Then, the integrated intensity of (1,0) peak was measured from the first image. This value was multiplied by 6.9 to account for the beam attenuation and by 60 to scale with the exposure time. The intensity of (2,0) and (2,-1) were measured from the second image, also multiplied by 60 to account for the shorter exposure time. The intensities of the rest of the observed peaks were measured from the third image.

The integrated intensity of each peak was obtained using the Nagle lab tview software developed by Dr. Yufeng Liu [50] by putting a box around a peak and summing up the intensity in those pixels that fall inside the box. The background

scattering was estimated by measuring the intensity in pixels near the peak but not containing any peak tail. The choice of box size was made according to the width of each peak. Because of mosaic spread in the sample, the peaks were wider for higher orders. Consequently, the box was made wider for higher orders. The box size was chosen so that approximately 80% of the peak intensity was counted toward the integrated intensity.

3.2.4 Near Grazing Incidence Wide Angle X-ray Scattering Experiment

The high resolution wide angle X-ray scattering (WAXS) experiment was also carried out at the G1 station. The instrument was set up by the G1 station scientist, Arthur Woll, and the assistant scientist, Dr. Robin Baur. Wide angle X-ray scattering was collected at an incident angle of 0.2° . The total external reflection from an air-lipid interface occurs approximately at 0.1° and 0.17° for air-silicon interface, so 0.2° is not quite grazing incidence. Grazing incidence usually implies that the incident angle is less than the critical angle for a total external reflection. Therefore, 0.2° is called near grazing incidence (NGI) in this thesis. The background scattering was collected at -0.2° . Subtraction of the negative angle data from the positive angle data resulted in a clean sample scattering image.

3.2.5 Transmission Wide Angle X-ray Scattering Experiment

The transmission wide angle X-ray scattering (TWAXS) experiment was also carried out at the G1 station. The incident angle ω was set to -45° for transmission data collection (see Fig. 3.13). A $35\ \mu\text{m}$ thick silicon substrate absorbs 10.5 keV X-ray by only 20% [103], so most of the incoming X-rays penetrated the thin substrate.

Unfortunately, the axis of the rotation motor did not coincide with the sample axis, so the sample to detector distance varied as ω was varied. To accurately measure the sample to detector distance, low angle scattering from a silver behenate (AgBe) sample was collected at a fixed ω . Due to large mosaic spread of the AgBe sample, many orders were visible. While the relative intensity of each order was inaccurate, the positions of peaks were the same as those observed with a rotating sample. To measure the D-spacing of the sample, ω was set to 1° . The sample to detector distance was measured to be 174.7 mm at $\omega = 0^\circ$. From the sample holder geometry shown in

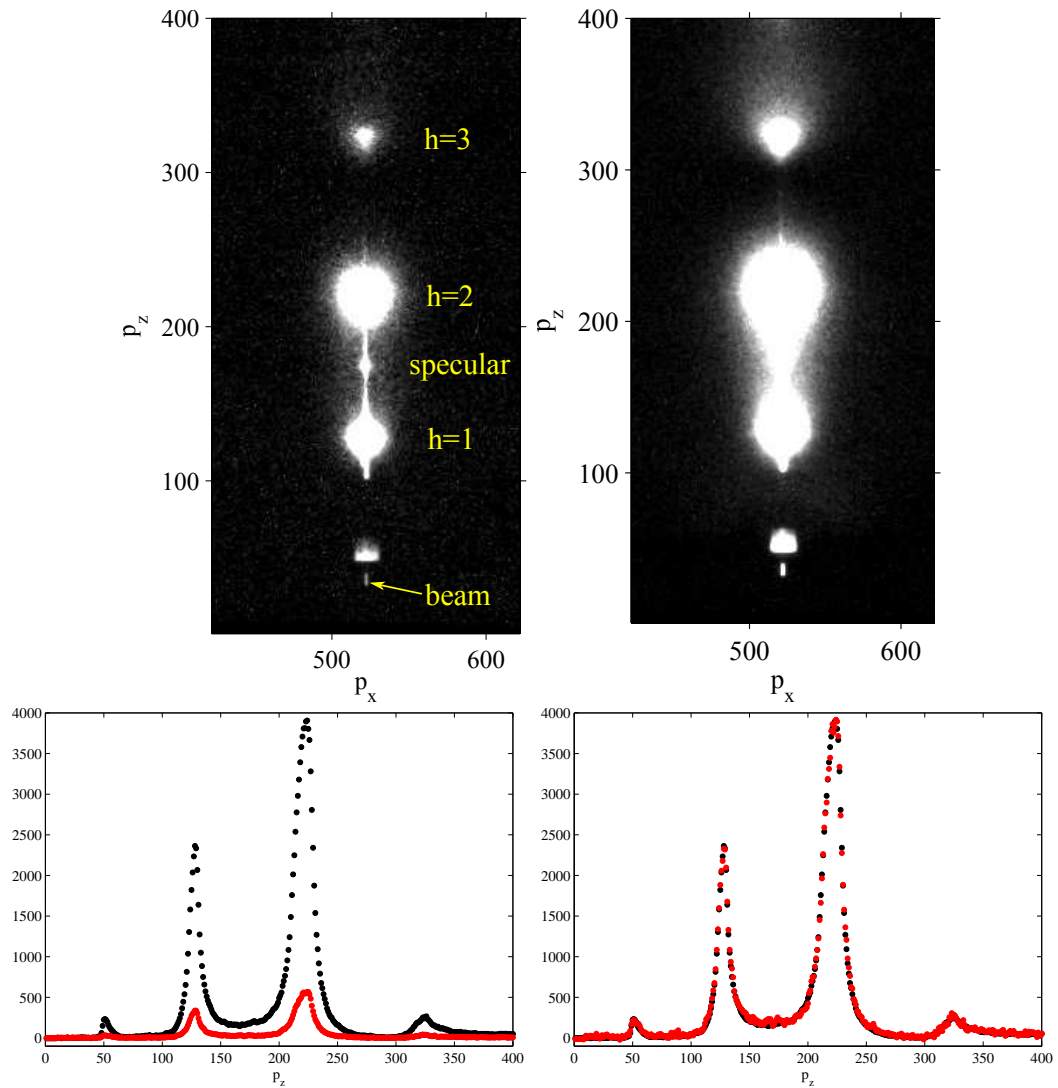


Figure 3.11: (top panels) CCD images of X-ray scattering taken with (left) and without (right) a nominally $25 \mu\text{m}$ thick Mo attenuator. These data were taken at a fixed angle of incidence $\omega = 0.8^\circ$. The sample was an oriented film of DOPC:DOPE (3:1) in the fluid phase at 37°C . The wavelength was 1.175 \AA , the same as the one used for the ripple phase experiment. The same gray scale is used in both images. $100 \text{ pixel} = 0.11 \text{ \AA}^{-1}$ in q . A small dot located about $(p_x, p_z) = (520, 170)$ between the first and second orders is a specular reflection from the substrate. The exposure times were 1 second. (bottom panels) Vertical p_z slices of the X-ray images shown in the top panels (left). The scattering intensity measured with the attenuator (red solid circles) was multiplied by a factor of 6.9 and compared to the intensity measured without the attenuator (black solid circles, right).

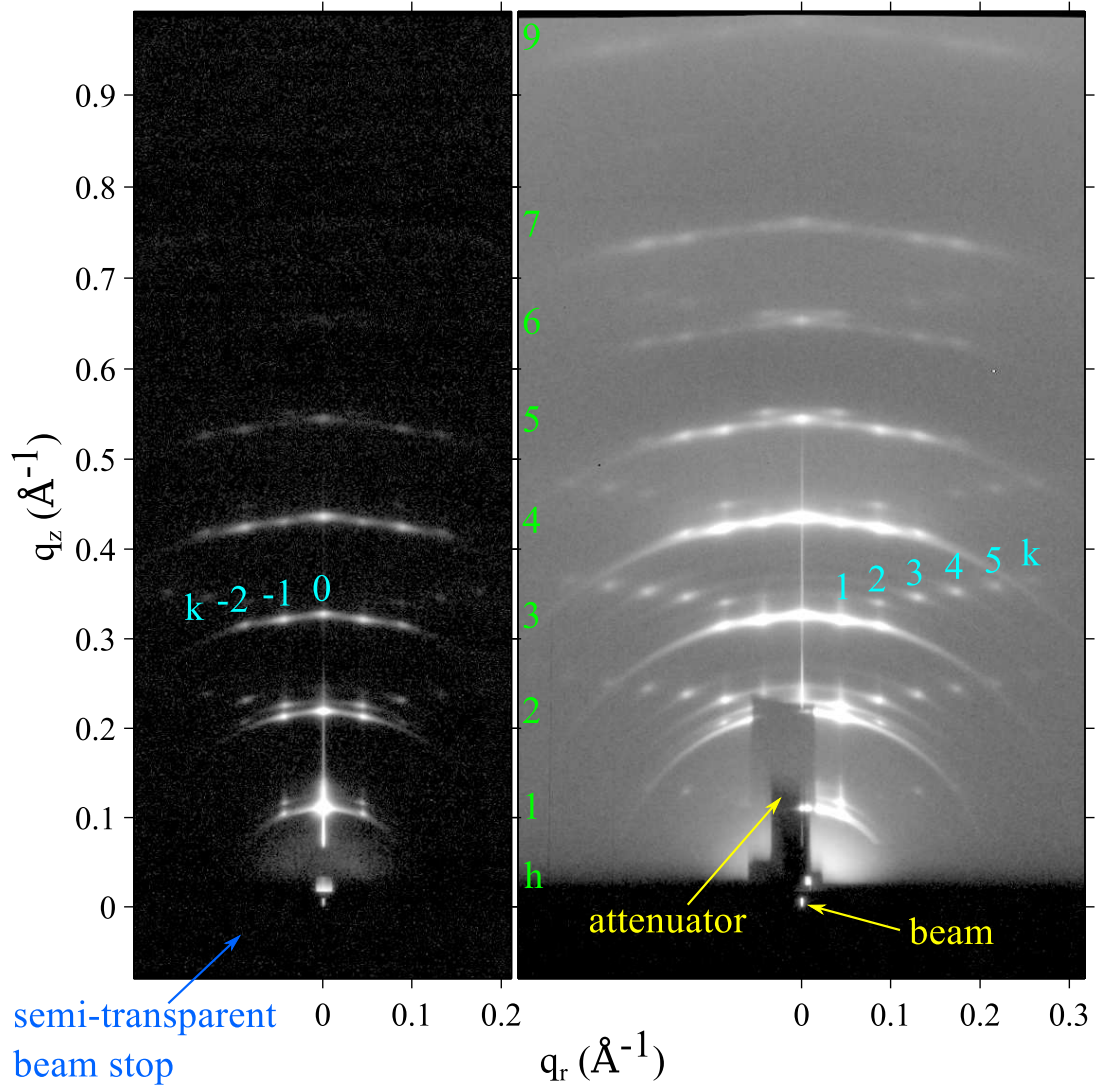


Figure 3.12: 1 second exposure (left) and 60 second exposure (right) of the low angle X-ray scattering from the DMPC ripple phase in gray log scales. The index h is labeled in green. $(3, k)$ reflections are identified in cyan. The shadow cast by 100 μm thick molybdenum attenuator blocking strong $(1, 0)$ and $(2, 0)$ orders in the right image is labeled as attenuator and extends from $q_z = 0 \text{ \AA}^{-1}$ to 0.2 \AA^{-1} . $D = 57.8 \text{ \AA}$, $\lambda_r = 145.0 \text{ \AA}$, and $\gamma = 98.2^\circ$.

Fig. 3.14, the sample to detector distance was estimated to be 158.6 mm at $\omega = 45^\circ$. A picture of the sample holder is shown in Fig. 3.15.

To level the sample, the sample was first leveled coarsely by watching the sample scattering. When ω was negative, much of the incoming beam was absorbed by the flat substrate, yielding weak sample scattering. When ω became positive, sample scattering was strong. With this procedure, we leveled the sample with an uncertainty of $\pm 0.2^\circ$. We then measured the beam intensity at various sample heights as a function of ω . The sample was level when the beam intensity had the narrowest dip as the sample was moved vertically through the beam.

Background scattering was collected by replacing the sample with a bare wafer. The bare wafer was not placed exactly at the same location as the sample, which gave slightly different background scattering. This only affected the background subtraction near the beam. The wide angle scattering was not affected by this inexact placement of the bare wafer.

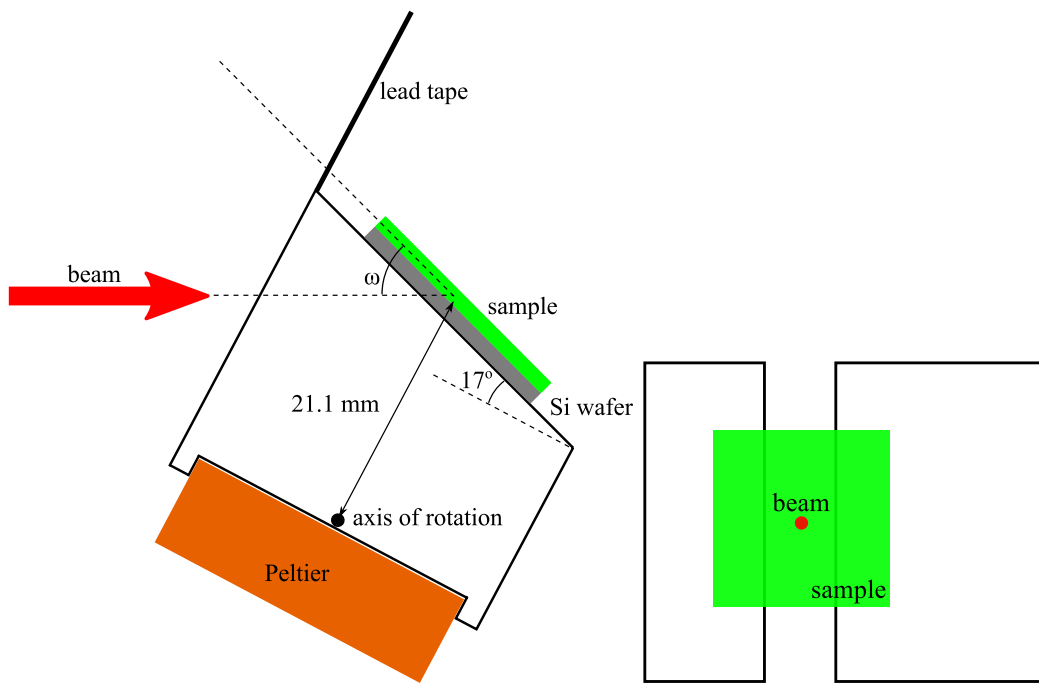


Figure 3.13: Schematics of the sample holder in the transmission mode. Side (left) and top (right) views are shown. The thickness of the Si wafer = $35 \mu\text{m}$. The thickness of the sample $\approx 10 \mu\text{m}$. The distance between the axis of rotation and sample = 21.1 mm.

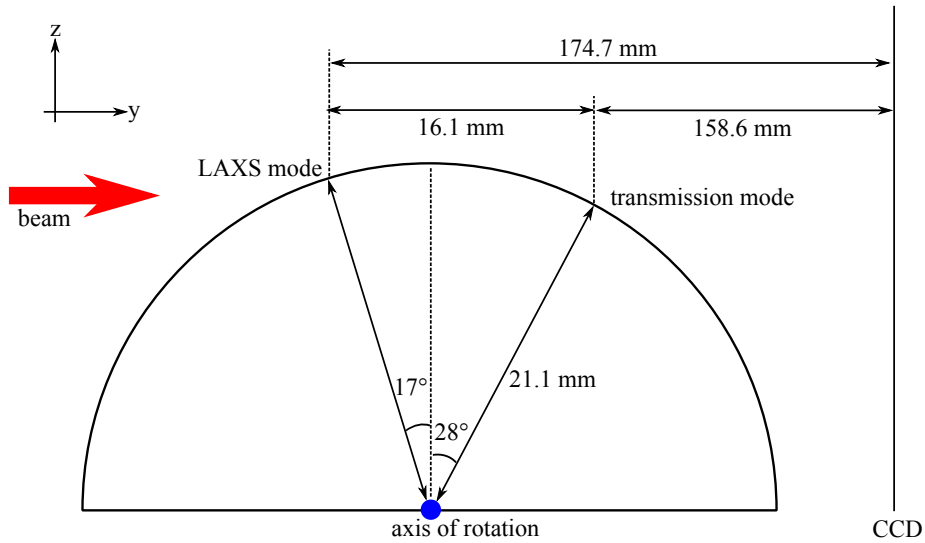


Figure 3.14: Circular path followed by the sample as the angle of incidence ω was changed. The sample to detector distance and D -spacing of the sample were measured in the LAXS mode, where $\omega = 1^\circ$. WAXS images were collected at the transmission mode, where $\omega = -45^\circ$. The z position of the sample was slightly higher at the LAXS mode than at the transmission mode, so the sample holder was vertically shifted for different modes.

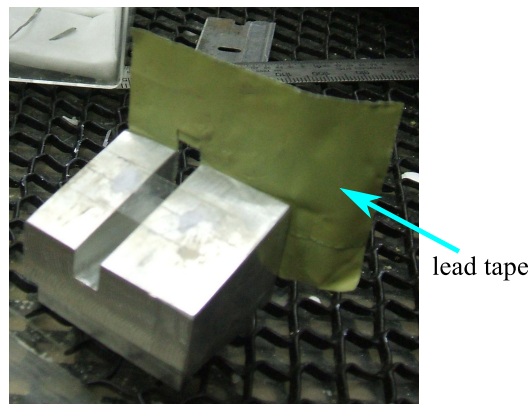


Figure 3.15: Picture of the sample holder looking from above. A lead tape was attached to the back of the sample holder to help reduce the background scattering, typically coming from the air gap between the flightpath snout and the mylar window of the chamber.

3.3 LAXS: analysis

3.3.1 Lattice Structure

The unit cell vectors for the two-dimensional oblique lattice shown in Fig. 3.1 can be expressed as

$$\mathbf{a} = \frac{D}{\tan \gamma} \hat{\mathbf{x}} + D \hat{\mathbf{z}} \quad (3.3)$$

and

$$\mathbf{b} = \lambda_r \hat{\mathbf{x}}. \quad (3.4)$$

The corresponding reciprocal lattice unit cell vectors are

$$\mathbf{A} = \frac{2\pi}{D} \hat{\mathbf{z}} \quad (3.5)$$

and

$$\mathbf{B} = \frac{2\pi}{\lambda_r} \hat{\mathbf{x}} - \frac{2\pi}{\lambda_r \tan \gamma} \hat{\mathbf{z}}. \quad (3.6)$$

The reciprocal lattice vector, \mathbf{q}_{hk} for the Bragg peak with Miller indices (h, k) is

$$\mathbf{q}_{hk} = h\mathbf{A} + k\mathbf{B}, \quad (3.7)$$

so its Cartesian components are

$$\mathbf{q}_{hk} \cdot \hat{\mathbf{x}} = q_{hk}^x = \frac{2\pi k}{\lambda_r} \equiv q_k^x \quad (3.8)$$

$$\mathbf{q}_{hk} \cdot \hat{\mathbf{y}} = q_{hk}^y = 0 \quad (3.9)$$

$$\mathbf{q}_{hk} \cdot \hat{\mathbf{z}} = q_{hk}^z = \frac{2\pi h}{D} - \frac{2\pi k}{\lambda_r \tan \gamma}. \quad (3.10)$$

Our sample consists of many ripple domains with a uniform distribution of in-plane directions of the ripple wave vector, \mathbf{b} in Fig. 3.1. In this case, q_{hk}^x and q_{hk}^y are combined to give $q_{hk}^r = 2\pi k / \lambda_r$.

3.3.2 Sample q-space

The incoming and outgoing wavevectors of the x-ray beam in Fig. 3.16 are given by

$$\mathbf{k}_{\text{in}} = \frac{2\pi}{\lambda} \hat{\mathbf{y}}, \quad \mathbf{k}_{\text{out}} = \frac{2\pi}{\lambda} (\sin 2\theta \cos \phi \hat{\mathbf{x}} + \cos 2\theta \hat{\mathbf{y}} + \sin 2\theta \sin \phi \hat{\mathbf{z}}), \quad (3.11)$$

where λ is the wavelength of x-ray, 2θ is the total scattering angle, and ϕ is the angle measured from the equator on the detector. The scattering vector (also called momentum transfer vector) is the difference between \mathbf{k}_{in} and \mathbf{k}_{out} ,

$$\begin{aligned} \mathbf{q} &= \mathbf{k}_{\text{out}} - \mathbf{k}_{\text{in}} \\ &= q (\cos \theta \cos \phi \hat{\mathbf{x}} - \sin \theta \hat{\mathbf{y}} + \cos \theta \sin \phi \hat{\mathbf{z}}), \end{aligned} \quad (3.12)$$

where $q = 4\pi \sin \theta / \lambda$ is the magnitude of the scattering vector. When the sample is rotated by ω about the lab x-axis in the clockwise direction as shown in Fig. 3.16, the sample q -space also rotates and are given by

$$\hat{\mathbf{e}}_x = \hat{\mathbf{x}}, \quad \hat{\mathbf{e}}_y = \cos \omega \hat{\mathbf{y}} + \sin \omega \hat{\mathbf{z}}, \quad \hat{\mathbf{e}}_z = -\sin \omega \hat{\mathbf{y}} + \cos \omega \hat{\mathbf{z}}. \quad (3.13)$$

From Eq. (3.12) and (3.13), we find Cartesian components of the sample q -space to be

$$\begin{aligned} q_x &= \mathbf{q} \cdot \hat{\mathbf{e}}_x = q \cos \theta \cos \phi, \\ q_y &= \mathbf{q} \cdot \hat{\mathbf{e}}_y = q (-\sin \theta \cos \omega + \cos \theta \sin \phi \sin \omega), \\ q_z &= \mathbf{q} \cdot \hat{\mathbf{e}}_z = q (\sin \theta \sin \omega + \cos \theta \sin \phi \cos \omega). \end{aligned} \quad (3.14)$$

The position, (X, Z) , of a CCD pixel is measured with respect to the beam and given by

$$X = S \tan 2\theta \cos \phi, \quad Z = S \tan 2\theta \sin \phi, \quad (3.15)$$

where S is the distance between the sample and detector.

From a model for the electron density of a lipid bilayer, one calculates the X-ray scattering intensity pattern, $I(\mathbf{q})$. Then, Eq. (3.14) and (3.15) relate $I(\mathbf{q})$ to the experimentally measured intensity pattern, $I(X, Z)$. It is important to remember that a given pixel position, (X, Z) , corresponds to a triplet (q_x, q_y, q_z) . Fully exploring the sample q -space requires changing ω for a fixed wavelength, which was achieved

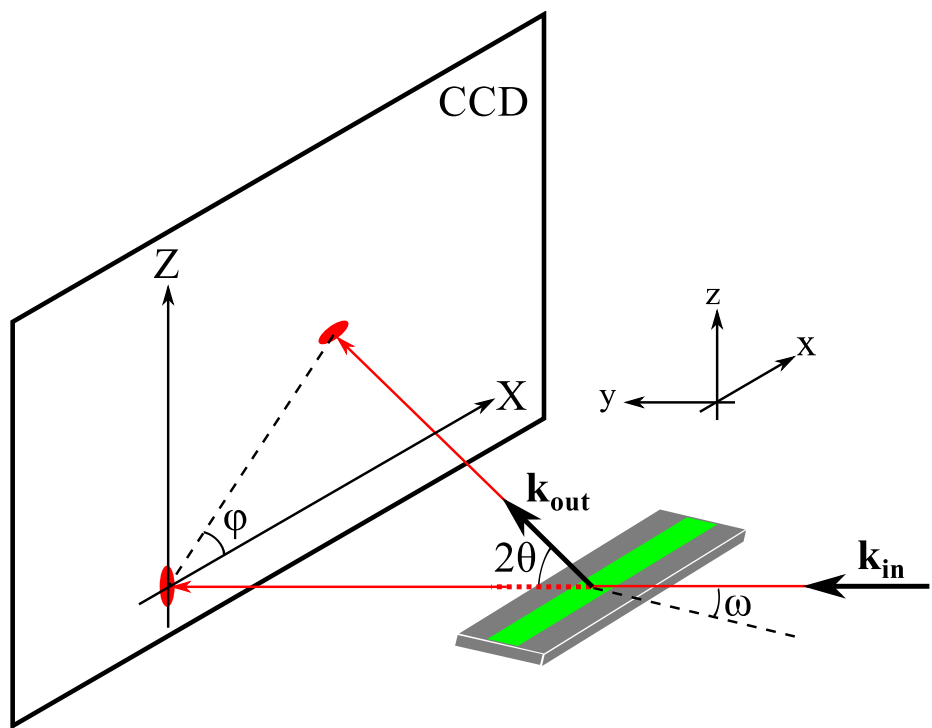


Figure 3.16: Experimental reflectivity geometry.

by continuously rotating the sample with a motor. In the ripple phase, because our sample has in-plane rotational symmetry, the ripple side peaks ($h, k \neq 0$) make up Bragg rings while the main peaks ($h, k = 0$) are still delta function like (see Fig. 3.17) in q -space. In order for the main peak to be observed, ω must be equal to θ_B , but the side peaks are observed at any ω . Those side peaks get slightly smeared due to integration over q_y .

For low angle x-ray scattering (LAXS), it is convenient to linearize the above equations in terms of θ and ω . In the small angle approximation, $\sin \phi \approx Z/(2S\theta)$ and $\cos \phi \approx X/(2S\theta)$, and

$$\begin{aligned} q_x &\approx \frac{4\pi\theta \cos \phi}{\lambda} \approx kX/S \\ q_y &\approx q_z \omega - \frac{4\pi\theta^2}{\lambda} \approx q_z \omega - \frac{\lambda q_z^2}{4\pi} \\ q_z &\approx \frac{4\pi\theta \sin \phi}{\lambda} \approx kZ/S, \end{aligned} \quad (3.16)$$

with $k = 2\pi/\lambda$. For wide angle X-ray scattering, the exact relations given by Eq. (3.14) are necessary. Especially in the transmission experiment, where ω is large, an observed X-ray pattern appears nontrivial and becomes almost impossible to analyze without the use of Eq. (3.14). The transmission experiment is discussed in Sec.3.7.

3.3.3 Lorentz Correction

Our sample has in-plane rotational symmetry about the z -axis. Ignoring mosaic spread to which we will come back later, this means that the sample consists of many domains with differing ripple directions, all domains being parallel to the substrate. In sample q -space, ripple ($h, k \neq 0$) side peaks are represented as rings centered at the meridian, or q_z -axis, while ($h, k = 0$) main peaks are still points on the meridian (see Fig. 3.17). Then, for an arbitrary incident angle ω , ($h, 0$) peaks are not observed while side peaks are observed for a range of ω as will now be explained.

In order to capture all (h, k) peaks in one X-ray exposure, the sample was continuously rotated over a range of $\omega, \Delta\omega$, about the x -axis. As a result of this rotation, the ($h, 0$) main peaks become arcs that subtend an angle $\Delta\omega$, as shown in Fig. 3.18, with its length equal to $\Delta\omega q_{h0}$. The detector records the intersections of these arcs

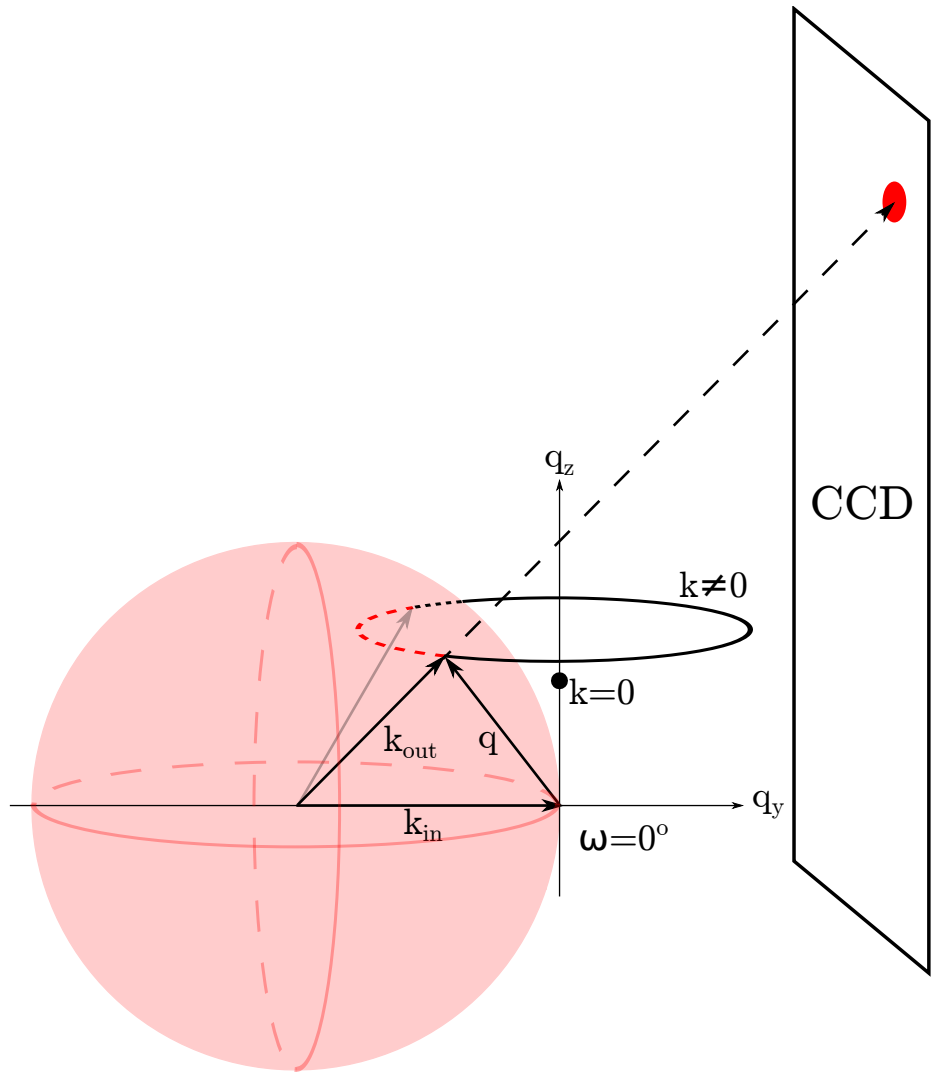


Figure 3.17: Ewald sphere construction for the ripple phase diffraction in the low angle regime. A ripple $k = 0$ peak is the solid, black circle on the q_z -axis. A ripple $k \neq 0$ ring is the black ring centered about the q_z -axis. The portion of the ring that is inside the Ewald sphere is shown as a red dashed line and the portion of the ring that is outside but behind the Ewald sphere is shown as a black dotted line. The magnitude of the total scattering angle is exaggerated. With a wavelength of 1.175 \AA , the magnitude $|k_{in}| = 5.35 \text{ \AA}^{-1}$. For a $h = 5$ peak, $q_{50}^z = 0.54 \text{ \AA}^{-1}$, one tenth of k_{in} .

with the Ewald sphere, so the intrinsic scattering intensity of the $(h, k = 0)$ reflections is the product of the observed intensity, I_{hk}^{obs} with the arc length, that is,

$$I_{h0} = \Delta\omega q_{h0}^z I_{h0}^{\text{obs}}. \quad (3.17)$$

This is the usual Lorentz correction for lamellar orders.

Now, we consider relative intensity of side peaks for a given order h . As described earlier, $(h, k \neq 0)$ side peaks are represented as rings whose radius is q_{hk}^r in the sample q -space. Because only the domains with the right ripple direction can satisfy the Bragg's condition at a given fixed angle ω , the intrinsic scattering intensity in this ring is reduced by a factor of $2\pi q_k^r$ compared to the $(h, 0)$ reflections. This reduction of intensity can be nicely visualized by the Ewald sphere construction shown in Fig. 3.17, which shows that the entire rings are not intersected by the Ewald sphere at a fixed angle. Then, the intrinsic scattering intensity in a ring is

$$I_{hk \neq 0} \propto 2\pi q_{hk}^r I_{hk}^{\text{obs}}. \quad (3.18)$$

During an X-ray exposure, the sample q -space rotates and the rings are intersected by the Ewald sphere at all our experimental incident angles ω . However, as Fig. 3.19 shows, only small parts of the rings are actually intersected with the Ewald sphere. To obtain the full expression for $(h, k \neq 0)$ reflections, we now turn to a more rigorous calculation.

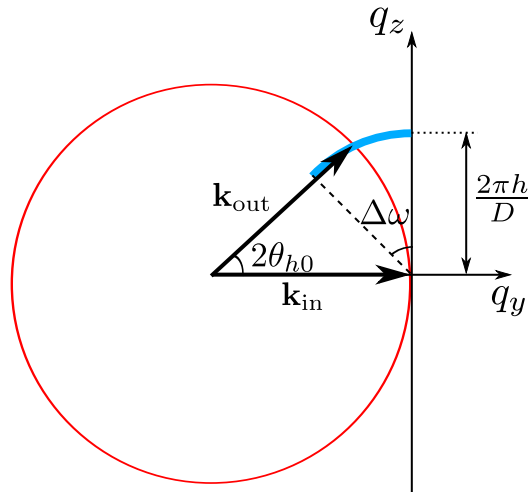


Figure 3.18: Side view of an arc of $k = 0$ peak shown as a thick blue line.

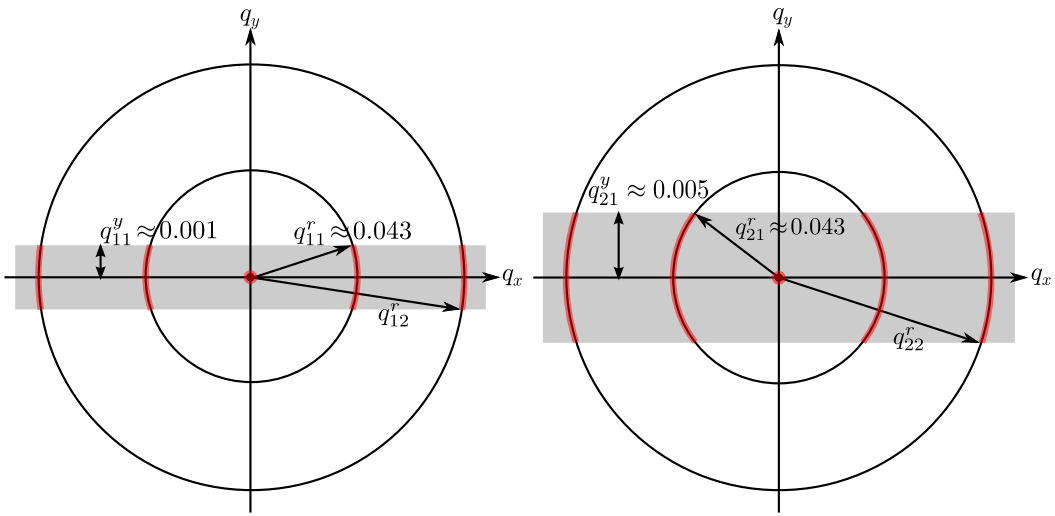


Figure 3.19: q -space representations of Bragg peaks and Bragg rings for $h = 1$ and 2 and $k = 0, 1$, and 2 in q_{hk}^z planes. The intersection between the Ewald sphere and a Bragg peak/ring is indicated in red. The observed intensity for the $k \neq 0$ orders is proportional to the fraction of the length of red arcs in the circumference. This fraction is equal to one for $k = 0$ reflections. Because the reflections are not in the same q_z plane, the range of q_y integration indicated by the height of the gray rectangle is different for different h orders. For $\gamma \neq 90^\circ$, the range of q_y integration is slightly different for different k reflections with the same h . The values shown are for $D = 58$ Å, $\lambda_r = 145$ Å, $\gamma = 90^\circ$, and $\lambda = 1.175$ Å. The magnitude of curvature of arcs is exaggerated.

Mathematically, the rotation is equivalent to an integration over ω . In low angle X-ray scattering, q_z is nearly constant at a given pixel as ω is changed, which can be seen from Eq. (3.16). As Eq. (3.16) shows, ω dependence appears only through q_y , so rotating the sample is realized by integrating over q_y ; formally, we write $d\omega = dq_y/q_z$. To derive the integration limits on q_y , let us consider two cases: (1) When $\omega \leq 0$, the incoming X-ray beam is blocked by the back of the substrate. This sets the lower limit of ω to 0. Plugging $\omega = 0$ in Eq. 3.16), we find the lower limit of the q_y integration to be $-\lambda q_z^2/(4\pi)$. (2) When $\omega \geq 2\theta$, the substrate blocks the outgoing X-ray, so the maximum $\omega = 2\theta$. Within the small angle approximation, $q_z \approx 4\pi\theta/\lambda$. Then, the maximum ω can be expressed as $\lambda q_z/(2\pi)$. Plugging this expression for ω in Eq. (3.16), we find the upper limit of the q_y integration to be $\lambda q_z^2/(4\pi)$. Also integrating over the detector pixels X and Z to obtain integrated intensity, we write the observed intensity as

$$\begin{aligned} I_{hk}^{\text{obs}} &\propto \int dX \int dZ \int d\omega I_{hk} \\ &\propto \int dq_x \int dq_z \int_{-\frac{\lambda q_z^2}{4\pi}}^{\frac{\lambda q_z^2}{4\pi}} \frac{dq_y}{q_z} I_{hk}(\mathbf{q}), \end{aligned} \quad (3.19)$$

where $1/q_z$ factor in q_y integration is the usual Lorentz polarization factor in the small angle approximation.

For a crystalline sample with in-plane rotational symmetry, the structure factor of a ripple Bragg peak is

$$S_{hk}(\mathbf{q}) = S_{hk}(q_r, q_z) = \frac{1}{2\pi q_r} \delta(q_r - q_{hk}^r) \delta(q_z - q_{hk}^z), \quad (3.20)$$

where $q_{hk}^r = 2\pi|k|/\lambda_r$. Thus, the scattering pattern in the ripple phase is a collection of Bragg rings for $k \neq 0$ centered at the meridian and the Bragg peaks for $k = 0$ located along the meridian. The scattering intensity is $I(\mathbf{q}) = |F(\mathbf{q})|^2 S(\mathbf{q})$, where $F(\mathbf{q})$ is the form factor. After the q_z integration, the observed, integrated intensity of (h, k) peak is proportional to

$$I_{hk}^{\text{obs}} \propto \frac{|F_{hk}|^2}{q_{hk}^z} \int dq_x \int_{-q_{hk}^{y0}}^{q_{hk}^{y0}} dq_y \frac{\delta(q_r - q_{hk}^r)}{2\pi q_r}, \quad (3.21)$$

where $q_{hk}^{y0} = \lambda(q_{hk}^z)^2/(4\pi)$. For side peaks ($k \neq 0$), we have

$$\begin{aligned} \int dq_x \int_{-q_{hk}^{y0}}^{q_{hk}^{y0}} dq_y \frac{\delta(q_r - q_{hk}^r)}{2\pi q_r} &\approx \int_{-q_{hk}^{y0}/q_{hk}^r}^{q_{hk}^{y0}/q_{hk}^r} d\phi \int dq_r q_r \frac{\delta(q_r - q_{hk}^r)}{2\pi q_r} \\ &= \frac{q_{hk}^{y0}}{\pi q_{hk}^r}. \end{aligned} \quad (3.22)$$

For main peaks ($k = 0$), we have

$$\begin{aligned} \int dq_x \int_{-q_{hk}^{y0}}^{q_{hk}^{y0}} dq_y \frac{\delta(q_r - q_{hk}^r)}{2\pi q_r} &= \int_0^{2\pi} d\phi \int dq_r q_r \frac{\delta(q_r - q_{hk}^r)}{2\pi q_r} \\ &= 1 \end{aligned} \quad (3.23)$$

Using Eq. (3.21 – 3.23), we write the observed integrated intensity as

$$I_{h0}^{\text{obs}} \propto \frac{|F_{h0}|^2}{q_{h0}^z} \quad (3.24)$$

$$I_{hk}^{\text{obs}} \propto \frac{|F_{hk}|^2}{q_{hk}^z} \frac{q_{hk}^{y0}}{\pi q_{hk}^r} = |F_{hk}|^2 \frac{\lambda q_{hk}^z}{2\pi} \frac{1}{2\pi q_{hk}^r} = |F_{hk}|^2 \frac{2\theta_{hk}}{2\pi q_{hk}^r}, \quad (3.25)$$

where $2\theta_{hk} = \lambda q_{hk}^z/(2\pi)$ is the incident angle at which the outgoing X-ray for the peak (h, k) is blocked by the substrate. Eq. (3.24) and (3.25) relate the form factor calculated from a model to the experimentally observed intensity, and are partially equivalent to Eq. (3.17) and (3.18).

In non-linear least squares fitting procedure, we fitted the observed integrated intensity to the calculated intensity from a bilayer model using these Lorentz corrections. This is because we can determine experimental uncertainties on observed intensity rather than the Lorentz-corrected form factors. We avoid propagating the uncertainties by fitting a model to observed intensity.

3.3.4 Absorption Correction for LAXS

In this section, we derive the absorption correction for an oriented sample. The calculation involves an explicit integration over the incident angle, ω , which is necessitated by the sample rotation during an X-ray exposure. The procedure is to write down an absorption factor, $A(\omega, \theta)$, for a given scattering angle at a given incident angle,

and then integrate over ω . We ignore q_x dependence because the X-ray path inside the sample is nearly within the y - z plane for low angle scattering. The correction for wide angle scattering is described in a later section.

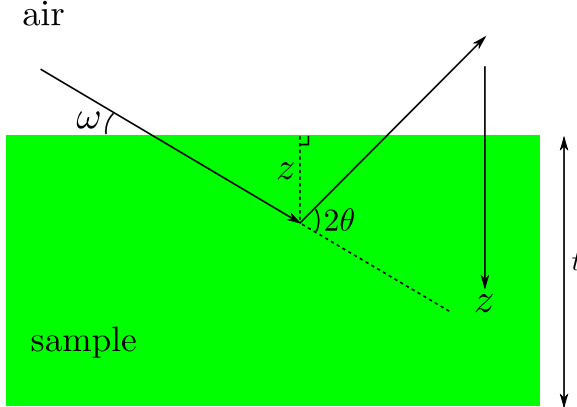


Figure 3.20: The path of X-rays within the sample. The incident angle is ω and the total scattering angle is 2θ . An X-ray with a penetration depth of z is shown. The total thickness of the sample is t . Refraction correction is smaller than what? for $\theta > 0.5^\circ$ ($h = 1$).

Assume that all the X-rays enter the sample from the top surface. The total scattering angle is given by 2θ (see Fig. 3.20). Let the z -axis point downward. At the top surface (air-sample interface), $z = 0$. For X-rays that travel to z and then scatter, the total path length within the sample is

$$L(z, \omega, \theta) = \frac{z}{\sin \omega} + \frac{z}{\sin(2\theta - \omega)} = z g(\omega, \theta), \quad (3.26)$$

where $g(\omega, \theta) = (\sin \omega)^{-1} + (\sin(2\theta - \omega))^{-1}$. For each ray, the intensity is attenuated by the sample absorption. If non-attenuated intensity is equal to I_0 , then the attenuated intensity is

$$I(z, \omega, \theta) = I_0 \exp\left(-\frac{L}{\mu}\right), \quad (3.27)$$

where μ is the absorption length of an X-ray. μ is about 2.6 mm for 10.5 keV for both water and lipids in all phases [103]. The observed intensity of scattering from a sample fixed at an angle ω is equal to the integration of Eq. (3.27) over the total

thickness of the sample and given by

$$\begin{aligned} I(\omega, \theta) &= \int_0^t dz I(z, \omega, \theta) = I_0 \int_0^t dz \exp\left(-\frac{g(\omega, \theta)}{\mu} z\right) \\ &= I_0 \mu \frac{1 - \exp\left(-\frac{t}{\mu} g(\omega, \theta)\right)}{g(\omega, \theta)}. \end{aligned} \quad (3.28)$$

Defining the absorption factor at a fixed angle to be $A(\omega, \theta)$, the observed intensity can also be written as

$$I(\omega, \theta) = A(\omega, \theta) t I_0, \quad (3.29)$$

where $t I_0$ is the intensity we would observe for non-absorbed X-rays. Equating Eq. (3.28) and (3.29), we get

$$A(\omega, \theta) = \frac{\mu}{t} \frac{1 - \exp\left(-\frac{t}{\mu} g(\omega, \theta)\right)}{g(\omega, \theta)}. \quad (3.30)$$

If μ is taken to infinity (no absorption), $A(\omega, \theta)$ goes to 1 as expected. The absorption factor A_{h0} for the $k = 0$ peaks is given by $A(\omega = \theta = \theta_B)$, plotted in Fig. 3.21. As shown, this factor is about 20 % for $h = 1$ peak relative to $h = 4$, so it is not negligible.

For $k \neq 0$ side peaks, an integration over the incident angle ω is necessary because these peaks are observable at all our experimental incident angles as described in section 3.3.3. The observed intensity for side peaks from a rotating sample is simply

$$I_{\text{obs}}(\theta) = \int_0^{2\theta} d\omega I(\omega, \theta). \quad (3.31)$$

The upper integration limit is equal to 2θ because the substrate completely blocks the scattered X-rays above this angle as discussed in section 3.3.3. Eq. (3.30), which is essentially the integrand in Eq. (3.31), is plotted in Fig. 3.22. It is maximum when $\omega = \theta$, meaning that the path length is shortest at the Bragg condition. The non-attenuated observed intensity is equal to $2\theta t I_0$. We, then, define the absorption factor $A(\theta)$ to be the ratio of the total observed intensity to the total non-attenuated intensity,

$$A(\theta) \equiv \frac{I_{\text{obs}}(\theta)}{2\theta t I_0}. \quad (3.32)$$

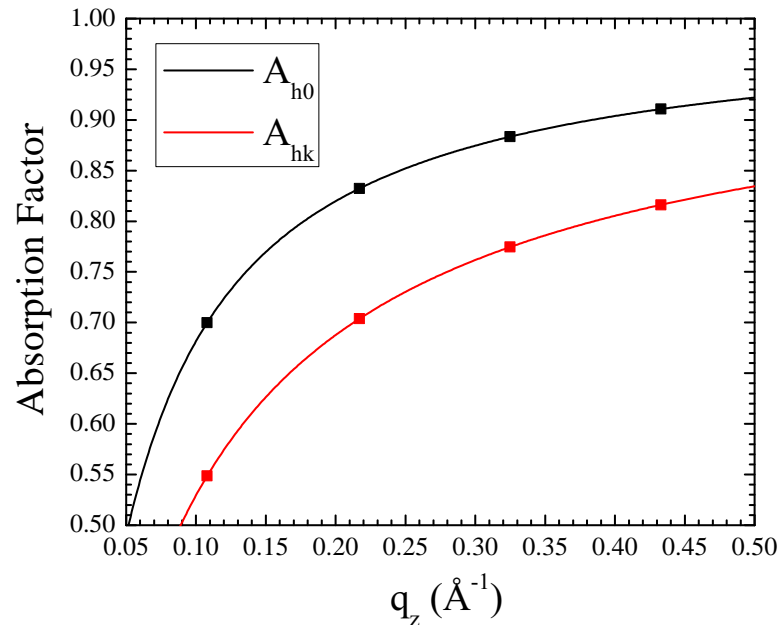


Figure 3.21: Absorption factors as a function of $q_z \approx 4\pi\theta/\lambda$. Values at $q_z = 2\pi h/D$ corresponding to $D = 57.8 \text{ \AA}$ are shown as squares. $\mu = 2600 \mu\text{m}$, $t = 10 \mu\text{m}$, and $\lambda = 1.175 \text{ \AA}$.

Using Eq. (3.30) and (3.31) in (3.32), we arrive at the final absorption factor

$$A(\theta) = \frac{1}{2\theta} \int_0^{2\theta} d\omega A(\omega, \theta) = \frac{\mu}{2\theta t} \int_0^{2\theta} d\omega \frac{1 - \exp\left(-\frac{t}{\mu}g(\omega, \theta)\right)}{g(\omega, \theta)}. \quad (3.33)$$

$A_{hk} = A(\theta)$ is plotted in Fig. 3.21. The absorption correction $A_c(\theta)$ is the inverse of Eq. (3.33).

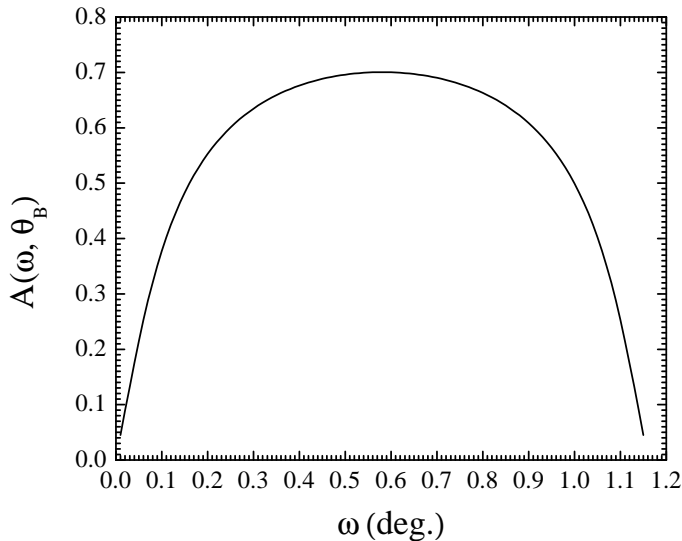


Figure 3.22: Eq. (3.30) plotted as a function of ω for $\theta = \theta_B = 0.58^\circ$, corresponding to a Bragg angle for $D = 57.8 \text{ \AA}$.

3.3.5 Correction due to mosaic spread

Integrated intensity needs to be corrected for mosaic spread. During an X-ray exposure, the sample was continuously rotated. Due to this rotation, each pixel integrates intensity over a range of incident angles ω . As described in appendix A.1.2, a mosaic spread distribution can be probed by changing ω , so rotating the sample is essentially equivalent to integrating a mosaic spread distribution. Because the range of the distribution probed is approximately given by $\omega = [0, 2\theta_{hk}]$ where θ_{hk} is the Bragg angle for a (h, k) reflection, this range is larger for higher h orders. This effect is illustrated in Fig. 3.23.

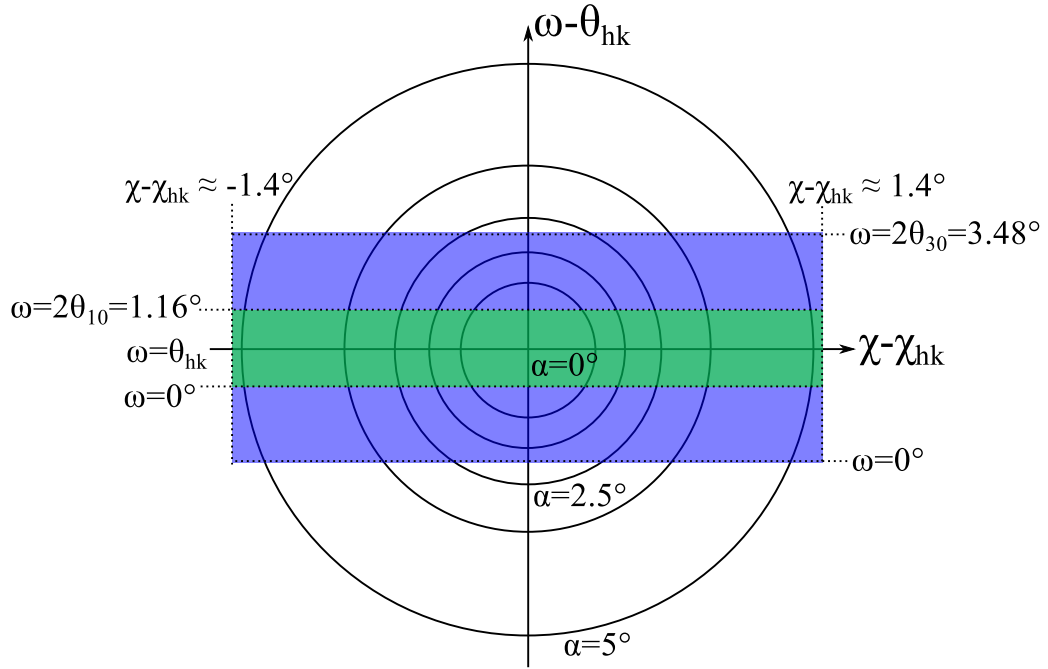


Figure 3.23: Contours of a mosaic spread distribution projected on the $\omega\chi$ -plane, where $\chi - \chi_{hk}$ is an angle measured from a (h, k) reflection on the detector ($\chi = \pi/2 - \phi$ in Fig. 3.16) and θ_{hk} is the Bragg angle for a (h, k) reflection. The distribution function takes a form of Lorentzian centered at $\alpha = 0$. Domains with $\alpha = 0$ are probed at $\omega = \theta_{hk}$ and $\chi = \chi_{hk}$. Integrated intensity of $(1, k)$ reflection arises from domains in the green shaded area while that of $(3, k)$ reflection is from the blue shaded area, which is three times larger.

We limit $\chi - \chi_{hk}$ to go from -1.4° to 1.4° . The effect of cutoff on $\chi - \chi_{hk}$ is not very important because most of observed intensity was included in integration boxes. In contrast, cutoff on ω due to substrate blocking the scattering is important, especially for lower h orders.

We take the distribution to be Lorentzian, which has been experimentally observed (REF, Dr. Nagle),

$$P(\alpha) = \frac{N}{\alpha^2 + \alpha_M^2}, \quad (3.34)$$

where N is a normalization constant and α_M is the HWHM of the distribution. N satisfies

$$N \approx \frac{1}{2\pi} \left(\int_0^{\frac{\pi}{2}} d\alpha \frac{\alpha}{\alpha^2 + \alpha_M^2} \right)^{-1}. \quad (3.35)$$

We then consider a two dimensional contour map on a $\omega\chi$ plane. Intensity for a reflection with a Bragg angle of θ_B is given by

$$I = \int_{-\theta_B}^{\theta_B} d\omega \int_{-\chi_0}^{\chi_0} d\chi P(\alpha) = \int_{-\theta_B}^{\theta_B} d\omega \int_{-\chi_0}^{\chi_0} d\chi \frac{N}{\omega^2 + \chi^2 + \alpha_M^2} \quad (3.36)$$

After the integration over χ , Eq. (3.36) is

$$I = 4N \int_0^{\theta_B} \frac{d\omega}{\sqrt{\omega^2 + \alpha_M^2}} \arctan\left(\frac{\chi_0}{\sqrt{\omega^2 + \alpha_M^2}}\right). \quad (3.37)$$

Eq. (3.37) is plotted in Fig. 3.24.

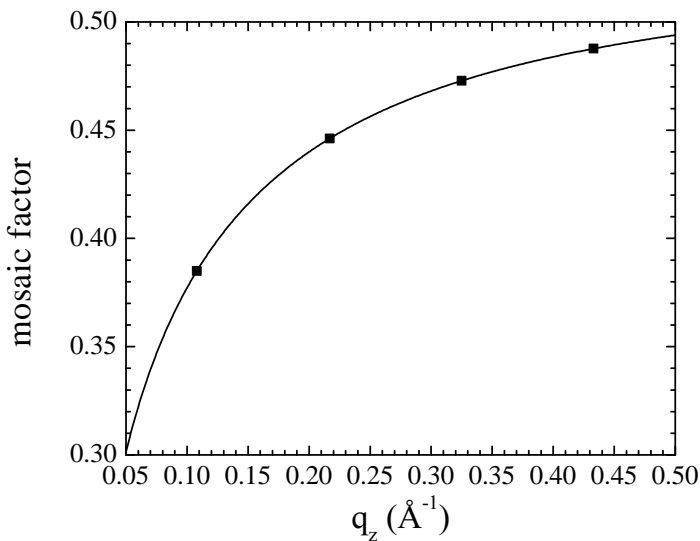


Figure 3.24: Mosaic factor given by Eq. (3.37) as a function of $q_z \approx 4\pi\theta/\lambda$. Values at $q_z = 2\pi h/D$ corresponding to $D = 57.8 \text{ \AA}$ are shown as squares. $\alpha_M = 0.05^\circ$ and $\chi_0 = 1.4^\circ$. Eq. (3.37) reaches ~ 0.54 at $\theta_B = \pi/2$ and $\chi_0 = 1.4^\circ$ and reaches ~ 1 at $\theta_B = \pi/2$ and $\chi_0 = 1.4^\circ$ as expected.

3.4 LAXS: model

3.4.1 Contour Part of the Form Factor

As in Ref. [88], we take the ripple profile to have a sawtooth profile. Its amplitude is A and the projection of the major arm on the ripple direction is x_M as shown in Fig. 3.1. Then, we write the ripple profile as

$$u(x) = \begin{cases} -\frac{A}{\lambda_r - x_0} \left(x + \frac{\lambda_r}{2} \right) & \text{for } -\frac{\lambda_r}{2} \leq x < -\frac{x_0}{2}, \\ \frac{A}{x_0} x & \text{for } -\frac{x_0}{2} \leq x \leq \frac{x_0}{2}, \\ -\frac{A}{\lambda_r - x_0} \left(x - \frac{\lambda_r}{2} \right) & \text{for } \frac{x_0}{2} < x \leq \frac{\lambda_r}{2}. \end{cases} \quad (3.38)$$

The ripple profile has inversion symmetry, so that the resulting form factor is real. A and x_M are fitting parameters that depend on the integrated intensity of each peak while D , λ_r , and γ are determined from measuring the positions of the Bragg peaks.

In order to allow the electron density along the ripple direction to modulate, we include two additional parameters, one to allow for the electron density across the minor side to be different by a ratio f_1 from the electron density across the major side and a second parameter f_2 , which is multiplied by δ functions $\delta(x \pm x_M/2)$ to allow for a different electron density near the kink between the major and the minor sides.

The contour part of the form factor F_C calculated from Eq. (3.38) is plotted in Fig. (3.25).

3.4.2 Transbilayer Part of the Form Factor

The hybrid model developed by Wiener *et al.* [104] has been successful in modeling the electron density profile in the gel phase. The hybrid model with two Gaussian functions each representing the headgroup and terminal methyl group was employed by Sun *et al.* [88] for phasing the ripple phase X-ray data published by Wack and Webb [8]. We employed the same model for fitting our data since it was shown to be very successful in fitting the ripple X-ray data. Because our data contain more data points at larger q , we also used a model that has three Gaussian functions, two of which represent the headgroup and the other one represents the terminal methyl group.

In the hybrid model, the terminal methyl region of the bilayer is represented as a

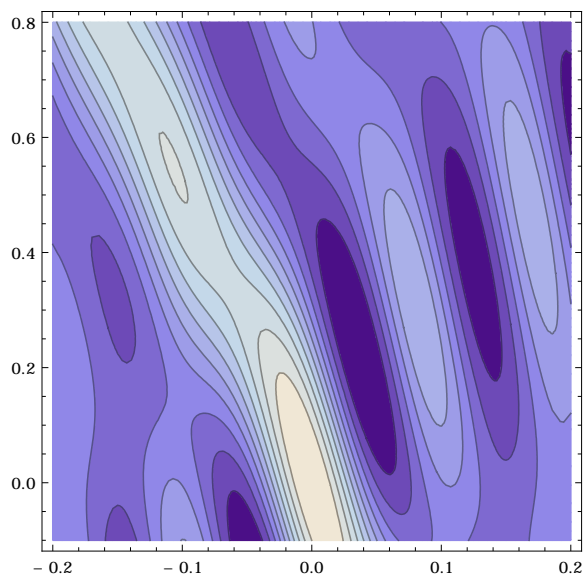


Figure 3.25: Not sure if this plot is useful. The horizontal axis is q_x and the vertical axis is q_z .

Gaussian function [104]. The headgroups are represented by one and two Gaussian functions in 1G and 2G hybrid model, respectively. The methylene and water regions are each treated as a constant. The gap between the two constants is represented by a sine function. Then, for half of the bilayer, $0 \leq z \leq D/2$, the electron density has the form,

$$\rho(z) = \rho_G(z) + \rho_S(z) + \rho_B(z), \quad (3.39)$$

where the Gaussian part is given by

$$\rho_G(z) = \sum_{i=1}^{1 \text{ or } 2} \rho_{H_i} e^{-(z-Z_{H_i})^2/(2\sigma_{H_i}^2)} + \rho_M e^{-z^2/(2\sigma_M^2)}, \quad (3.40)$$

the strip part is given by

$$\rho_S(z) = \begin{cases} \rho_{CH_2} & \text{for } 0 \leq z < Z_{CH_2}, \\ \rho_W & \text{for } Z_W \leq z \leq D/2, \end{cases} \quad (3.41)$$

and the bridging part is given by

$$\rho_B(z) = \frac{\rho_W - \rho_{CH_2}}{2} \cos\left[\frac{-\pi}{\Delta Z_H}(z - Z_W)\right] + \frac{\rho_W + \rho_{CH_2}}{2} \quad \text{for } Z_{CH_2} < z < Z_W. \quad (3.42)$$

with $\Delta Z_H = Z_W - Z_{CH_2}$. Here, we assume $Z_{H2} > Z_{H1}$. Table 3.5 shows some of the definitions.

	1G	2G
Z_{CH_2}	$Z_{H1} - \sigma_{H1}$	$Z_{H1} - \sigma_{H1}$
Z_W	$Z_{H1} + \sigma_{H1}$	$Z_{H2} + \sigma_{H2}$

Table 3.5: Definitions of Z_{CH_2} and Z_W

The transbilayer profile along $x = -z \tan \psi$ can be obtained by rotating the coordinates x and z by ψ in the clockwise direction and reexpressing $\rho(z)$ in terms of the rotated coordinates. This leads to replacing x with $x' = x \cos \psi + z \sin \psi$ and z with $z' = -x \sin \psi + z \cos \psi$. Then, the rotated transbilayer profile is

$$\rho(x, z) = \delta(x + z \tan \psi)[\rho_G(z') + \rho_S(z') + \rho_B(z')]. \quad (3.43)$$

Taking the two dimensional Fourier transform of Eq. (3.43) leads to the transbi-

layer part of the form factor,

$$F_T = \int_{-\frac{D}{2}}^{\frac{D}{2}} \int_{-\frac{\lambda_r}{2}}^{\frac{\lambda_r}{2}} [\rho(x, z) - \rho_W] e^{i(q_x x + q_z z)} dx dz \quad (3.44)$$

$$= F_G + F_S + F_B. \quad (3.45)$$

The form factor is calculated in the minus fluid convention, where the bilayer electron density is measured with respect to the electron density of the surrounding solvent. The expression for F_T is rather messy, so the derivation and full expression are in the appendix. Here, we note that the fitting parameters in this model are Z_{Hi} , σ_{Hi} , and ρ_{Hi} for each of the two headgroup Gaussian functions, σ_M and ρ_M for the terminal methyl Gaussian, ψ for the lipid tilt, and an overall scaling factor. $rhochtwo$ is absorbed into the overall scaling factor. The contour part of the form factor has four more parameters (A , x_M , f_1 , and f_2). In total, the modified 2G hybrid model implements 13 structural parameters. Generally, we made Z_{Hi} , ψ , A , x_M , f_1 , and f_2 free parameters to guide the nonlinear least square procedure to find a reasonable fit while the rest of the parameters was fixed to the corresponding gel phase values reported in Ref. [104]. Although the best estimate of the gel phase structure was reported in Ref. [53], precise values for the fixed parameters were not important because we set those fixed parameters free to find the best fit once a reasonable fit was obtained.

3.5 LAXS: results

We measured scattering on oriented samples in almost identical conditions as the best unoriented sample of Wack and Webb. As discussed earlier, these two types of samples have different Lorentz corrections, so this allowed us to check our data obtained on oriented samples against an unoriented sample. As Table 3.6 shows, agreement between our oriented data and the unoriented data was good, but form factor from our oriented sample was in many cases slightly larger than that from the unoriented sample. We attribute this discrepancy to the way intensity was extracted. In X-ray data from an oriented sample, each peak was well separated, so integrating a peak intensity was trivial. In contrast, some reflections in unoriented data were overlapping with each other (three pairs of overlapping peaks are highlighted in Table 3.6), making separation of intensity difficult. If the $(1, 0)$ peak in the unoriented data had been overestimated, that would account for the observed discrepancy. Indeed, the microdensitometer trace in [8] suggests that the $(1, 0)$ and $(1, -1)$ reflections could have similar intensity as we observed in our oriented sample. Table 3.7 and 3.8 summarize observed intensity from our data shown in Fig. 3.12. q_z values for observed peaks were corrected for index of refraction (Appendix A.6).

Table 3.9 summarizes representative fits obtained by a nonlinear least square fitting procedure. Fit1 and Fit2 were fits using the 1G hybrid model, and Fit3-Fit7 were with the 2G hybrid model. As Table 3.9 shows, Fit5 produced the smallest χ^2 value. This fit was arrived by first getting Fit3, then freeing the widths of the three Gaussian (Fit4), and finally freeing the amplitudes of the Gaussian. We also tried a different route; from Fit3, we freed up the amplitudes of the Gaussian (Fit6) and then set the widths of the Gaussian free, arriving at Fit7. While the χ^2 values of fit5 and fit7 were not very different, they resulted in $h = 6$ orders have the opposite phases as shown in Table A.2. We consistently obtained model form factors that were too small compared to the experimental ones for $(h, k) = (3, 0)$, $(6, k)$, and $(9, 0)$. This can be understood by considering the contour part of the form factor F_C given by Eq. ???. Figure ?? plots a two dimensional map of $|F_C|$ for $\lambda_r = 145 \text{ \AA}$, $A = 20 \text{ \AA}$, $x_M = 100 \text{ \AA}$, and $f_1 = f_2 = 0$. which shows that $|F_C|$ takes small values around (q_r, q_z) of $h = 3, 6$, and 9 . Because the model form factor F is the product of F_C and F_T , F is also small for the models we tried. This analysis suggests that to fit those orders better may require a different model for the contour part of the form factor

h	k	q^* (Å $^{-1}$)	unoriented $ F_{hk} ^*$	oriented $ F_{hk} $	error
1	-1	0.111	60.8	86.3	3.7
1	0	0.108	100.0	100.0	0.5
1	1	0.123	26.9	43.1	2.6
1	2			0.0	3.9
1	3	0.185	7.6	8.8	0.2
2	-2	0.224	15.1	18.0	0.6
2	-1	0.215	71.2	76.0	0.4
2	0	0.217	39.7	28.7	0.2
2	1	0.228	33.9	39.5	0.4
2	2	0.246	22.7	24.6	0.3
2	3	0.271	14.2	14.6	0.1
2	4	0.301	7.8	9.2	0.2
2	5	0.329		5.6	0.7
2	6			4.1	0.3
3	-2	0.325	29.3	33.2	0.8
3	-1	0.322	44.2	45.9	0.4
3	0	0.325	12.0	13.2	0.5
3	1			0.0	7.1
3	2	0.350	10.5	10.2	0.2
3	3	0.370	14.9	13.6	0.2
3	4	0.394	10.0	13.0	0.2
3	5			9.6	0.1
3	6			5.6	0.4

Table 3.6: Comparison of form factor obtained in two different methods.
 *Unoriented data are from Wack and Webb [8].

h	k	q_z (Å $^{-1}$)	q_r (Å $^{-1}$)	I_{hk}^{obs}	σ_I	$ F $	σ_F	box size (pixels)
1	-1	0.102	-0.043	726	63	86.3	3.7	10 × 7
1	0	0.109	0	180818	1759	100.0	0.5	10 × 7
1	1	0.114	0.043	228	28	43.1	2.6	10 × 7
1	2			0	1	0.0	3.9	
1	3	0.128	0.13	3.8	0.2	8.8	0.2	10 × 7
2	-2	0.206	-0.087	49.2	3.5	18.0	0.6	10 × 7
2	-1	0.212	-0.044	1818	20	76.0	0.4	10 × 7
2	0	0.218	0	10200	174	28.7	0.2	10 × 7
2	1	0.224	0.043	550	10	39.5	0.4	10 × 7
2	2	0.231	0.086	112	3	24.6	0.3	10 × 7
2	3	0.237	0.129	27	0.2	14.6	0.1	10 × 7
2	4	0.243	0.173	8.2	0.4	9.2	0.2	10 × 7
2	5	0.25	0.214	2.6	0.7	5.6	0.7	10 × 7
2	6	0.256	0.257	1.2	0.2	4.1	0.3	10 × 7
3	-2	0.314	-0.087	305	15	33.2	0.8	15 × 7
3	-1	0.321	-0.043	1205	22	45.9	0.4	15 × 7
3	0	0.326	0	1566	110	13.2	0.5	15 × 7
3	1			0	31	0.0	7.1	
3	2	0.339	0.086	32.4	1.6	10.2	0.2	15 × 7
3	3	0.345	0.129	39.1	0.9	13.6	0.2	15 × 7
3	4	0.352	0.172	27.7	0.7	13.0	0.2	15 × 7
3	5	0.358	0.215	12.2	0.3	9.6	0.1	15 × 7
3	6	0.364	0.258	3.5	0.5	5.6	0.4	15 × 7
4	-3	0.417	-0.131	142	8	23.0	0.6	20 × 8
4	-2	0.423	-0.087	755.4	19	42.8	0.5	20 × 8
4	-1	0.429	-0.043	429.6	34	22.6	0.9	20 × 8
4	0	0.435	0.000	1917	23	16.2	0.1	20 × 8
4	1	0.441	0.043	45.3	7.2	7.2	0.6	20 × 8
4	2	0.448	0.085	43.6	2.4	9.9	0.3	20 × 8
4	3			0	1.3	0.0	2.1	
4	4	0.461	0.173	2.1	0.4	3.0	0.3	20 × 8
4	5	0.467	0.215	3.2	0.3	4.1	0.2	20 × 8
4	6	0.473	0.259	1	1.1	2.5	1.1	20 × 8

Table 3.7: Observed intensity for $h = 1$ to 4 at $D = 57.8$, $\lambda_r = 145$, and $\gamma = 98.2^\circ$.

h	k	q_z (Å $^{-1}$)	q_r (Å $^{-1}$)	I_{hk}^{obs}	σ_I	$ F $	σ_F	box size (pixels)
5	-3	0.525	-0.132	86.2	6.8	15.6	0.6	25 × 9
5	-2	0.532	-0.087	145	4	16.3	0.2	25 × 9
5	-1	0.538	-0.042	63.4	3.4	7.5	0.2	25 × 9
5	0	0.544	0.000	260	4	6.5	0.1	25 × 9
5	1	0.550	0.040	50	2.8	6.4	0.2	25 × 9
6	-4	0.628	-0.175	11.4	0.8	5.9	0.2	30 × 10
6	-3	0.635	-0.131	15.6	0.9	5.9	0.2	30 × 10
6	-2	0.641	-0.085	10.1	1.8	3.8	0.3	30 × 10
6	-1	0.647	0.043	16.3	3	3.4	0.3	30 × 10
6	0	0.653	0.000	60.2	4.7	3.4	0.1	30 × 10
6	1	0.659	0.044	20.4	1.5	3.9	0.1	30 × 10
6	2			0	0.6	0.0	0.9	
6	3	0.672	0.128	5.9	0.3	3.5	0.1	30 × 10
6	4	0.679	0.170	4.2	0.3	3.4	0.1	30 × 10
7	-4	0.737	-0.174	40	1.1	10.0	0.1	35 × 10
7	-3	0.743	-0.130	36	1.8	8.1	0.2	35 × 10
7	-2	0.749	-0.085	15	7.3	4.2	0.9	35 × 10
7	-1	0.755	-0.042	22	2.3	3.6	0.2	35 × 10
7	0	0.760	0.000	36	1.8	2.8	0.1	35 × 10
8	0			0	3	0.0	0.9	
9	-5	0.951	-0.215	16	3	6.1	0.5	35 × 10
9	-4	0.957	-0.173	16.9	3	5.6	0.5	35 × 10
9	-3			0	8	0.0	3.3	
9	-2	0.969	-0.086	10	2.9	3.0	0.4	35 × 10
9	-1			0	6	0.0	1.7	
9	0	0.981	0.000	17	10	2.2	0.6	35 × 10

Table 3.8: Observed intensity for $h = 5$ to 9 at $D = 57.8$, $\lambda_r = 145$, and $\gamma = 98.2^\circ$ (continued from Table 3.7).

rather than trying various models for the transbilayer part of the form factor. We did not consider improving the models because we were only interested in the predicted phases for calculating an electron density profile.

Figure 3.26 plots a two dimensional electron density profile calculated using the phases obtained from Fit5 and our experimental form factors. The density profile shows presence of the terminal methyl trough in the major arm, which is manifested by a dip in the electron density along the bilayer center. To obtain the thickness of the bilayer, electron density profiles are plotted in Fig. along the slices shown by the straight dashed lines in Fig. (A and B). Slice A is along the normal of the major arm and is centered in the middle of the hydrocarbon region. It indicates that the bilayer head-head spacing $D_{\text{HH}}^{\text{major}}$ is 40 Å on the major arm. Slice B is along the normal to the minor arm and is centered in the middle of the hydrocarbon region. It indicates that

	Fit1	Fit2	Fit3	Fit4	Fit5	Fit6	Fit7
χ^2	11996	9664	19458	8827	8525	8905	8883
A	20.4	24.2	22.1	21.5	21.5	21.4	21.5
x_M	98.5	118.8	92.6	104.0	102.9	102.1	102.7
f_1	0.489	0.726	0.776	0.515	0.538	0.516	0.511
f_2	0*	-11.3	-6.06	-2.77	-2.81	-2.62	-2.63
ψ	0.266	0.250	0.183	0.252	0.252	0.263	0.259
$Z_{\text{H}1}$	19.8	19.7	18.1	19.5	18.7	19.1	19.0
$\sigma_{\text{H}1}$	3.43*	3.43*	2.94*	3.06	2.51	2.94*	2.97
$\rho_{\text{H}1}$	10.77*	10.77*	9.91*	9.91*	7.03	8.38	8.45
$Z_{\text{H}2}$	NA	NA	20.0	20.4	22.4	23.2	23.0
$\sigma_{\text{H}2}$	NA	NA	1.47*	3.17	1.38	1.47*	1.72
$\rho_{\text{H}2}$	NA	NA	7.27*	7.27*	3.75	2.83	3.00
σ_{M}	1.67*	1.67*	1.83*	2.47	2.53	1.83*	1.87
ρ_{M}	9.23*	9.23*	10.9*	10.9*	5.15	6.87	6.97

Table 3.9: Model parameters. Fit1 and Fit2 were performed with the M1G model while Fit3 to 7 were with the M2G model.

*Parameters were fixed to the values shown.

	Fit1	Fit2	Fit3	Fit4	Fit5	Fit6	Fit7
D_{HH}^{major}	42.0	41.0	40.0	40.6	40.6	41.8	41.8
D_{HH}^{minor}	30.8	31.0	29.2	29.2	29.2	31.0	31.0
α_M	11.7	11.5	13.4	11.7	11.8	11.8	11.8
α_m	23.7	42.7	22.9	27.7	27.1	26.5	26.9

Table 3.10: Ripple structural quantities.

Figure 3.26: Electron density profile calculated using the phases obtained from the M2G model and experimental form factors. White is most electron dense and black is least electron dense. The thickness along the local bilayer normal in the major arm was about 40 Å. Depletion of electron density due to the terminal methyl is visible in the major arm but not in the minor arm.

Figure 3.27: Electron density profile calculated using the phases obtained from the M2G model with $f_2 = 0$ and experimental form factors. White is most electron dense and black is least electron dense. The thickness along the local bilayer normal in the major arm was about 40 Å. Depletion of electron density due to the terminal methyl is visible in the major arm but not in the minor arm.

3.6 nGIWAXS: results

3.6.1 Fluid and gel phase

Figure 3.28 shows the data reduction of near grazing incidence wide angle X-ray scattering (nGIWAXS) data of the DMPC fluid phase at $T = 30\text{ }^{\circ}\text{C}$. The original scattering image taken at $\omega = 0.5^\circ$ had unwanted scattering due to mylar windows in the hydration chamber which overlapped with the fluid phase WAXS. Subtracting background scattering data taken at incident angle $-\omega$ removed these unwanted features in the scattering data, resulting in a sample scattering image (Fig. 3.28(bottom, left panel)). This sample scattering image was then transformed to the sample q -space using the relationship between the CCD pixel positions and the sample q -space given by Eq. 3.14 and Eq. 3.15. The nonlinearity of this relationship is not negligible and must be taken into account for wide angle scattering data. The black regions in the sample q -space image (Fig. 3.28(bottom, right panel)) are the regions of q -space that were not probed by the detector. Because of the nonlinearity in the transformation, straight detector edges were turned into curves, the effect of which was most visible near the meridian $q_r = 0$. All nGIWAXS data in this chapter were reduced in the same manner.

Because of chain disordering in the fluid phase, chain-chain scattering gives rise to intensity along an arc [105] with a broad width in q . Scattering of the fluid phase WAXS is most intense at the equator. However, scattering near the equator was strongly absorbed by the sample and substrate, so observing the peak in the fluid phase WAXS would require a different experimental geometry. The data were collected with a low resolution setup to maximize intensity. The low resolution did not pose a problem for analysis of the data because observed features were broad. Figure 3.29 plots intensity along q_r showing that the fluid phase WAXS was centered at $q \approx 1.41\text{ \AA}^{-1}$. This corresponds to an average chain-chain distance of 4.5 \AA . A Lorentzian fit to the profile resulted in the full width half maximum (FWHM) $\Delta q_r = 0.288\text{ \AA}^{-1}$.

Figure 3.30 shows nGIWAXS of the the DMPC $L_{\beta I}$ gel phase that occurs at the highest hydration [11,53], collected with the high resolution setup. Because exposure time was short, the data did not have much intensity, but the (2,0) peak was clearly visible on the equator. When the peak profile of the (2,0) peak in q_r was fitted to a Lorentzian, we obtained an excellent fit with its FWHM $\Delta q_r = 0.014\text{ \AA}^{-1}$, centered

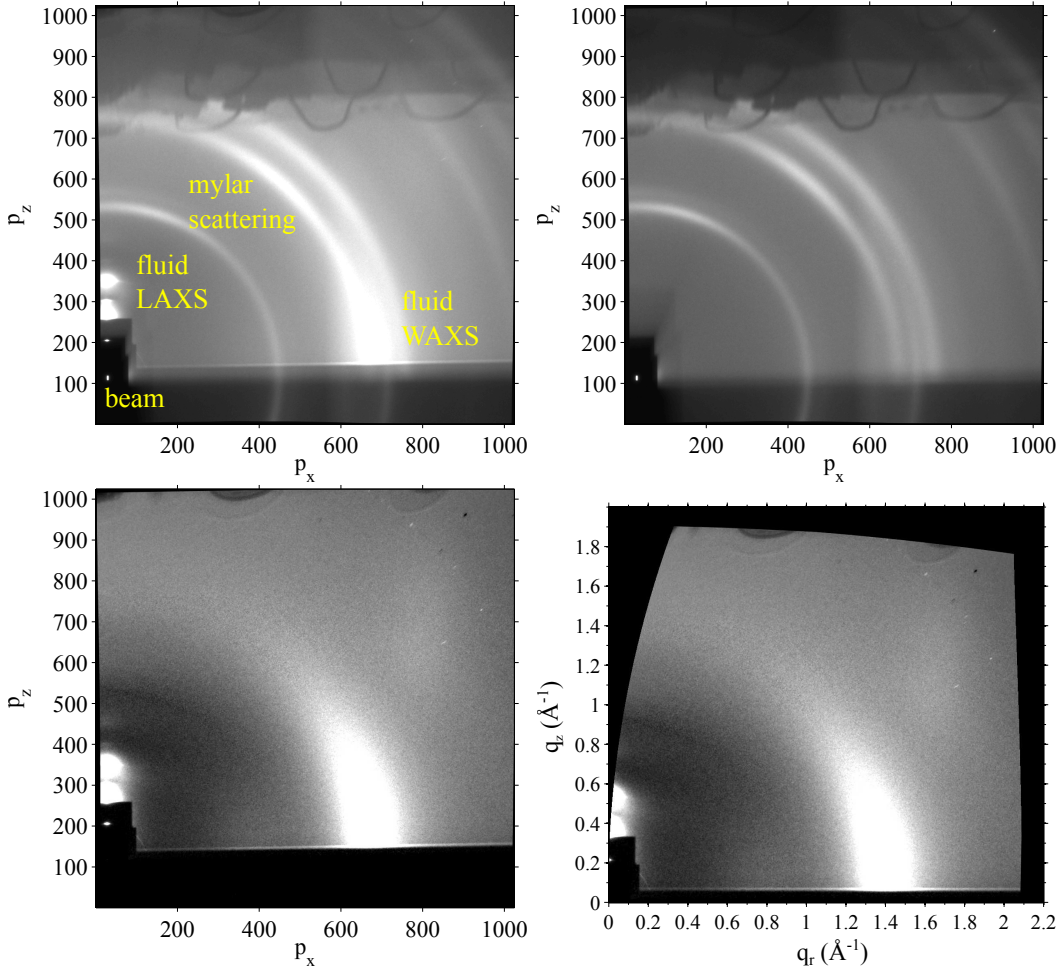


Figure 3.28: Data reduction of nGIWAXS data. (top) Fluid phase scattering at 30 °C taken at $\omega = 0.5^\circ$ (left) and at -0.5° (right) with the low resolution setup at the 2011 run. The sample width $w_s = 2$ mm. The fluid phase LAXS is also visible near the beam. The darker region below the equator defined by the beam vertical position p_z was due to the substrate. The beam was visible through the semitransparent beam stop. Scattering at $p_z > 750$ was the shadow cast by the electrical wires and thermal shielding in the hydration chamber. (bottom) The background subtracted image (left) and corresponding image in the sample q -space (right). Except some minor left over scattering, all the background scattering was removed very nicely. Because the meridian was not exactly along the vertical pixels, the background subtracted image was rotated by $\sim 1^\circ$ in the clockwise direction before the q -space transformation. The data reduction was done using MATLAB.

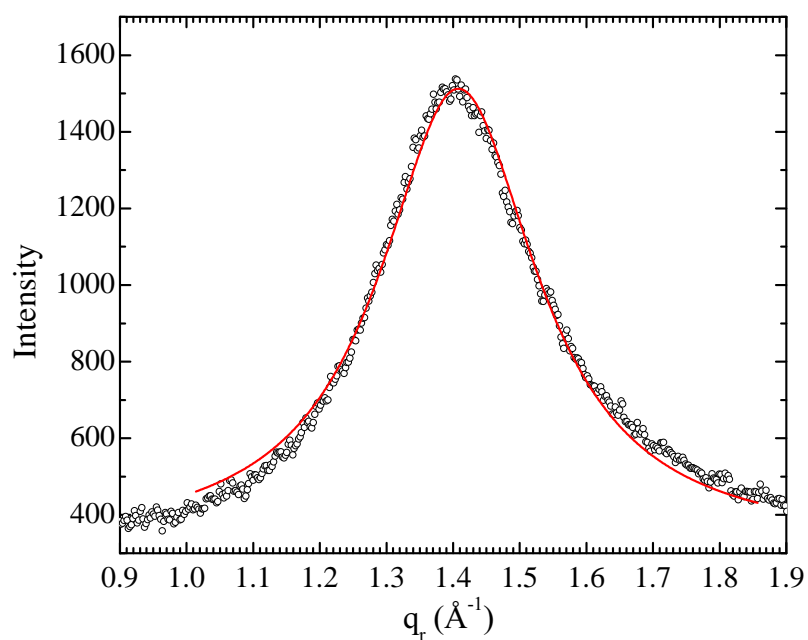


Figure 3.29: Fluid phase WAXS plotted along q_r at $q_z = 0.012 \text{ \AA}^{-1}$. The red solid line is a Lorentzian fit with its FWHM equal to 0.288 \AA^{-1} , centered at $q_r = 1.408$. Extra intensity at larger q_r was due to water scattering, which led to a slightly asymmetric profile.

at $q_r = 1.479 \text{ \AA}^{-1}$. This is the instrumental resolution as discussed in Sec. 3.2.2.3.

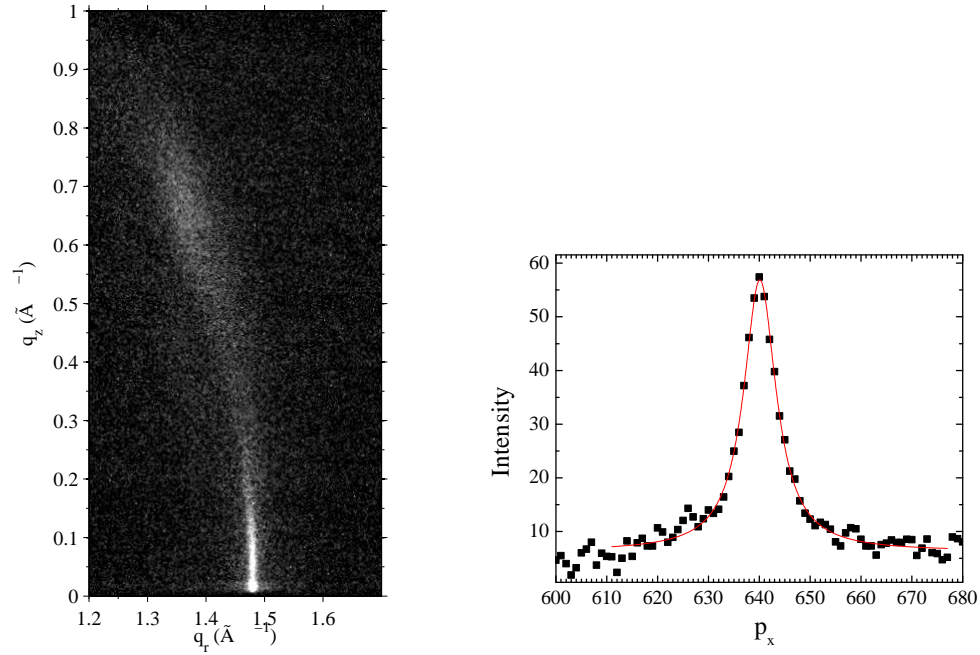


Figure 3.30: (left) nGIWAXS image of the DMPC gel phase at $10 \text{ }^\circ\text{C}$ for $D = 57.7 \text{ \AA}$ where the sample was in the $L_{\beta I}$ phase. The $(2,0)$ peak was at $q_r = 1.479 \text{ \AA}^{-1}$, corresponding to $d_{20} = 4.25 \text{ \AA}$. (right) The $(2,0)$ peak plotted along horizontal pixels p_x . The solid red line is a Lorentzian fit to the data, resulting in the FWHM of ~ 8 pixels, corresponding to $\Delta q = 0.014 \text{ \AA}^{-1}$, which is an unresolved width of intrinsically infinitely sharp peak estimated in Sec. 3.2.2.

3.6.2 Ripple phase

Figure 3.31 shows nGIWAXS from an oriented DMPC film in the ripple phase for $D = 60.8 \text{ \AA}$, collected with the high resolution setup. We observed a stronger peak and a weaker one off the equator. The maximum intensity of the stronger peak was at $(q_r, q_z) \approx (1.478 \text{ \AA}^{-1}, 0.20 \text{ \AA}^{-1})$ as shown in Fig. 3.32. The weaker peak was observed closer to the equator, and separation of this peak from the stronger one was most visible at $q_z = 0.12 \text{ \AA}^{-1}$, indicating that the center of this peak was near $(q_r, q_z) \approx (1.457 \text{ \AA}^{-1}, 0.12 \text{ \AA}^{-1})$. Because of absorption of X-rays due to the sample, intensity became attenuated as one approaches the equator. Very close to the equator, there is Vineyard-Yoneda peak that is due to constructive interference with scattering

from the substrate, which we will not consider. Absorption and Vineyard-Yoneda peak did not affect determination of the ripple peak positions as the ripple peaks were located at sufficiently large q_z . The positions of the peaks were confirmed by transmission wide angle X-ray scattering, which is discussed in the next section.

We also investigated dependence of the ripple WAXS on the interbilayer D -spacing. Figure 3.33 compares nGIWAXS at two different D -spacing, showing that chain scattering did not depend on the D -spacing in this range. A weak feature that looks like an arc coming from the chain peak was observed. This feature extended from $\phi = 0^\circ$ to at least 70° . This feature is perhaps mosaic spread scattering.

We estimated the width of the stronger peak by fitting the intensity profile in q_r to double Lorentzian as shown in Fig. 3.34. The fit resulted in the FWHM $\Delta q_r = 0.025 \text{ \AA}^{-1}$ centered at 1.478 \AA^{-1} and $\Delta q_r = 0.140 \text{ \AA}^{-1}$ centered at 1.464 \AA^{-1} . A fit with a single Lorentzian was not very good, and a broader Lorentzian was necessary to produce a reasonable fit. We also fitted the peak profile in q_r at $q_z = 0.12 \text{ \AA}^{-1}$, where two distinct peaks were observed (Fig.3.35). The two sharp peaks fitted with Lorentzian yielded the FWHM of about 0.025 \AA^{-1} , consistent with the FWHM obtained for the stronger peak. The widths and positions of the observed peaks are summarized in Table 3.11.

As Fig. 3.35 shows, the double Lorentzian fit was only successful within a limited range in q_r . This could be due to an underlining broad peak like the one shown in Fig. 3.34. To investigate this possibility, we fitted the same peak profile to triple Lorentzian with fixed widths. Two of the Lorentzian had fixed widths of 0.025 \AA^{-1} representing the sharp peaks and the last one had a fixed width of 0.14 \AA^{-1} representing the broad peak. Figure 3.35 shows an excellent fit obtained over a large range in q_r , suggesting that the estimated peak widths are not unreasonable. Curiously, the center of the stronger peak was different at the two different q_z : $(q_r, q_z) = (1.485 \text{ \AA}^{-1}, 0.12 \text{ \AA}^{-1})$ and $(1.478 \text{ \AA}^{-1}, 0.2 \text{ \AA}^{-1})$, while the total q was about the same, $\sim 1.49 \text{ \AA}^{-1}$.

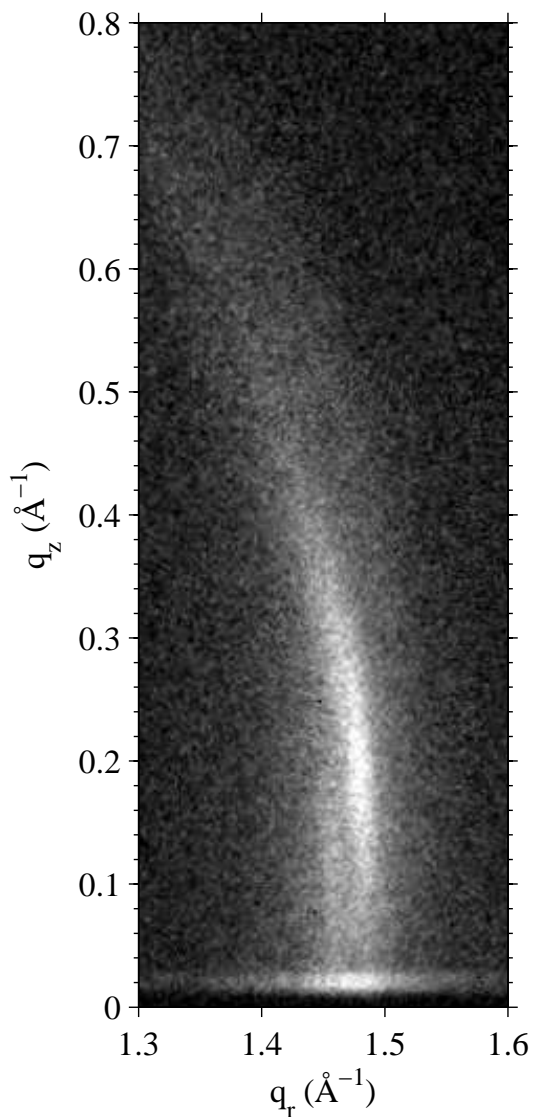


Figure 3.31: High resolution nGIWAXS of the DMPC ripple phase for $D = 60.8 \text{ \AA}$. The angle of incidence ω was 0.2° . The stronger peak was at $(q_r, q_z) \approx (1.478 \text{ \AA}^{-1}, 0.20 \text{ \AA}^{-1})$. The weaker peak was at $(q_r, q_z) \approx (1.452 \text{ \AA}^{-1}, 0.12 \text{ \AA}^{-1})$. The scattered intensity along the line slightly above $q_z = 0 \text{ \AA}^{-1}$ is the Vineyard-Yoneda peak [106, 107].

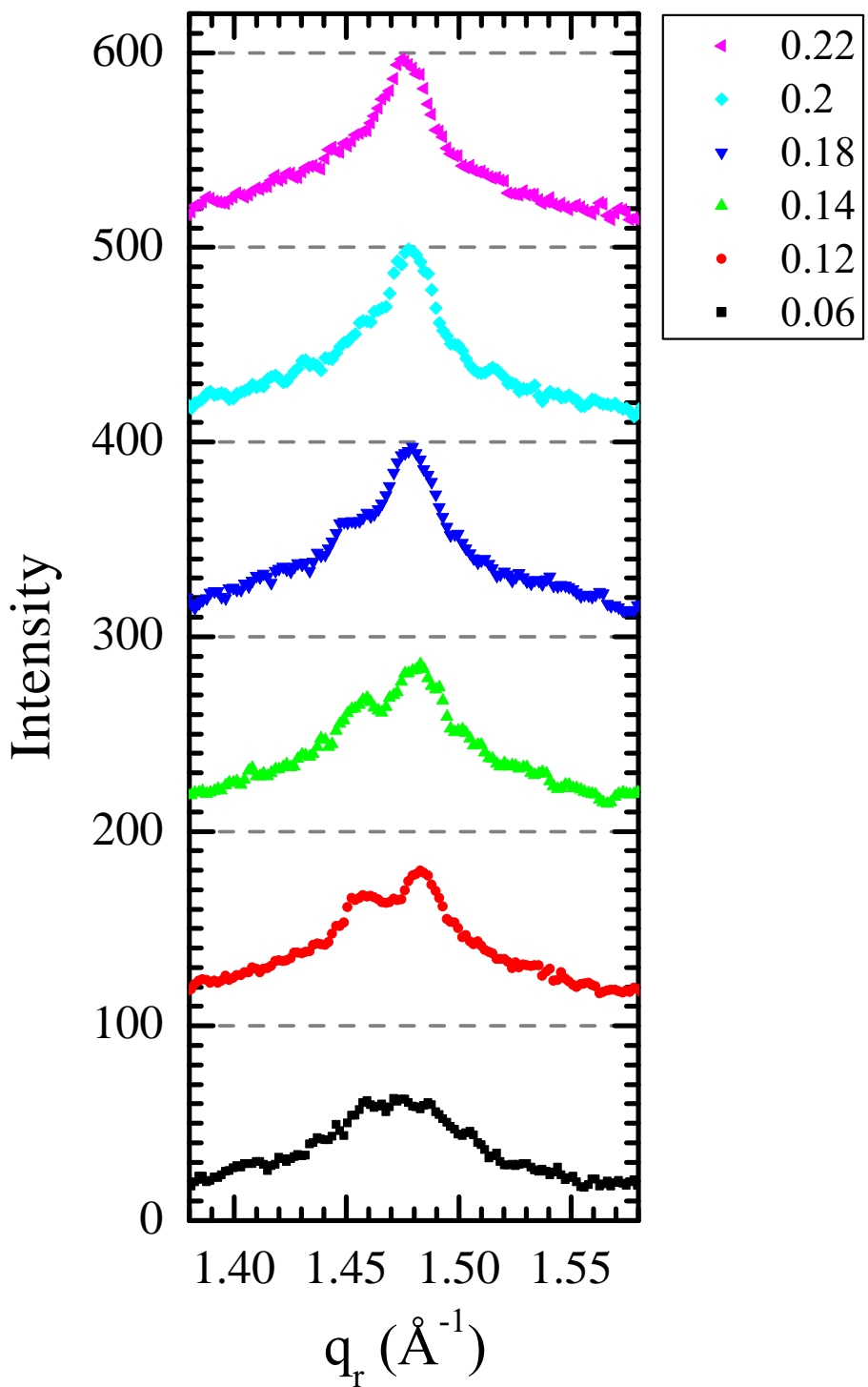


Figure 3.32: q_r swaths of the ripple WAXS, each averaged over 0.02 \AA^{-1} in q_z . Each curve is shifted by 100 vertically. The central q_z values of swaths are shown in the figure legend.

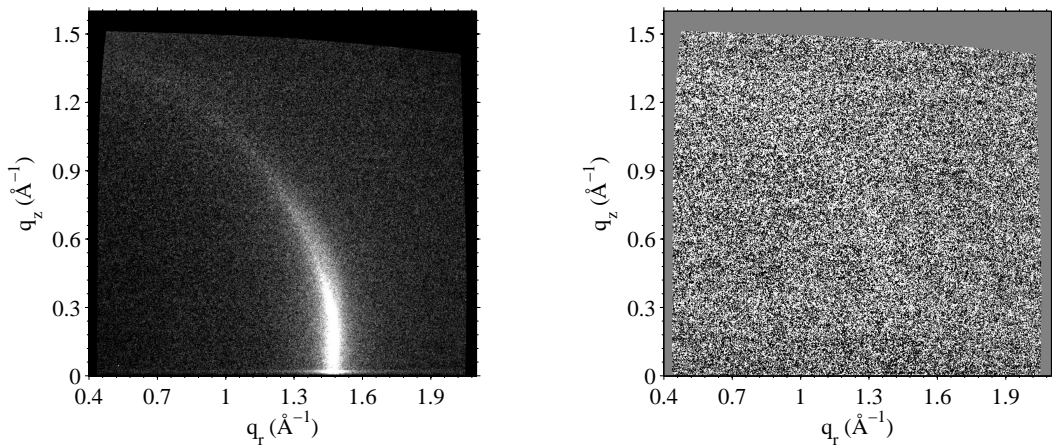


Figure 3.33: nGIWAXS of the DMPC ripple phase for $D = 59.2 \text{ \AA}$ (left) and difference between $D = 59.2 \text{ \AA}$ and 60.8 \AA (right). The difference shows no obvious feature, indicating that the ripple WAXS patterns at the two D-spacing were identical within an error. The angle of incidence ω was 0.2° . The data were taken with the high resolution setup.

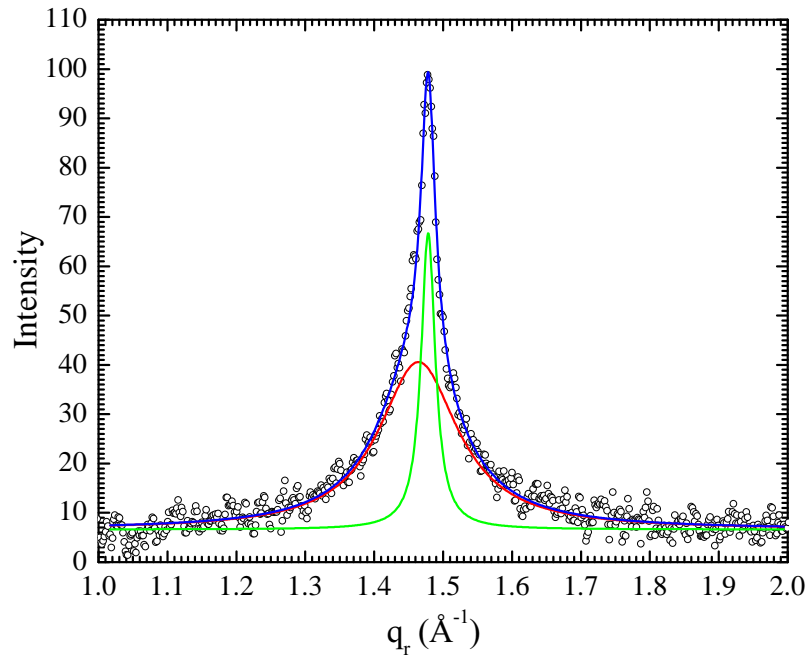


Figure 3.34: Peak profile in q_r at $q_z = 0.2 \text{ \AA}^{-1}$ fitted to double Lorentzian functions. The FWHM and center obtained were 0.025 \AA^{-1} and 1.478 \AA^{-1} (green) and 0.140 \AA^{-1} and 1.464 \AA^{-1} (red), respectively. The solid blue line is a sum of the two Lorentzian fits.

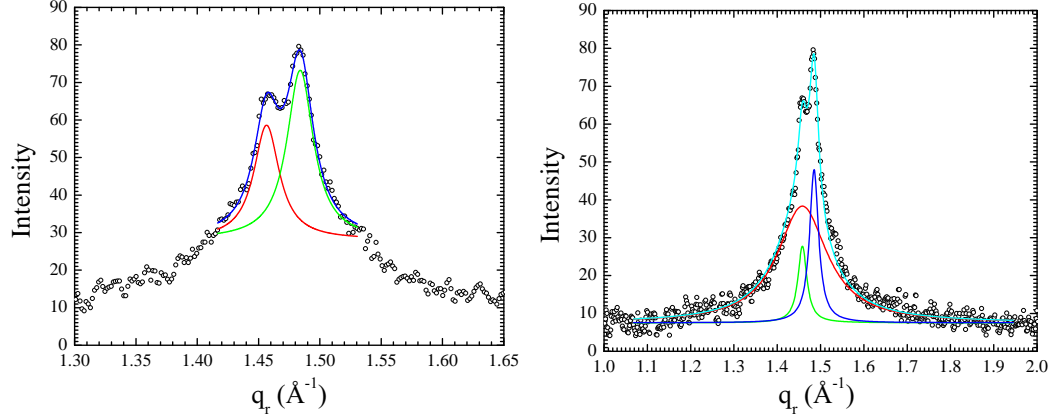


Figure 3.35: (left) Peak profile in q_r at $q_z = 0.12 \text{ \AA}^{-1}$ fitted to double Lorentzian functions. The FWHM and center obtained were 0.025 \AA^{-1} and 1.457 \AA^{-1} (red) and 0.026 \AA^{-1} and 1.484 \AA^{-1} (green), respectively. The fit was limited within a range in which fits were reasonable. (right) The same peak profile fitted to triple Lorentzian. The FWHM was constrained to 0.025 \AA^{-1} (blue), 0.025 \AA^{-1} (green), and 0.14 \AA^{-1} (red). The center was found to be 1.485 \AA^{-1} (blue), 1.458 \AA^{-1} (green), and 1.458 \AA^{-1} (red).

peaks	q (\AA^{-1})	q_r (\AA^{-1})	q_z (\AA^{-1})	Δq_r (\AA^{-1})	Δq_z (\AA^{-1})	$\hat{\theta}$
stronger	1.491	1.478	0.20	0.025	0.4	7.7°
weaker	1.462	1.457	0.12	0.025		4.7°
broader	1.463-1.478	1.458-1.464	0.12-0.20	0.140		
gel (2,0)	1.479	1.479	0	0.014	0.4	0°
fluid	1.41				0.288	

Table 3.11: Summary of measured peak properties. The values of Δq_z are from Sec. 3.7. $\hat{\theta} = \arctan(q_z/q_r)$. $R = I_{\text{strong}}/I_{\text{weak}} \approx 1.5-1.85$.

3.7 TWAXS: results

Figure 3.36(left) shows background subtracted transmission wide angle X-ray scattering (TWAXS) of the DMPC gel $L_{\beta I}$ phase obtained at $\omega = 45^\circ$. The background scattering image was collected by replacing the sample with a bare Si wafer. Imperfect subtraction of mylar scattering can be seen in the background subtracted image. This was most likely due to slight displacement of mylar windows when the sample was replaced with a bare wafer. Three main reflections whose Miller indices are (2,0), (1,1), and (1,-1) were observed along with the (1, ± 1) satellite peaks. Because the data were taken at $\omega = 45^\circ$, the WAXS pattern appeared on the CCD detector very differently from the respective pattern in the sample q -space. Therefore, the CCD to q -space transformation shown in Fig 3.36(right) was important in analyzing the TWAXS data.

Figure 3.37 shows the TWAXS pattern of the ripple phase after the CCD to q transformation. The stronger peak observed in nGIWAXS was also observed at approximately the same location. Because of a lower instrumental resolution than in the nGIWAXS experiment, the weaker peak was not as well separated. Figure 3.38 shows a hint of the weak peak at $q_z = 0.12 \text{ \AA}^{-1}$. This data set taken in the 2011 run motivated me to try an experiment with a higher instrumental resolution, which led to the nGIWAXS experiment in the 2013 run.

The length L of scattering entities in the z direction can be estimated by measuring the full length Δq_z of the (2,0) Bragg rod in q_z in the $L_{\beta I}$ phase [108], the relation between them being $\Delta q_z = 4\pi/L$. Figure 3.39 shows intensity of observed Bragg rods along q_z averaged in q_r for the gel and ripple phases. The full length Δq_z for the (2,0) gel phase peak was measured to be about 0.4 \AA^{-1} , corresponding to $L \approx 31 \text{ \AA}$. This value of L indicates that chains in the upper and lower monolayers scatter coherently, which has been shown to be the case for DPPC previously [108]. Figure 3.39(right) compares Δq_z in the ripple and gel phases, showing that Δq_z was about the same in both phases. Therefore, chains in the major arm are also coupled between the monolayers. We note that mosaic spread of the sample would make the apparent Δq_z larger, so that $L \approx 31 \text{ \AA}$ might be the lower bound on the true L .

Finally, Fig. 3.40 plots q_z swath along the weaker Bragg rod and along the entire ripple WAXS pattern. We found no obvious intensity maxima below $q_z = 0.12 \text{ \AA}^{-1}$, asserting that the weaker peak was also off the equator as discussed in Sec. 3.6. We

also found no sign of a third peak.

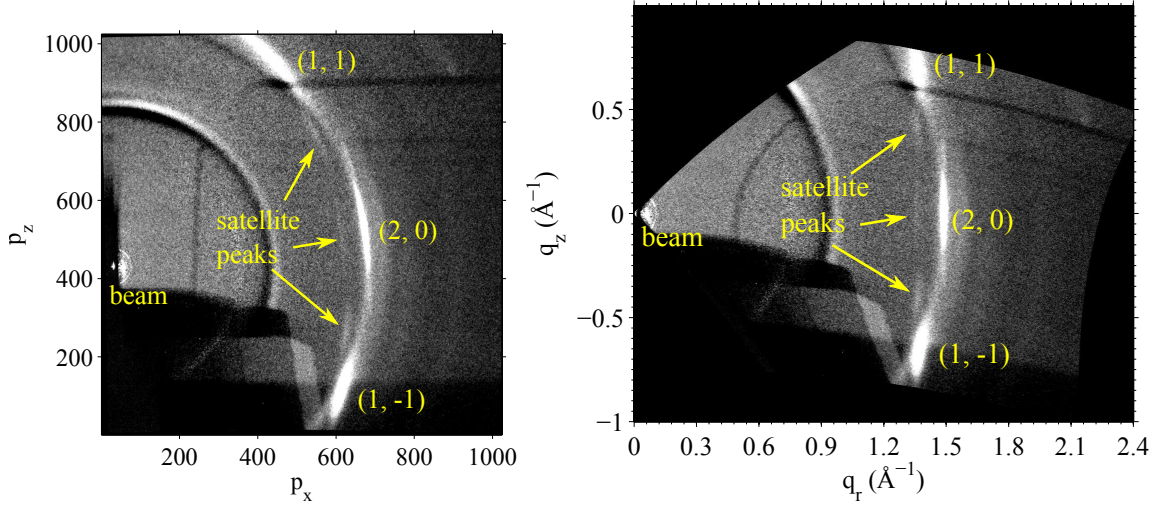


Figure 3.36: Transmission WAXS of the DMPC gel $L_{\beta I}$ phase observed on the CCD detector (left) and its corresponding pattern in the sample q -space (right). Bragg rods were indexed as $(2,0)$, $(1,1)$ and $(1,-1)$. The satellite peaks of $(1,\pm 1)$ reflections were also labeled. The black region in the right image corresponds to q -space that was not probed. The edges of the sample q -space image were distorted due to the nonlinear relation between the detector pixels and the sample q -space as discussed in Sec. 3.6. A ring of intensity at $q \approx 0.9 \text{ \AA}^{-1}$ is due to imperfect subtraction of the mylar scattering. Residual mylar scattering is also visible near the $(2,0)$ Bragg rod.

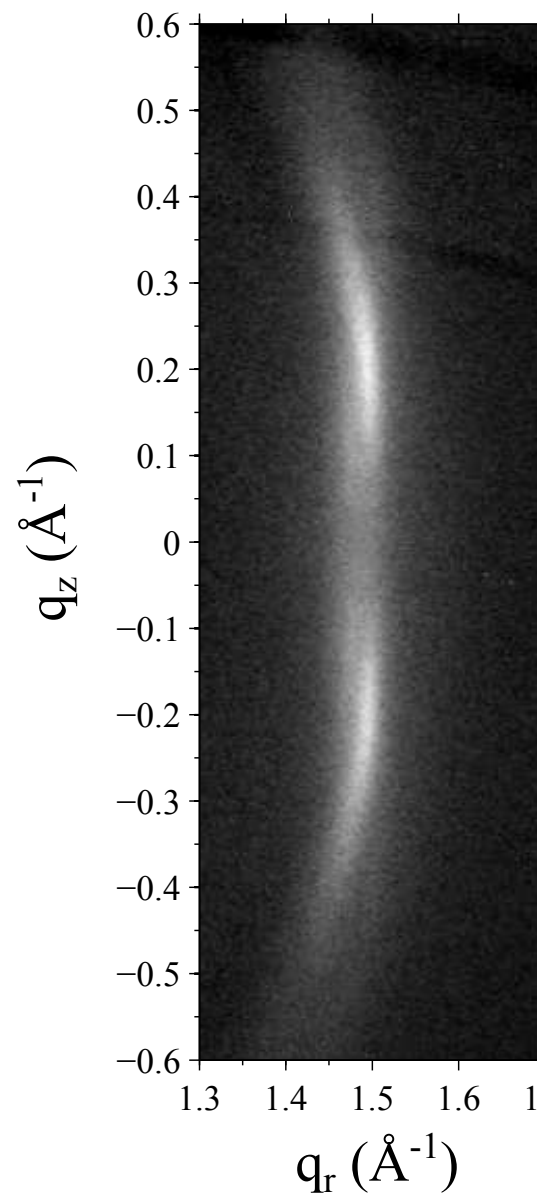


Figure 3.37: TWAXS image of the DMPC ripple phase at 18 °C and $D = 60.3 \text{ \AA}$.

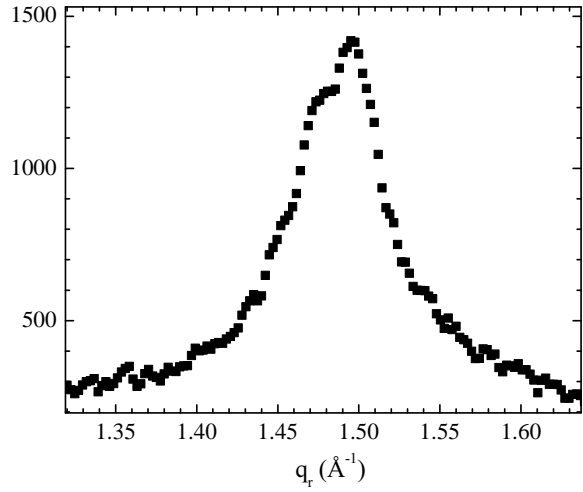


Figure 3.38: q_r swath of the ripple TWAXS averaged between 0.11 \AA^{-1} and 0.13 \AA^{-1} in q_z . Asymmetric shape of the profile is due to two Bragg rods centered at different q_r values as discussed in Sec. 3.6.

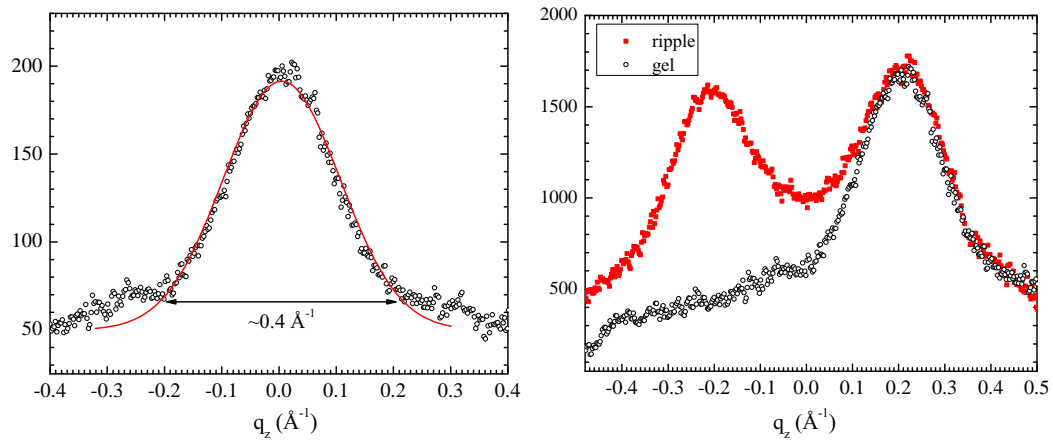


Figure 3.39: (left) q_z swath of the gel (2,0) Bragg rod. The solid line is a Gaussian fit with the FWHM of 0.23 \AA^{-1} . (right) q_z swath of the ripple peak averaged between 1.465 \AA^{-1} and 1.481 \AA^{-1} in q_r (red solid squares) and the gel (2,0) peak scaled and shifted to guide visual comparison (open black circles).

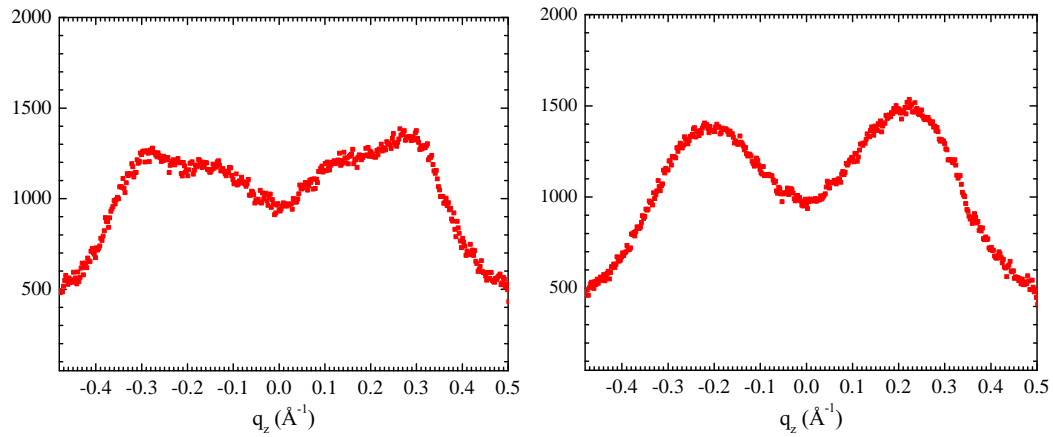


Figure 3.40: q_z swath averaged between 1.465 \AA^{-1} and 1.481 \AA^{-1} (left) and between 1.465 \AA^{-1} and 1.51 \AA^{-1} (right) in q_r . The left plot is approximately the q_z profile along the weaker peak while the right profile extends over the entire ripple WAXS pattern.

3.8 Discussion

The chain-chain correlation length can be estimated by using the Scherrer equation [109],

$$B = \frac{0.94\lambda}{L \cos \theta},$$

where B is the observed FWHM of a Bragg peak, λ is the wavelength, L is the length over which chains are positionally correlated, and θ is the Bragg angle. For $\Delta q = 0.014 \text{ \AA}^{-1}$, $q = 1.479 \text{ \AA}^{-1}$, and $\lambda = 1.175 \text{ \AA}$, the Scherrer equation yields $L = 426 \text{ \AA}$. Because the width of the (2,0) gel phase peak was not instrumentally resolved, the correlation length of chains was greater than 426 \AA . The width of similar lipid, DPPC, was resolved and had a correlation length of 2900 \AA [110].

In contrast, the observed peaks in the ripple phase were instrumentally resolved (Fig. 3.34). The FWHM of the stronger peak was estimated to be 0.025 \AA^{-1} , corresponding to the correlation length of $\sim 240 \text{ \AA}$, indicating that the correlation length in the ripple phase is shorter than that in the gel phase. This observation can be understood by supposing that chains in the major and minor arms are not correlated, so that gel phase like chains in the major arm are only correlated within the major arm, limiting the correlation length along the ripple direction to be less than the length of the major arm, $\sim 100 \text{ \AA}$. Although it is possible that chains are correlated over a much longer distance along the direction perpendicular to the ripple direction leading to a sharp reflection along q_y , what is observed in our in-plane powder sample is a convolution of a broad width along q_x and sharp one along q_y . Such convolution would result in a broad Bragg rod as observed in our nGIWAXS data.

The ripple phase has attracted many researchers since its discovery in 1967, and extensive study on average structural properties such as the ripple wavelength, oblique angle, D -spacing, and electron density profiles have been reported. From those experimental measurements, many theoretical models to explain the origin of the ripple phase have been considered. Yet, chain packing for the asymmetric ripple has only been elusive. For example, based on the calculated electron density profile, Sun *et al.* [88] has suggested that the chains in the major arm are gel phase like while those in the minor arm are disordered like in the fluid phase. Sengupta *et al.* [96] has argued, also based on the electron density profile calculated using the X-ray data by Wack and Webb [8], that chains are packed like in the gel phase throughout both arms with the same tilt angle with respect to the stacking z direction. Since the millennium,

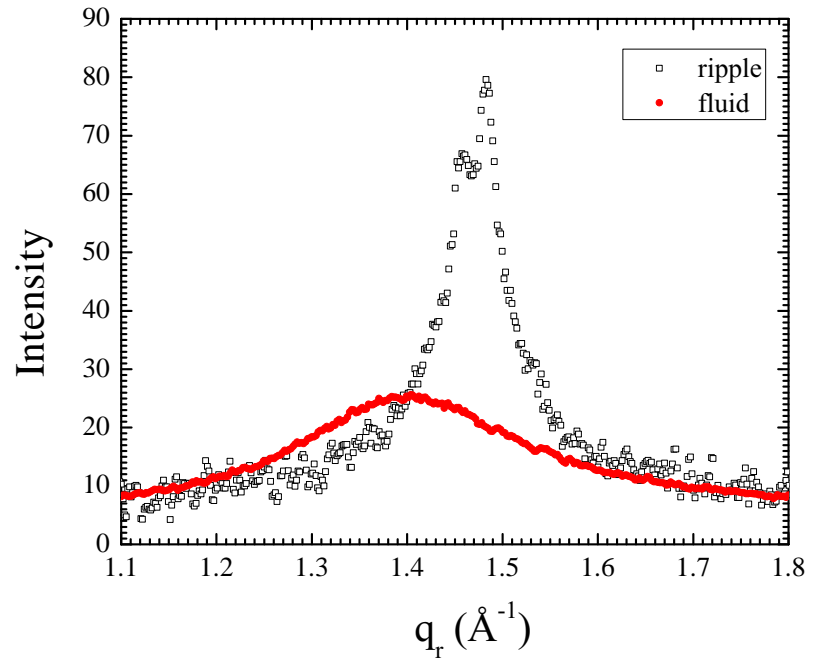


Figure 3.41: Comparison of the ripple (black) and fluid (red) phase WAXS at $q_z = 0.012 \text{\AA}^{-1}$. The fluid phase data were taken with the low resolution setup and scaled vertically to enable visual comparison.

a few simulations have predicted a different type of chain packing. For example, all atomistic simulations done by de Vrie *et al.* [98] have predicted existence of interdigitated state in the minor arm of the DMPC asymmetric ripple while lipids in the major arm are packed like in the gel phase with the monolayers decoupled from each other.

Previous predictions and suggestions so far have not been able to directly be verified because of the lack of quantitative wide angle scattering data. Although the DMPC WAXS was measured by Katsaras and Raghunathan [101] using a rotating anode, the wide angle peak measured was broad and ambiguous to answer the question of lipid packing. Therefore, we sought to fill the gap with synchrotron X-ray techniques. Our strength were three fold: 1) brilliant synchrotron beam that allowed use of Si monochromater with a very small energy dispersion, 2) stacks of \sim 2000 bilayers oriented on the substrate that scattered strongly and anisotropically, and 3) hydration chamber that allowed us to control the hydration of the sample.

By careful analysis of low angle X-ray scattering data, we have shown that chains in the major arm are straightened like in the gel phase, the finding of which is consistent with previous publications. The thickness of the major arm was measured to be 40 Å, slightly larger than the previously published value of 37.9 Å [88]. The electron density profile in the minor arm we obtained was similar to that of interdigitated chains. However, the wide angle X-ray scattering data is inconsistent with this. As de Vries *et. al.* calculated, interdigitated chains in the minor arm would result in a wide angle peak at $q_z \approx 0.5 \text{ \AA}^{-1}$, much larger q_z than 0.2 \AA^{-1} that we observed.

By comparing the wide angle pattern from the ripple and fluid phases, we showed that scattering intensity around 1.4 \AA^{-1} in the ripple phase is probably the tail of the stronger peak coming from the major arm and not due to the fluid-like chain packing in the minor arm.

Given existence of gel-like packing in the major arm, we argue that the stronger peak observed in the nGIWAXS data is the Bragg rod from the major arm. It is not clear, however, whether or not the weaker peak is also due to packing in the major arm. Resolving this issue seems to require modeling of various types of chain packing for both major and minor arms.

3.9 Conclusion

We have attempted to solve the lateral structure of the lipids within the bilayer using synchrotron X-rays. While we could not calculate the electron density profile unambiguously or solve the chain packing based on the measured wide angle scattering data, previously suggested structure of the ripple phase can be tested against our data. For example, Monte Carlo simulations based on a model free energy can be tuned to obtain a good fit to our measured wide angle data. One could also consider some exotic packing such as swirling pattern observed by Watkin et al. (PNAS) or tilt modulation field. Predicting the scattering intensity pattern from these structures might lead to a different way to analyze our LAXS and nGIWAXS data and possibly more improved study of the ripple phase.

Future possible experiments include a high resolution transmission experiment, where both geometric broadening and energy dispersion are minimized. The expected resolution is the width of the X-ray beam, which is about 3 pixels. This experiment doubles the best resolution achieved in this work. Another slightly different high resolution experiment is to use silicon crystal analyzer downstream of the sample, which completely remove geometric broadening. The downside of this type of high resolution experiment is that only one point in q-space is probed at any given exposure, so getting a full 2D map of wide angle scattering is time consuming.

Also highly speculative, but the ripple phase might be an interesting phase to study curvature sensing peptides. The description of curvature in the ripple phase has been around for a while. Those curvature sensing peptides may accumulate at the kink regions. Then, the electron density profile can be calculated with the analysis detailed in this work. It would be very interesting if peptide-lipid interactions also significantly modify the wide angle pattern. With a known perturbation property of a peptide on lipids, it could shed light on the structure of the minor arm. For example, if indeed chains are fluid like in the minor, some peptides might have tendency to accumulate in the minor arm because of ease of insertion compared to the gel-like major arm. Then, the ripple phase might be used to study biologically relevant problems.

Appendices

Appendix A

A.1 Mosaic Spread for NFIT analysis

First we calculate how mosaic spread affects the structure factor $S(q)$. Next we discuss two experimental methods. Third, we discuss the updated NFIT program. Fourth, we show the results.

A.1.1 Mosaic Spread: Calculation

In this section, an analytical framework for dealing with mosaic spread is developed. A sample of oriented stacks of bilayers consists of many small domains, within which layers are registered in an array. An ideal domain is a domain where the layers are parallel to the substrate, whose surface is in the sample xy -plane, so the orientation \mathbf{n} of an ideal domain is perpendicular to the substrate as shown in Fig. A.1. In general, the orientation \mathbf{n}' of a domain is tilted from that of an ideal domain by some angle α . Then, we consider a mosaic spread distribution function, $P(\alpha)$, representing a probability of finding a domain with a tilt α . We assume that the sample is symmetric about the substrate normal, so that the distribution $P(\alpha)$ does not depend on the azimuthal angle, β . The normalization condition on $P(\alpha)$ is

$$1 = \int_0^{2\pi} d\beta \int_0^{\frac{\pi}{2}} d\alpha \sin \alpha P(\alpha). \quad (\text{A.1})$$

The object of this section is to derive the X-ray scattering structure factor including the distribution function $P(\alpha)$.

First, let us consider a two dimensional example. Our sample consists of two identical domains except a tilt α shown in Fig. A.2. Then, the sample structure

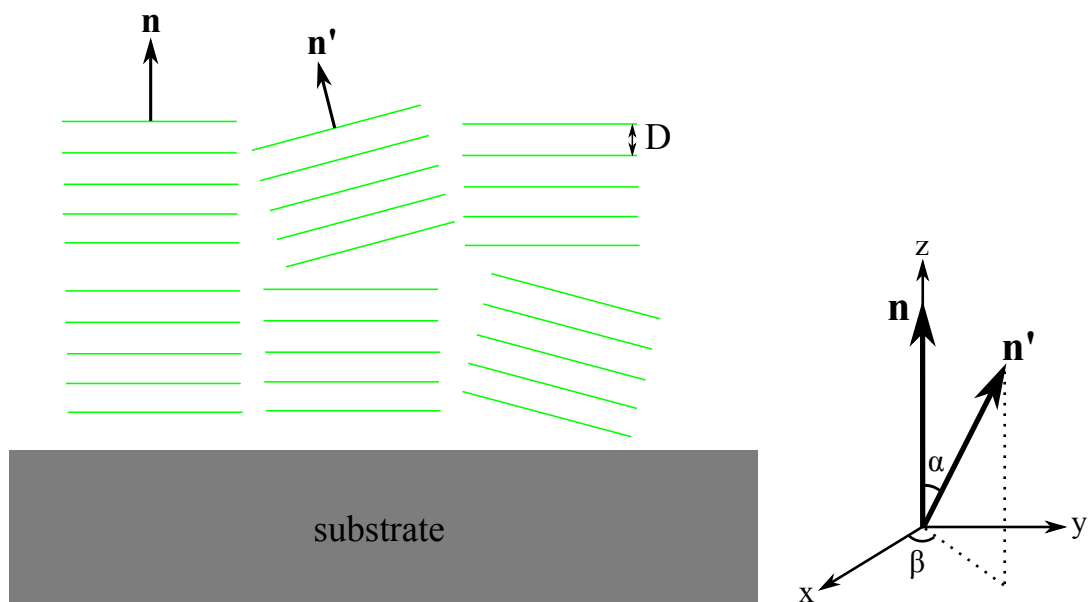


Figure A.1: Two dimensional view of mosaic spread (left) and notations used in this section (right). The stacking direction of an ideal domain is \mathbf{n} and that of a tilted domain \mathbf{n}' . The deviation of \mathbf{n}' from \mathbf{n} denoted as α quantifies the degree of misorientation of a domain. The x , y , and z -axes are the sample coordinates.

factor $S^{\text{sam}}(\mathbf{q})$ is a superposition of the structure factor $S(\mathbf{q})$ of the ideal domain and $S(\mathbf{q}')$ of the tilted domain,

$$S^{\text{sam}}(\mathbf{q}) = S(q_x, q_z) + S(q'_x, q'_z). \quad (\text{A.2})$$

To express $S(q'_x, q'_z)$ in terms of the sample q -space (q_x, q_z) , we write q'_x and q'_z in terms of q_x , q_z , and α ,

$$\begin{aligned} q'_x &= \mathbf{q} \cdot \hat{\mathbf{x}}' = q \cos\left(\frac{\pi}{2} - \theta + \alpha\right) \\ q'_z &= \mathbf{q} \cdot \hat{\mathbf{z}}' = q \sin\left(\frac{\pi}{2} - \theta + \alpha\right) \\ q_x &= q \cos(\pi/2 - \theta) \\ q_z &= q \sin(\pi/2 - \theta) \end{aligned} \quad (\text{A.3})$$

where $q = |\mathbf{q}|$. Eq. (A.2) and (A.3) give the structure factor of a sample consisting of the two domains. With a continuous distribution of \mathbf{n}' , we integrate over the angle α with each structure factor modulated by the distribution function $P(\alpha)$,

$$S_M(\mathbf{q}) = S_M(q, \theta) = \int_{-\frac{\pi}{2}}^{\frac{\pi}{2}} d\alpha S(q'_x, q'_z) P(\alpha), \quad (\text{A.4})$$

Variables q and θ are used in the above equation to make a connection with the three dimensional case, where the spherical coordinates are convenient, which we discuss now.

For a three dimensional sample, the basic idea is the same as the two dimensional case. In the three dimensional case, we also rotate the vector \mathbf{n}' about the z -axis by an angle β after the rotation about the y -axis by an angle α , so all we need to do is to apply appropriate rotation matrices to the sample xyz -axes which define the domain coordinates $x'y'z'$.

The rotation matrix for rotating a vector about the y -axis is given by

$$R_y = \begin{pmatrix} \cos \alpha & 0 & \sin \alpha \\ 0 & 1 & 0 \\ -\sin \alpha & 0 & \cos \alpha \end{pmatrix} \quad (\text{A.5})$$

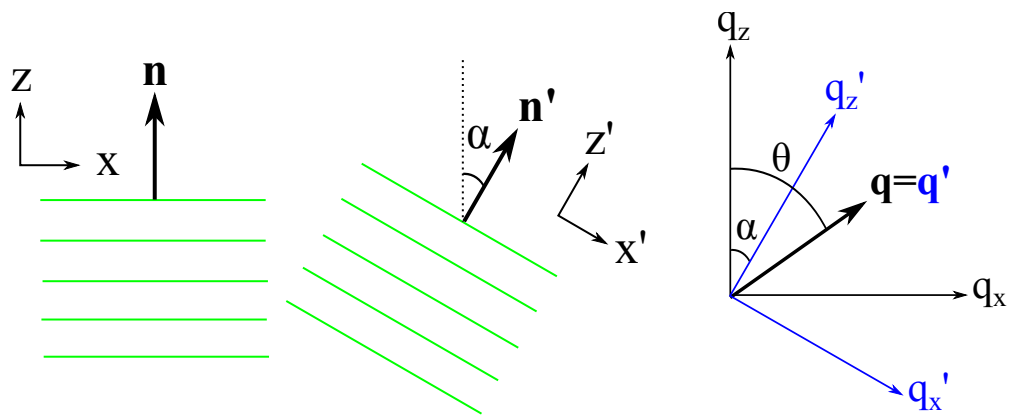


Figure A.2: Example of a two dimensional sample consisting of an ideal and tilted domains. $\mathbf{q} = (q_x, q_z)$ is the sample q -space and $\mathbf{q}' = (q'_x, q'_z)$ is the domain q -space. The two q -spaces are related by a rotation of α about the y -axis, which is into the page.

and for rotating about the z -axis

$$R_z = \begin{pmatrix} \cos \beta & -\sin \beta & 0 \\ \sin \beta & \cos \beta & 0 \\ 0 & 0 & 1 \end{pmatrix}. \quad (\text{A.6})$$

Then, what we want is

$$\hat{\mathbf{x}}' = R_z R_y \begin{pmatrix} 1 \\ 0 \\ 0 \end{pmatrix} = \begin{pmatrix} \cos \alpha \cos \beta \\ \cos \alpha \sin \beta \\ -\sin \alpha \end{pmatrix} \quad (\text{A.7})$$

$$\hat{\mathbf{y}}' = R_z R_y \begin{pmatrix} 0 \\ 1 \\ 0 \end{pmatrix} = \begin{pmatrix} -\sin \beta \\ \cos \beta \\ 0 \end{pmatrix} \quad (\text{A.8})$$

$$\hat{\mathbf{z}}' = R_z R_y \begin{pmatrix} 0 \\ 0 \\ 1 \end{pmatrix} = \begin{pmatrix} \sin \alpha \cos \beta \\ \sin \alpha \sin \beta \\ \cos \alpha \end{pmatrix}. \quad (\text{A.9})$$

The domain q -space, (q'_x, q'_y, q'_z) , in terms of the sample q -space (q_x, q_y, q_z) is given by

$$q'_x = \mathbf{q} \cdot \hat{\mathbf{x}}' = q_x \cos \alpha \cos \beta + q_y \cos \alpha \sin \beta - q_z \sin \alpha, \quad (\text{A.10})$$

$$q'_y = \mathbf{q} \cdot \hat{\mathbf{y}}' = -q_x \sin \beta + q_y \cos \beta, \quad (\text{A.11})$$

$$q'_z = \mathbf{q} \cdot \hat{\mathbf{z}}' = q_x \sin \alpha \cos \beta + q_y \sin \alpha \sin \beta + q_z \cos \alpha. \quad (\text{A.12})$$

The transformation expressed in the spherical coordinates is

$$\cos \theta' = \frac{q'_z}{q} = \sin \theta \sin \alpha \cos(\phi - \beta) + \cos \theta \cos \alpha, \quad (\text{A.13})$$

$$\tan \phi' = \frac{q'_y}{q'_x} = \frac{\sin \theta \sin(\phi - \beta)}{\sin \theta \cos \alpha \cos(\phi - \beta) - \cos \theta \sin \alpha}. \quad (\text{A.14})$$

Summing over all the domains, we get for the mosaic spread modified structure factor

$$S_M(q, \theta, \phi) = \int_0^{2\pi} d\beta \int_0^{\frac{\pi}{2}} d\alpha S(q, \theta', \phi') P(\alpha) \quad (\text{A.15})$$

with Eq. (A.13) and Eq. (A.14).

To test these equations, let us apply them to the simple case of a stack of rigid layers with their normals parallel to the z -axis in spherical coordinates. The structure factor is then

$$S(q, \theta, \phi) = \frac{\delta(q - \frac{2\pi h}{D})}{q^2} \delta(\cos \theta - 1) \delta(\phi) \quad (\text{A.16})$$

where $\delta(x)$ is the Dirac delta function. From Eq. (A.14), $\delta(\phi')$ is equivalent to $\delta(\beta - \phi)$. Setting $\beta = \phi$ in Eq. (A.13) gives $\cos \theta' = \cos(\alpha - \theta)$. Then, the mosaic spread modified structure factor $S_M(\mathbf{q})$ is

$$\begin{aligned} S_M(q, \theta, \phi) &= \int d\alpha \int d\beta \frac{\delta(q - \frac{2\pi h}{D})}{q^2} \delta(\cos \theta' - 1) \delta(\beta - \phi) P(\alpha) \\ &= \frac{\delta(q - \frac{2\pi h}{D})}{q^2} \int d\alpha \delta(\cos[\alpha - \theta] - 1) P(\alpha) \\ &= \frac{\delta(q - \frac{2\pi h}{D})}{q^2} P(\theta). \end{aligned} \quad (\text{A.17})$$

Eq. (A.17) describes hemispherical shells with radii of $2\pi h/D$ in the sample q -space. As will be described in the next section, a 2D detector records cross sections of these shells, which give rise to mosaic arcs along $q = 2\pi h/D$.

The structure factor of thermally fluctuating layers is not simple delta functions and gives rise to diffuse scattering. Analysis of the diffuse scattering from a sample with mosaic spread requires Eq. (A.15).

A.1.2 Mosaic Spread: Near Equivalence of Two Methods

In this section, we discuss experimental procedures to probe appropriate q -space to measure the mosaic spread distribution, $P(\alpha)$. In our setup, the angle of incidence between the beam and substrate, denoted by ω , can be varied. A conventional method to measure $P(\alpha)$ is a rocking scan, where one measures the integrated intensity of a given Bragg peak as a function of ω with a fixed detector position. Another method that takes an advantage of an area detector [111] measures the intensity as a function of χ on a two dimensional detector (see Fig. A.3). This method has been used to quantify complete pole figures for thin films with fiber texture (isotropic in-plane orientation) [112]. First, we want to compare the two methods mentioned above and determine their relationship.

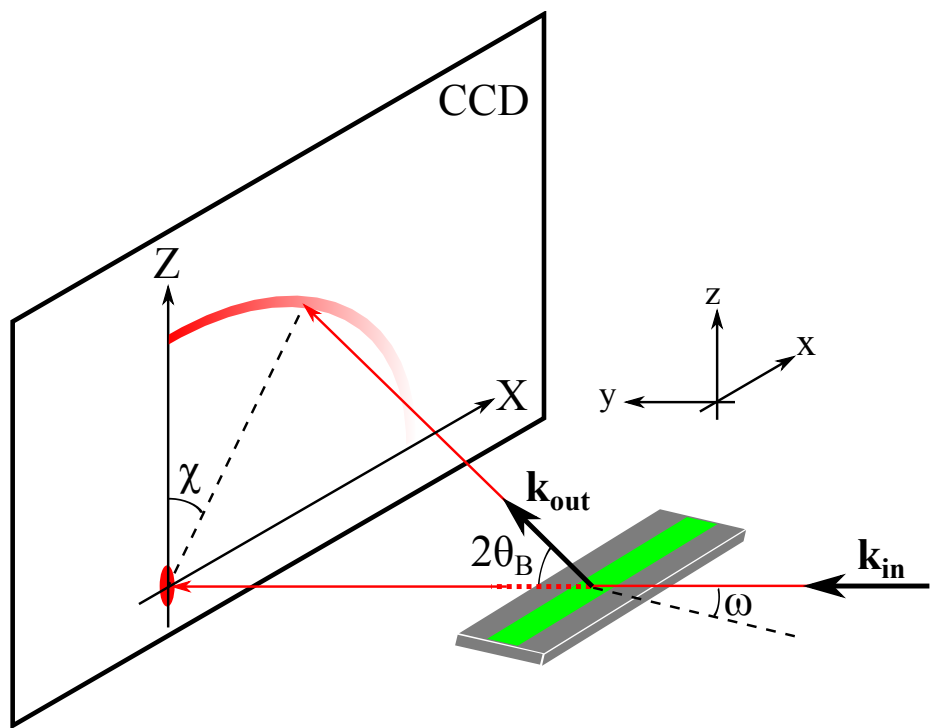


Figure A.3: Notations used in this section. The arc originating from the Z -axis is the mosaic arc due to the mosaic spread distribution.

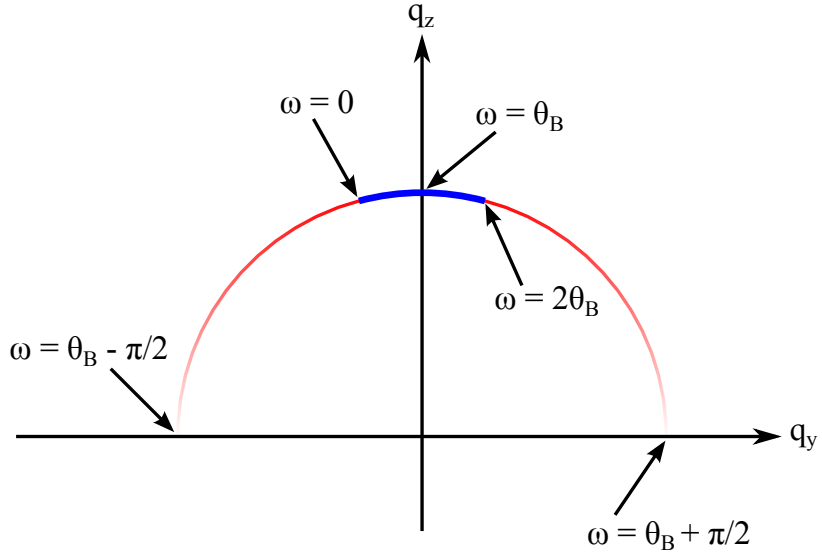


Figure A.4: Rocking scan trace in q -space.

Eq. (3.14) expressed in terms of the coordinates defined in Fig. A.3 is

$$\begin{aligned} q_x &= q \cos \theta \sin \chi \\ q_y &= q (-\sin \theta \cos \omega + \cos \theta \cos \chi \sin \omega) \\ q_z &= q (\sin \theta \sin \omega + \cos \theta \cos \chi \cos \omega). \end{aligned} \quad (\text{A.18})$$

For a rocking scan focused on a particular order, $\chi = 0$ and $\theta = \theta_B$ while ω is varied about θ_B , where θ_B is the Bragg angle. Then,

$$\begin{aligned} q_x &= 0 \\ q_y &= q_B \sin(\omega - \theta_B) \\ q_z &= q_B \cos(\omega - \theta_B), \end{aligned} \quad (\text{A.19})$$

which shows that this scan traces a part of the circular path in the $q_x = 0$ plane as shown in Fig. A.4. As Fig. A.4 shows, however, the rocking scan only probes a small fraction of the entire distribution, limited by $2\theta_B$. As discussed in section 3.3.3, beyond $\omega = 2\theta_B$, the substrate blocks scattering. On the other hand, the ring analysis takes advantage of a two dimensional detector and can probe a substantially wider range of the distribution in principle: approximately $\pm 45^\circ$ at $\omega = \theta_B$. This method is now described.

In the ring method, we set $\omega = \theta_B$ and scan on the detector along $\theta = \theta_B$ as a function of χ . Then, Eq. (A.18) becomes

$$\begin{aligned} q_x &= q \cos \theta_B \sin \chi \\ q_y &= q \sin \theta_B \cos \theta_B (\cos \chi - 1) \\ q_z &= q(\sin^2 \theta_B + \cos^2 \theta_B \cos \chi), \end{aligned} \quad (\text{A.20})$$

where $q = 4\pi \sin \theta_B / \lambda$. For small θ_B , Eq. (A.20) reduces to

$$\begin{aligned} q_x &\approx q \sin \chi \\ q_y &\approx 0 \\ q_z &\approx q \cos \chi. \end{aligned} \quad (\text{A.21})$$

For a sharp Bragg peak, this ring method gives the same mosaic intensity $I(\chi, \theta_B)$ in Eq. (A.21) as the rocking method mosaic intensity $I(\omega - \theta_B)$ in Eq. (A.19) because the mosaic distribution $P(\alpha)$ is in-plane isotropic. Differences occur when diffuse scattering is added. The diffuse scattering intensity is much broader and weaker than the Bragg peaks. In the ring method, it can be estimated as the average from two rings offset on either side from θ_B and subtracted from the θ_B ring.

A.1.3 NFIT

The original NFIT program was written by Dr. Yufeng Liu and described in his thesis. It was used in the Nagle lab, with small updates for data handling, from 2003 until recently. A newer version has been implemented by Michael Jablin that calculates the theoretical structure factor using cylindrical domains appropriate for in-plane correlations [48] rather than rectangular domains appropriate for coherence domains. All these versions approximated the effect of mosaic spread roughly by averaging only in the q_r direction at fixed q_z which means that mosaic rings are approximated as mosaic lines or spikes. The subsequent development described here and not yet adopted by the Nagle lab calculates the structure factor $S(q_r, q_z)$ with rotational symmetry about the z -axis, which eliminates the ϕ' dependence in Eq. (A.15). The program interpolates $S(q_r, q_z)$ in terms of the spherical coordinates q and θ with $\phi = 0$ to perform the double integration in Eq. (A.15). After the mosaic spread

integration, the program performs the q_y integration described in section 2.2.5. For this integration, the calculated S_M is interpolated in terms of q_x , q_y , and q_z .

Note: if the structure factor defined in the Cartesian coordinates is desired (for a case of square domains instead of circular ones), Eq. (A.10 – A.12) can be used instead of Eq. (A.13) and (A.14).

While it is an improvement, the new program also is an approximation because it does not include the unknown form factor $|F(q_z)|$. The mosaic spread integration mixes up intensity at different q_z values, so the separation of $|F(q_z)|$ from $S(\mathbf{q})$ is in principle impossible. One way to deal with this issue would be to combine the SDP program, which determines $|F(q_z)|$, with the NFIT program, but that will end up with too many non-linear parameters. Another possibility is to limit the fitting range to regions close to the meridian. For a small range of integration, it is not unreasonable to assume that the form factor is approximately constant as can be seen from Eq. (A.12) with small q_x , q_y , and α . Therefore, the analysis developed in this appendix ignores the form factor.

Model $F(h, k)$								Data	error	
h	k	Fit1	Fit2	Fit3	Fit4	Fit5	Fit6	Fit7	$ F(h, k) $	σ_F
1	-1	-74.0	-71.6	-39.4	-78.4	-77.1	-79.1	-79.8	86.3	3.7
1	0	-94.3	-89.2	-63.1	-98.6	-100.0	-99.6	-100.1	100.0	0.5
1	1	23.7	19.9	19.9	23.9	25.2	24.1	24.2	43.1	2.6
1	2	-6.0	-2.3	-8.3	-6.0	-6.9	-5.9	-6.0	0.0	3.9
1	3	0.3	-3.7	6.9	1.4	2.0	1.5	1.4	8.8	0.2
2	-2	-17.2	-20.2	-28.5	-19.7	-20.4	-20.1	-20.1	18.0	0.6
2	-1	-62.2	-59.1	-53.9	-67.9	-66.5	-65.7	-66.9	76.0	0.4
2	0	-32.1	-31.9	-30.8	-33.2	-33.0	-33.0	-33.1	28.7	0.2
2	1	31.8	30.2	32.3	31.5	31.5	32.1	32.0	39.5	0.4
2	2	-25.0	-24.2	-22.9	-24.0	-23.9	-24.3	-24.3	24.6	0.3
2	3	15.0	15.0	14.8	14.9	14.9	14.9	14.9	14.6	0.1
2	4	-6.1	-5.2	-12.0	-8.6	-8.9	-8.6	-8.5	9.2	0.2
2	5	1.1	-2.4	10.2	6.6	7.0	6.8	6.6	5.6	0.7
2	6	0.1	5.5	-4.0	-7.2	-7.1	-7.0	-7.0	4.1	0.3
3	-2	34.2	33.3	29.9	40.3	40.6	39.9	40.1	33.2	0.8
3	-1	39.4	39.1	27.6	45.5	44.9	44.0	44.4	45.9	0.4
3	0	-3.2	-4.3	-2.3	-4.3	-4.0	-4.1	-4.2	13.2	0.5
3	1	-9.4	-6.9	-11.2	-9.2	-9.6	-9.8	-9.5	0.0	7.1
3	2	14.1	12.4	15.0	14.0	14.3	14.5	14.3	10.2	0.2
3	3	-12.9	-13.7	-12.5	-13.1	-13.1	-13.2	-13.1	13.6	0.2
3	4	8.6	11.7	9.0	9.5	9.4	9.2	9.3	13.0	0.2
3	5	-4.1	-7.9	-7.1	-6.0	-5.9	-5.6	-5.7	9.6	0.1
3	6	1.1	3.6	5.4	3.9	3.9	3.6	3.7	5.6	0.4
4	-3	-18.1	-18.9	-18.0	-20.4	-21.7	-22.6	-21.6	23.0	0.6
4	-2	-48.5	-45.2	-23.9	-53.5	-53.2	-53.5	-53.0	42.8	0.5
4	-1	-17.8	-19.9	-7.8	-19.4	-19.0	-18.7	-18.7	22.6	0.9
4	0	11.3	14.3	7.8	12.7	12.6	12.7	12.6	16.2	0.1
4	1	-2.8	-7.8	-1.0	-4.1	-3.7	-3.7	-3.8	7.2	0.6
4	2	-4.0	1.6	-5.4	-2.9	-3.3	-3.5	-3.3	9.9	0.3
4	3	7.1	3.2	7.8	6.3	6.5	6.7	6.5	0.0	2.1
4	4	-6.5	-5.7	-6.8	-6.4	-6.3	-6.4	-6.4	3.0	0.3
4	5	4.2	6.1	5.0	4.7	4.4	4.3	4.4	4.1	0.2
4	6	-1.8	-4.9	-3.8	-2.8	-2.5	-2.3	-2.5	2.5	1.1

Table A.1: Form factors for $h = 1$ to 4

A.2 More results from LAXS models

h	k	Model $F(h, k)$							Data $ F(h, k) $	σ_F
		Fit1	Fit2	Fit3	Fit4	Fit5	Fit6	Fit7		
5	-3	-18.2	-17.8	-26.6	-16.2	-16.4	-17.7	-17.3	15.6	0.6
5	-2	-21.1	-21.4	-19.3	-19.3	-19.3	-19.6	-19.4	16.3	0.2
5	-1	1.8	1.9	4.4	2.0	2.0	2.2	2.2	7.5	0.2
5	0	4.7	4.8	6.4	4.3	4.6	4.5	4.3	6.5	0.1
5	1	-6.1	-8.3	-8.2	-6.1	-6.4	-6.3	-6.1	6.4	0.2
6	-4	-1.9	-1.8	6.9	2.2	2.2	-3.0	-2.8	5.9	0.2
6	-3	-4.3	-4.0	7.8	6.6	6.7	-5.9	-5.9	5.9	0.2
6	-2	-1.4	-1.7	1.5	2.7	2.8	-1.7	-1.8	3.8	0.3
6	-1	0.8	1.1	-2.7	-2.0	-2.2	1.1	1.1	3.4	0.3
6	0	-0.2	-0.5	0.8	0.7	0.7	-0.3	-0.3	3.4	0.1
6	1	-0.2	0.1	1.5	0.6	0.8	-0.2	-0.2	3.9	0.1
6	2	0.3	0.3	-2.0	-1.2	-1.5	0.3	0.3	0.0	0.9
6	3	-0.2	-0.5	0.5	1.0	1.2	-0.2	-0.2	3.5	0.1
6	4	-0.1	0.6	1.5	-0.2	-0.1	0.0	0.0	3.4	0.1
7	-4	-12.8	-12.0	-13.9	-9.8	-9.7	-9.6	-9.6	10.0	0.1
7	-3	-12.8	-13.0	-7.5	-9.6	-9.6	-9.2	-9.4	8.1	0.2
7	-2	1.1	0.9	3.0	0.9	1.0	1.1	1.1	4.2	0.9
7	-1	2.2	2.5	1.8	1.5	1.7	1.7	1.7	3.6	0.2
7	0	-2.4	-3.8	-3.1	-1.8	-2.1	-2.2	-2.2	2.8	0.1
8	0	-0.8	0.1	-1.0	-0.4	0.1	-0.4	-0.4	0.0	0.9
9	-5	-5.6	-5.2	2.5	-0.7	-7.3	-8.7	-8.0	6.1	0.5
9	-4	-5.5	-5.6	1.1	-0.6	-6.6	-8.0	-7.4	5.6	0.5
9	-3	0.5	0.3	-0.7	0.1	0.7	1.1	1.0	0.0	3.3
9	-2	0.9	1.2	-0.2	0.1	1.0	1.4	1.2	3.0	0.4
9	-1	-1.0	-1.7	0.7	-0.1	-1.3	-1.9	-1.7	0.0	1.7
9	0	0.4	1.7	-0.4	0.1	0.6	1.0	0.9	2.2	0.6

Table A.2: Form factors for $h = 5$ to 9

A.3 Derivation of the contour part of the form factor

In this section, we derive F_C . The ripple profile, $u(x)$ is given by

$$u(x) = \begin{cases} -\frac{A}{\lambda_r - x_0} \left(x + \frac{\lambda_r}{2} \right) & \text{for } -\frac{\lambda_r}{2} \leq x < -\frac{x_0}{2} \\ \frac{A}{x_0} x & \text{for } -\frac{x_0}{2} \leq x \leq \frac{x_0}{2} \\ -\frac{A}{\lambda_r - x_0} \left(x - \frac{\lambda_r}{2} \right) & \text{for } \frac{x_0}{2} < x \leq \frac{\lambda_r}{2} \end{cases} \quad (\text{A.22})$$

The contour part of the form factor is the Fourier transform of the contour function, $C(x, z)$,

$$F_C(\mathbf{q}) = \frac{1}{\lambda_r} \int_{-\frac{\lambda_r}{2}}^{\frac{\lambda_r}{2}} dx \int_{-\frac{D}{2}}^{\frac{D}{2}} dz C(x, z) e^{iq_z z} e^{iq_x x}$$

As discussed in section X, the modulated models allow the electron density to modulate along the ripple direction, x . This means

$$C(x, z) = \begin{cases} f_1 \delta[z - u(x)] & \text{for } -\frac{\lambda_r}{2} \leq x < -\frac{x_0}{2} \\ \delta[z - u(x)] & \text{for } -\frac{x_0}{2} < x < \frac{x_0}{2} \\ f_1 \delta[z - u(x)] & \text{for } \frac{x_0}{2} \leq x < \frac{\lambda_r}{2} \\ + f_2 \delta\left(x + \frac{x_0}{2}\right) \delta\left(z + \frac{A}{2}\right) + f_2 \delta\left(x - \frac{x_0}{2}\right) \delta\left(z - \frac{A}{2}\right). \end{cases} \quad (\text{A.23})$$

The contribution from the minor arm is

$$\begin{aligned} & \frac{1}{\lambda_r} \int_{-\frac{\lambda_r}{2}}^{-\frac{x_0}{2}} dx e^{iq_x x} e^{iq_z u(x)} + \int_{\frac{x_0}{2}}^{\frac{\lambda_r}{2}} dx e^{iq_x x} e^{iq_z u(x)} \\ &= \frac{1}{\lambda_r} \int_{\frac{x_0}{2}}^{\frac{\lambda_r}{2}} dx e^{-i[q_x x - q_z \frac{A}{\lambda_r - x_0} (x - \frac{\lambda_r}{2})]} + \int_{\frac{x_0}{2}}^{\frac{\lambda_r}{2}} dx e^{i[q_x x - q_z \frac{A}{\lambda_r - x_0} (x - \frac{\lambda_r}{2})]} \\ &= \frac{2}{\lambda_r} \int_{\frac{x_0}{2}}^{\frac{\lambda_r}{2}} \cos \left[\left(q_x - q_z \frac{A}{\lambda_r - x_0} \right) x + q_z \frac{A}{\lambda_r - x_0} \frac{\lambda_r}{2} \right] \end{aligned} \quad (\text{A.24})$$

Using a trigonometric identity,

$$\sin u - \sin v = 2 \cos[(u + v)/2] \sin[(u - v)/2],$$

and defining

$$\omega(\mathbf{q}) = \frac{1}{2} (q_x x_0 + q_z A), \quad (\text{A.25})$$

we further simplify Eq. (A.24),

$$\begin{aligned} &= \frac{2}{\lambda_r} \frac{\lambda_r - x_0}{\frac{1}{2} q_x \lambda_r - \omega} \cos \left[\frac{1}{2} \left(\frac{1}{2} q_x \lambda_r + \omega \right) \right] \sin \left[\frac{1}{2} \left(\frac{1}{2} q_x \lambda_r - \omega \right) \right] \\ &= \frac{1}{\lambda_r} \frac{\lambda_r - x_0}{\frac{1}{2} q_x \lambda_r - \omega} \cos \left[\frac{1}{2} \left(\frac{1}{2} q_x \lambda_r + \omega \right) \right] \frac{\sin \left(\frac{1}{2} q_x \lambda_r - \omega \right)}{\cos \left[\frac{1}{2} \left(\frac{1}{2} q_x \lambda_r - \omega \right) \right]} \\ &= \frac{\lambda_r - x_0}{\lambda_r} \frac{\cos \left[\frac{1}{2} \left(\frac{1}{2} q_x \lambda_r + \omega \right) \right]}{\cos \left[\frac{1}{2} \left(\frac{1}{2} q_x \lambda_r - \omega \right) \right]} \frac{\sin \left(\frac{1}{2} q_x \lambda_r - \omega \right)}{\frac{1}{2} q_x \lambda_r - \omega}. \end{aligned} \quad (\text{A.26})$$

Similarly, we calculate the contribution from the major arm,

$$\begin{aligned} \frac{1}{\lambda_r} \int_{-\frac{x_0}{2}}^{\frac{x_0}{2}} dx e^{i \left(\frac{q_z A}{x_0} + q_x \right) x} &= \frac{2}{\lambda_r} \int_0^{\frac{x_0}{2}} dx \cos \left(\frac{q_z A}{x_0} + q_x \right) x \\ &= \frac{x_0 \sin \omega}{\lambda_r \omega} \end{aligned} \quad (\text{A.27})$$

The contribution from the kink region is

$$\begin{aligned} &\frac{1}{\lambda_r} \iint dx dz \left[\delta \left(x + \frac{x_0}{2} \right) \delta \left(z + \frac{A}{2} \right) + \delta \left(x - \frac{x_0}{2} \right) \delta \left(z - \frac{A}{2} \right) \right] e^{iq_x x} e^{iq_z z} \\ &= \frac{2}{\lambda_r} \cos \omega. \end{aligned} \quad (\text{A.28})$$

Therefore,

$$\begin{aligned} F_C(\mathbf{q}) &= \frac{x_0 \sin \omega}{\lambda_r \omega} + f_1 \frac{\lambda_r - x_0}{\lambda_r} \frac{\cos \left[\frac{1}{2} \left(\frac{1}{2} q_x \lambda_r + \omega \right) \right]}{\cos \left[\frac{1}{2} \left(\frac{1}{2} q_x \lambda_r - \omega \right) \right]} \frac{\sin \left(\frac{1}{2} q_x \lambda_r - \omega \right)}{\frac{1}{2} q_x \lambda_r - \omega} \\ &\quad + \frac{2f_2}{\lambda_r} \cos \omega \end{aligned} \quad (\text{A.29})$$

some additional models. We write the form factor as

$$F(\mathbf{q}) = F_C^M(\mathbf{q}) F_T^M(\mathbf{q}) + f_1 F_C^m(\mathbf{q}) F_T^m(\mathbf{q}) + f_2 F_C^k(\mathbf{q}) F_T^k(\mathbf{q}) \quad (\text{A.30})$$

such that

$$F_C^M = \frac{x_0}{\lambda_r} \frac{\sin \omega}{\omega} \quad (\text{A.31})$$

$$F_C^m = \frac{\lambda_r - x_0}{\lambda_r} \frac{\cos \left[\frac{1}{2} \left(\frac{1}{2} q_x \lambda_r + \omega \right) \right]}{\cos \left[\frac{1}{2} \left(\frac{1}{2} q_x \lambda_r - \omega \right) \right]} \frac{\sin \left(\frac{1}{2} q_x \lambda_r - \omega \right)}{\frac{1}{2} q_x \lambda_r - \omega} \quad (\text{A.32})$$

$$F_C^k = \frac{2}{\lambda_r} \cos \omega. \quad (\text{A.33})$$

A.4 Rotation of a Two-Dimensional Function

Let us consider rotating a function, $f(x, z)$ in two dimensions by an angle, ψ , in the counterclockwise direction (see Fig. X). This is easily achieved by rotating the coordinate system by ψ in the clockwise direction. Let rotated coordinates be x' and z' . A point in the original coordinates, (x, z) , is written as (x', z') in the new coordinates. More specifically, the point P is written as $\mathbf{P} = x\hat{\mathbf{x}} + z\hat{\mathbf{z}} = x'\hat{\mathbf{x}}' + z'\hat{\mathbf{z}}'$. $\hat{\mathbf{x}}$ and $\hat{\mathbf{z}}$ in the $x'z'$ coordinate system are written as

$$\hat{\mathbf{x}} = \cos \psi \hat{\mathbf{x}}' + \sin \psi \hat{\mathbf{z}}' \quad (\text{A.34})$$

$$\hat{\mathbf{z}} = -\sin \psi \hat{\mathbf{x}}' + \cos \psi \hat{\mathbf{z}}'. \quad (\text{A.35})$$

Pluggin these in $\mathbf{P} = x\hat{\mathbf{x}} + z\hat{\mathbf{z}}$ leads to

$$x' = x \cos \psi - z \sin \psi \quad (\text{A.36})$$

$$z' = z \cos \psi + x \sin \psi, \quad (\text{A.37})$$

the inverse of which is

$$x = x' \cos \psi + z' \sin \psi \quad (\text{A.38})$$

$$z = -x' \sin \psi + z' \cos \psi. \quad (\text{A.39})$$

Using the latter equations, $f(x, z)$ can be expressed in terms of x' and z' . The resulting function $f(x', z')$ is the rotated version of $f(x, z)$.

As an example, let us consider a Dirac delta function located at $(x, z) = (0, Z_{\text{H}})$, that is, $f(x, z) = \delta(x)\delta(z - Z_{\text{H}})$. After the rotation by ψ , it becomes

$$\begin{aligned} f(x, z) &\rightarrow \delta(x \cos \psi + z \sin \psi)\delta(-x \sin \psi + z \cos \psi - Z_{\text{H}}) \\ &= \frac{\delta(x + z \tan \psi)}{|\cos \psi|} \frac{\delta(-x \sin \psi \cos \psi + z \cos^2 \psi - Z_{\text{H}} \cos \psi)}{1/|\cos \psi|} \\ &= \delta(x + z \tan \psi)\delta(z \tan \psi \sin \psi \cos \psi + z \cos^2 \psi - Z_{\text{H}} \cos \psi) \\ &= \delta(x + z \tan \psi)\delta(z - Z_{\text{H}} \cos \psi), \end{aligned}$$

which is a part of the expression for $T_{\psi}(x, z)$ in the simple delta function model.

A.5 Derivation of the transbilayer part of the form factor in the 2G hybrid model

In this section, we derive the trasbilayer part of the form factor calculated from the 2G hybrid model discussed in section X. Defining $z' = -x \sin \psi + z \cos \psi$, the Fourier transform of a Gaussian function along the line tilted from z -axis by ψ is

$$\begin{aligned} & \iint dz dx \rho_{\text{Hi}} \exp \left\{ -\frac{(z' - Z_{\text{Hi}})^2}{2\sigma_{\text{Hi}}^2} \right\} \delta(x \cos \psi + z \sin \psi) e^{iq_x x} e^{iq_z z} \\ &= \frac{1}{\cos \psi} \int_{-\frac{D}{2}}^{\frac{D}{2}} dz \rho_{\text{Hi}} \exp \left\{ -\frac{(z - Z_{\text{Hi}} \cos \psi)^2}{2\sigma_{\text{Hi}}^2 \cos^2 \psi} + i(q_z - q_x \tan \psi)z \right\} \\ & \approx \rho_{\text{Hi}} \sqrt{2\pi} \sigma_{\text{Hi}} \exp \left\{ i\alpha Z_{\text{Hi}} - \frac{1}{2} \alpha^2 \sigma_{\text{Hi}}^2 \right\} \end{aligned} \quad (\text{A.40})$$

with $\alpha = q_z \cos \psi - q_x \sin \psi$. Using Eq. (A.40) and adding the other side of the bilayer and the terminal methyl term, we get

$$F_{\text{G}} = \sqrt{2\pi} \left[-\rho_{\text{M}} \sigma_{\text{M}} \exp \left\{ -\frac{1}{2} \alpha^2 \sigma_{\text{M}}^2 \right\} + \sum_{i=1}^{\text{1 or 2}} 2\rho_{\text{Hi}} \sigma_{\text{Hi}} \cos(\alpha Z_{\text{Hi}}) \exp \left\{ -\frac{1}{2} \alpha^2 \sigma_{\text{Hi}}^2 \right\} \right]. \quad (\text{A.41})$$

The strip part of the model in the minus fluid convention is

$$\rho_{\text{S}}(z) = \begin{cases} -\Delta\rho & \text{for } 0 \leq z < Z_{\text{CH}_2} \cos \psi, \\ 0 & \text{for } Z_{\text{W}} \cos \psi \leq z \leq D/2, \end{cases} \quad (\text{A.42})$$

where $\Delta\rho = \rho_{\text{W}} - \rho_{\text{CH}_2}$. Then, the corresponding Fourier transform is

$$\begin{aligned} F_{\text{S}} &= \iint dz dx e^{iq_x x} e^{iq_z z} \rho_{\text{S}}(z) \delta(x \cos \psi + z \sin \psi) \\ &= \frac{2}{\cos \psi} \int_0^{Z_{\text{CH}_2} \cos \psi} dz \cos \left(\frac{\alpha}{\cos \psi} z \right) (-\Delta\rho) \\ &= -2\Delta\rho \frac{\sin(\alpha Z_{\text{CH}_2})}{\alpha}. \end{aligned} \quad (\text{A.43})$$

The bridging part of the model in the minus fluid convention is

$$\rho_B(x, z) = \frac{\Delta\rho}{2} \cos\left[\frac{-\pi}{\Delta Z_H}(z' - Z_W)\right] - \frac{\Delta\rho}{2} \quad (\text{A.44})$$

for $Z_{CH_2} \cos \psi < z < Z_W \cos \psi$, and 0 otherwise. Here, $\Delta Z_H = Z_W - Z_{CH_2}$. Then, for the strip part of the form factor, we have

$$\begin{aligned} F_B &= \iint dz dx e^{iq_x x} e^{iq_z z} \delta(x \cos \psi + z \sin \psi) \rho_B(x, z) \\ &= \frac{\Delta\rho}{\cos \psi} \int_{Z_{CH_2} \cos \psi}^{Z_W \cos \psi} dz \cos\left(\alpha \frac{z}{\cos \psi}\right) \left\{ \cos\left[-\frac{\pi}{\Delta Z_H} \left(\frac{z}{\cos \psi} - Z_W\right)\right] - 1 \right\} \\ &= \Delta\rho \left\{ \frac{\Delta Z_H \sin\left[\frac{\pi(-u+Z_W)}{\Delta Z_H} + \alpha u\right]}{-2\pi + 2\alpha\Delta Z_H} + \frac{\Delta Z_H \sin\left[\frac{\pi(u-Z_W)}{\Delta Z_H} + \alpha u\right]}{2\pi + 2\alpha\Delta Z_H} - \frac{\sin(\alpha u)}{\alpha} \right\} \Big|_{Z_{CH_2}}^{Z_W} \\ &= -\frac{\Delta\rho}{\alpha} [\sin(\alpha Z_W) - \sin(\alpha Z_{CH_2})] \\ &\quad + \frac{\Delta\rho}{2} \left(\frac{1}{\alpha + \frac{\pi}{\Delta Z_H}} + \frac{1}{\alpha - \frac{\pi}{\Delta Z_H}} \right) [\sin(\alpha Z_W) + \sin(\alpha Z_{CH_2})]. \end{aligned} \quad (\text{A.45})$$

Because our X-ray scattering intensity was measured in a relative scale, an overall scaling factor was necessary for a non linear least square fitting procedure. This means that $\Delta\rho$ can be absorbed in the scaling factor. Doing so means that the values of ρ_{Hi} and ρ_M resulting from a fitting procedure are relative to $\Delta\rho$. One way to have these parameters in the absolute scale is to integrate the bilayer electron density over the lipid volume and equate the result to the total number of electrons in the lipid, which can easily be calculated from the chemical formula. For the ripple phase study in this thesis, the absolute values of the electron density were not of importance, so the discussion was omitted in the main text.

A.6 Correction due to refractive index

q_z needs to be corrected for index of refraction [50].

Let θ' and λ' be the true scattering angle and wavelength within the sample. The wavelength by an energy analyzer, λ , and the scattering angle calculated from a position on a CCD detector, θ are apparent. The correction is not necessary in the horizontal direction. The Snell's law in Fig. X gives

$$n \cos \theta = n' \cos \theta' \quad (\text{A.46})$$

$$n\lambda = n'\lambda'. \quad (\text{A.47})$$

For low angle X-ray scattering, the momentum transfer along z direction is

$$q_z = \frac{4\pi \sin \theta'}{\lambda'} \quad (\text{A.48})$$

$$= \frac{4\pi n'}{n\lambda} \sin \theta' \quad (\text{A.49})$$

$$= \frac{4\pi n'}{n\lambda} \sqrt{1 - \cos^2 \theta'} \quad (\text{A.50})$$

$$= \frac{4\pi n'}{n\lambda} \sqrt{1 - \left(\frac{n}{n'} \cos \theta\right)^2}. \quad (\text{A.51})$$

The apparent scattering angle, θ , is directly related to the vertical pixel position, p_z , by

$$\theta = \frac{1}{2} \tan^{-1} \left(\frac{p_z}{S} \right), \quad (\text{A.52})$$

where S is the sample-to-detector distance. The typical units of S and p_z are in mm. In our experimental setup, $n = 1$ and $n' = 0.9999978$ for lipids at $\lambda = 1.18 \text{ \AA}$. $S = 359.7 \text{ mm}$.

A.7 Thin Rod Model of the ripple phase

The thin rod model will be applied to the ripple phase WAXS. In this model, electron density of lipid chains are described as delta functions and lipid head groups are assumed not to contribute to scattering. Since the molecular packing of the major side of ripple phase is hypothesized to be gel-like, the model may be adequate. First, we will study diffraction from chains packed in gel phase manner whose system size is infinite but whose packing plane make an angle ξ with the xy plane. This infinite case is adequate for indexing the ripple Bragg peaks while it ignores the peak broadening effect. The system will later be truncated along the ripple direction to see the effect of the finite size on peak broadening. Finally, in-plane powder will be taken into account to derive a peak intensity pattern.

First, let us calculate the positions of the diffraction peaks from a two dimensional orthorhombic lattice whose plane makes an angle ξ with respect to the xy plane and extends to infinity. As a unit cell, we will take a parallelepipedon containing two rods, one located at the origin and the other located at the center (Fig. A.5). The lattice vectors are $\mathbf{a}_1 = a_1 \cos \xi \hat{\mathbf{x}} + a_1 \sin \xi \hat{\mathbf{z}}$ and $\mathbf{a}_2 = a_2 \hat{\mathbf{y}}$. There are other choices for how the lattice is oriented with respect to the ripple direction, which should be considered as well. Then, the Laue conditions are given by

$$2\pi h = \mathbf{q} \cdot \mathbf{a}_1 = (a_1 \cos \xi) q_x + (a_1 \sin \xi) q_z \quad (\text{A.53})$$

$$2\pi k = \mathbf{q} \cdot \mathbf{a}_2 = a_2 q_y, \quad (\text{A.54})$$

with h and k being zero or integer. Let us define the chain tilt angle θ to be the angle between the stacking z direction and the chain direction. We also define ϕ to represent the direction into which chains are tilted. In other words, θ and ϕ are usual spherical coordinates with respect to the ripple x , y , and z axes, not the local bilayer Cartesian axes. With this choice of coordinates, chains are tilted with respect to the local bilayer normal if $\theta = 0$. $\theta = \xi$ and $\phi = \pi$ gives chains parallel to the local bilayer normal, or $\theta_t = 0$. It would be good to work out the relation between θ and θ_t , θ_t being the chain tilt with respect to the local bilayer normal.

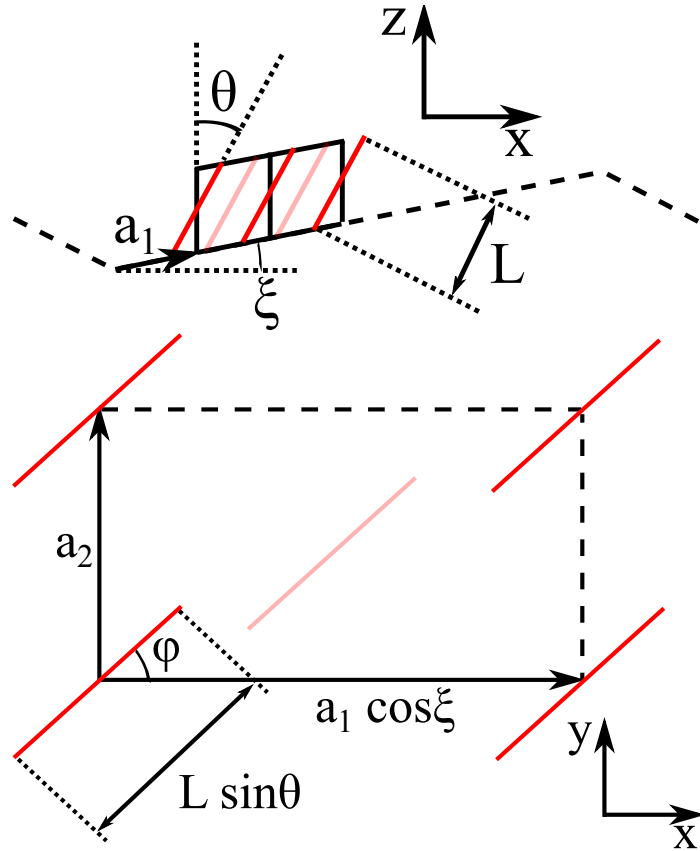


Figure A.5: Unit cell for chain packing in the major arm. (top) Projection of the unit cell in the xz -plane. The unit cell is taken as a parallelepipedon shown by black solid lines, each unit cell containing two chains. Chains located at the center of the unit cell are drawn as opaque red lines while chains at the lattice points are drawn as solid red lines. The dash line indicates the mid-plane of a rippling bilayer. Chains are tilted with respect to the stacking z direction by θ and the major arm is tilted with respect to the ripple x direction by ξ . The chain length is denoted by L . \mathbf{a}_1 and \mathbf{a}_2 are orthorhombic unit cell vectors. (bottom) Projection of the unit cell in the xy -plane. $\phi = 0$ means chains are tilted in the xz plane and $\phi = \pi/2$ means chains are titled into the direction perpendicular to the ripple direction.

The electron density, assuming a delta function for each chain, is given by

$$\rho(\mathbf{r}) = \delta(x - \alpha z, y - \beta z) + \quad (\text{A.55})$$

$$\delta \left[x - \frac{a_1 \cos \xi}{2} - \alpha \left(z - \frac{a_1 \sin \xi}{2} \right), y - \frac{a_2}{2} - \beta \left(z - \frac{a_1 \sin \xi}{2} \right) \right], \quad (\text{A.56})$$

where $\alpha = \tan \theta \cos \phi$ and $\beta = \tan \theta \sin \phi$. The first rod extends for

$$-L/2 \sin \theta \cos \phi \leq x \leq L/2 \sin \theta \cos \phi \quad (\text{A.57})$$

$$-L/2 \sin \theta \sin \phi \leq y \leq L/2 \sin \theta \sin \phi \quad (\text{A.58})$$

$$-L/2 \cos \theta \leq z \leq L/2 \cos \theta, \quad (\text{A.59})$$

and the second rod for

$$-L/2 \sin \theta \cos \phi + a_1/2 \cos \xi \leq x \leq L/2 \sin \theta \cos \phi + a_1/2 \cos \xi \quad (\text{A.60})$$

$$-L/2 \sin \theta \sin \phi + a_2/2 \leq y \leq L/2 \sin \theta \sin \phi + a_2/2 \quad (\text{A.61})$$

$$-L/2 \cos \theta + a_1/2 \sin \xi \leq z \leq L/2 \cos \theta + a_1/2 \sin \xi. \quad (\text{A.62})$$

Then, the form factor is given by

$$F(\mathbf{q}) = \int dx \int dy \int dz \rho(\mathbf{r}) e^{i\mathbf{q} \cdot \mathbf{r}} \quad (\text{A.63})$$

$$\begin{aligned} &= \int_{-\frac{L}{2} \cos \theta}^{\frac{L}{2} \sin \theta} dz e^{i(\alpha q_x + \beta q_y + q_z)z} + \\ &\int_{-\frac{L}{2} \cos \theta + \frac{a_1}{2} \sin \xi}^{\frac{L}{2} \cos \theta + \frac{a_1}{2} \sin \xi} dz e^{\frac{i}{2}[q_x(a_1 \cos \xi - \alpha a_1 \sin \xi) + q_y(a_2 - \beta a_1 \sin \xi)]} e^{i(\alpha q_x + \beta q_y + q_z)z} \\ &= \left[1 + e^{\frac{i}{2}(a_1 \cos \xi q_x + a_1 \sin \xi q_z + a_2 q_y)} \right] \frac{2}{\gamma} \sin \left(\frac{\gamma L \cos \theta}{2} \right) \\ &= [1 + e^{i\pi(h+k)}] \frac{2}{\gamma} \sin \left(\frac{\gamma L \cos \theta}{2} \right), \end{aligned} \quad (\text{A.64})$$

where $\gamma = \alpha q_x + \beta q_y + q_z$. Eq. A.64 shows that peaks with $h+k$ being odd is extinct. For $h+k$ even, we have

$$F(\mathbf{q}) = \frac{4}{\gamma} \sin \left(\frac{\gamma L \cos \theta}{2} \right). \quad (\text{A.65})$$

For (20) peak, $q_y = 0$ and $4\pi = a_1 \cos \xi q_x + a_1 \sin \xi q_z$. The second equation can be rewritten to give

$$q_z = -\frac{1}{\tan \xi} q_x + \frac{4\pi}{a_1 \sin \xi} \quad (\text{A.66})$$

which defines a straight line in $q_x q_z$ -plane along which (20) Bragg rod appears. Eq. A.65 has a peak at $\gamma = 0$. Hence, the maximum intensity of (20) peak is at q_x and q_z that satisfy Laue conditions and $\gamma = 0$. This gives three equations and three unknowns. Explicitly written, we have

$$q_y = 0 \quad (\text{A.67})$$

$$4\pi = a_1 \cos \xi q_x + a_1 \sin \xi q_z \quad (\text{A.68})$$

$$0 = \tan \theta \cos \phi q_x + q_z \quad (\text{A.69})$$

Solving these, we get

$$q_x = \frac{4\pi}{a_1 \cos \xi (1 - \tan \theta_t \cos \phi \tan \xi)} \quad (\text{A.70})$$

$$q_z = \frac{-4\pi \tan \theta_t \cos \phi}{a_1 \cos \xi (1 - \tan \theta_t \cos \phi \tan \xi)} \quad (\text{A.71})$$

For $\phi = \pi/2$, we have $q_x = 4\pi/(a_1 \cos \xi)$ and $q_z = 0$, so one would expect to see a peak on the equator, the case of which is similar to $L_{\beta I}$ phase in gel phase. To get back to ordinary gel phase, ξ should be set equal to zero.

For any (hk) line, we again have three equations and three unknowns as

$$2\pi h = q_x a_1 \cos \xi + q_z a_1 \sin \xi \quad (\text{A.72})$$

$$2\pi k = q_y a_2 \quad (\text{A.73})$$

$$0 = q_x \tan \theta_t \cos \phi + \frac{2\pi k}{a_2} \tan \theta_t \sin \phi + q_z \quad (\text{A.74})$$

Solving for q_x , q_y , and q_z , we obtain

$$q_x = \frac{2\pi(h + ka\beta \sin \xi)}{a_1 \cos \xi(1 - \alpha \tan \xi)} \quad (\text{A.75})$$

$$q_y = \frac{2\pi k}{a_2} \quad (\text{A.76})$$

$$q_z = \frac{-2\pi(h\alpha + ka\beta \cos \xi)}{a_1 \cos \xi(1 - \alpha \tan \xi)}, \quad (\text{A.77})$$

where $a = a_1/a_2$.

Bibliography

- [1] PF Fahey and WW Webb. Lateral diffusion in phospholipid bilayer membranes and multilamellar liquid crystals. *Biochemistry*, 17(15):3046–3053, 1978.
- [2] A. Tardieu, Vittorio Luzzati, and F.C. Reman. Structure and polymorphism of the hydrocarbon chains of lipids: A study of lecithin-water phases. *Journal of Molecular Biology*, 75(4):711 – 733, 1973.
- [3] Elizabeth J Luna and Harden M McConnell. The intermediate monoclinic phase of phosphatidylcholines. *Biochimica et Biophysica Acta (BBA)-Biomembranes*, 466(3):381–392, 1977.
- [4] Bruce R. Copeland and Harden M. McConnel. The rippled structure in bi-layer membranes of phosphatidylcholine and binary mixtures of phosphatidyl-choline and cholesterol. *Biochimica et Biophysica Acta (BBA) - Biomembranes*, 599(1):95 – 109, 1980.
- [5] D Ruppel and E Sackmann. On defects in different phases of two-dimensional lipid bilayers. *Journal de Physique*, 44(9):1025–1034, 1983.
- [6] JAN Zasadzinski and MB Schneider. Ripple wavelength, amplitude, and configuration in lyotropic liquid crystals as a function of effective headgroup size. *Journal de Physique*, 48(11):2001–2011, 1987.
- [7] JA Zasadzinski, J Schneir, J Gurley, V Elings, and PK Hansma. Scanning tunneling microscopy of freeze-fracture replicas of biomembranes. *Science*, 239(4843):1013–1015, 1988.
- [8] Daniel C. Wack and Watt W. Webb. Synchrotron x-ray study of the modulated lamellar phase $p\beta'$ in the lecithin-water system. *Phys. Rev. A*, 40:2712–2730, Sep 1989.

- [9] RJ Wittebort, CF Schmidt, and RG Griffin. Solid-state carbon-13 nuclear magnetic resonance of the lecithin gel to liquid-crystalline phase transition. *Biochemistry*, 20(14):4223–4228, 1981.
- [10] Marilyn B Schneider, WINSTON K Chan, and Watt W Webb. Fast diffusion along defects and corrugations in phospholipid p beta, liquid crystals. *Biophysical journal*, 43(2):157–165, 1983.
- [11] GS Smith, EB Sirota, CR Safinya, and Noel A Clark. Structure of the 1 β phases in a hydrated phosphatidylcholine multimembrane. *Physical review letters*, 60(9):813, 1988.
- [12] Rainer Fischer, Mariola Fotin-Mleczek, Hansjrg Hufnagel, and Roland Brock. Break on through to the other sidebiophysics and cell biology shed light on cell-penetrating peptides. *ChemBioChem*, 6(12):2126–2142, 2005.
- [13] Alain Joliot and Alain Prochiantz. Transduction peptides: from technology to physiology. *Nat Cell Biol*, 6(3), 2004.
- [14] Maria Lindgren, Mattias Hillbrink, Alain Prochiantz, and lo Langel. Cell-penetrating peptides. *Trends in Pharmacological Sciences*, 21(3):99 – 103, 2000.
- [15] Alan D. Frankel and Carl O. Pabo. Cellular uptake of the tat protein from human immunodeficiency virus. *Cell*, 55(6):1189 – 1193, 1988.
- [16] Maurice Green and Paul M. Loewenstein. Autonomous functional domains of chemically synthesized human immunodeficiency virus tat trans-activator protein. *Cell*, 55(6):1179 – 1188, 1988.
- [17] Eric Viks, Priscille Brodin, and Bernard Lebleu. Hiv-1 tat protein basic domain rapidly translocates through the plasma membrane and accumulates in the cell nucleus. *Journal of Biological Chemistry*, 272(25):16010–16017, 1997.
- [18] Gohar Ter-Avetisyan, Gisela Tnnemann, Danny Nowak, Matthias Nitschke, Andreas Herrmann, Marek Drab, and M. Cristina Cardoso. Cell entry of arginine-rich peptides is independent of endocytosis. *Journal of Biological Chemistry*, 284(6):3370–3378, 2009.

- [19] Gisela Tnnemann, Robert M. Martin, Simone Haupt, Christoph Patsch, Frank Edenhofer, and M. Cristina Cardoso. Cargo-dependent mode of uptake and bioavailability of tat-containing proteins and peptides in living cells. *The FASEB Journal*, 20(11):1775–1784, 2006.
- [20] Andr Ziegler, Pierluigi Nervi, Markus Drrenberger, and Joachim Seelig. The cationic cell-penetrating peptide cpptat derived from the hiv-1 protein tat is rapidly transported into living fibroblasts: optical, biophysical, and metabolic evidence. *Biochemistry*, 44(1):138–148, 2005. PMID: 15628854.
- [21] J. S. Wadia, R. V. Stan, and S. F. Dowdy. Transducible tat-ha fusogenic peptide enhances escape of tat-fusion proteins after lipid raft macropinocytosis. *Nature Medicine*, 10(3):310–315, 2004.
- [22] I. M. Kaplan, J. S. Wadia, and S. F. Dowdy. Cationic tat peptide transduction domain enters cells by macropinocytosis. *Journal of Controlled Release*, 102(1):247–253, 2005.
- [23] David A Mann and Alan D Frankel. Endocytosis and targeting of exogenous hiv-1 tat protein. *The EMBO journal*, 10(7):1733, 1991.
- [24] Jean Philippe Richard, Kamran Melikov, Hilary Brooks, Paul Prevot, Bernard Lebleu, and Leonid V Chernomordik. Cellular uptake of unconjugated tat peptide involves clathrin-dependent endocytosis and heparan sulfate receptors. *Journal of Biological Chemistry*, 280(15):15300–15306, 2005.
- [25] Simon W Jones, Richard Christison, Ken Bundell, Catherine J Voyce, Sarah Brockbank, Peter Newham, and Mark A Lindsay. Characterisation of cell-penetrating peptide-mediated peptide delivery. *British journal of pharmacology*, 145(8):1093–1102, 2005.
- [26] Agnès Vendeville, Fabienne Rayne, Anne Bonhoure, Nadir Bettache, Philippe Montcourrier, and Bruno Beaumelle. Hiv-1 tat enters t cells using coated pits before translocating from acidified endosomes and eliciting biological responses. *Molecular biology of the cell*, 15(5):2347–2360, 2004.
- [27] Christina Foerg, Urs Ziegler, Jimena Fernandez-Carneado, Ernest Giralt, Robert Rennert, Annette G Beck-Sickinger, and Hans P Merkle. Decoding the

- entry of two novel cell-penetrating peptides in hela cells: lipid raft-mediated endocytosis and endosomal escape. *Biochemistry*, 44(1):72–81, 2005.
- [28] Antonio Fittipaldi and Mauro Giacca. Transcellular protein transduction using the tat protein of hiv-1. *Advanced drug delivery reviews*, 57(4):597–608, 2005.
- [29] Ying Liu, Melina Jones, Cynthia M Hingtgen, Guojun Bu, Nick Laribee, Rudolph E Tanzi, Robert D Moir, Avindra Nath, and Johnny J He. Uptake of hiv-1 tat protein mediated by low-density lipoprotein receptor-related protein disrupts the neuronal metabolic balance of the receptor ligands. *Nature medicine*, 6(12):1380–1387, 2000.
- [30] Vladimir P Torchilin, Ram Rammohan, Volkmar Weissig, and Tatyana S Levchenko. Tat peptide on the surface of liposomes affords their efficient intracellular delivery even at low temperature and in the presence of metabolic inhibitors. *Proceedings of the National Academy of Sciences*, 98(15):8786–8791, 2001.
- [31] Vladimir P Torchilin, Tatyana S Levchenko, Ram Rammohan, Natalia Volodina, Brigitte Papahadjopoulos-Sternberg, and Gerard GM D’Souza. Cell transfection in vitro and in vivo with nontoxic tat peptide-liposome–dna complexes. *Proceedings of the National Academy of Sciences*, 100(4):1972–1977, 2003.
- [32] Carsten Rudolph, Christian Plank, James Lausier, Ulrike Schillinger, Rainer H Müller, and Joseph Rosenecker. Oligomers of the arginine-rich motif of the hiv-1 tat protein are capable of transferring plasmid dna into cells. *Journal of Biological Chemistry*, 278(13):11411–11418, 2003.
- [33] Ashok Chauhan, Akshay Tikoo, Arvinder K Kapur, and Mahavir Singh. The taming of the cell penetrating domain of the hiv tat: myths and realities. *Journal of Controlled Release*, 117(2):148–162, 2007.
- [34] JM Sabatier, E Vives, K Mabrouk, ABDELAZIZ Benjouad, H Rochat, A Duval, B Hue, and ELMOSTAFA Bahraoui. Evidence for neurotoxic activity of tat from human immunodeficiency virus type 1. *Journal of virology*, 65(2):961–967, 1991.

- [35] A. Mishra, V. D. Gordon, L. H. Yang, R. Coridan, and G. C. L. Wong. Hiv tat forms pores in membranes by inducing saddle-splay curvature: Potential role of bidentate hydrogen bonding. *Angewandte Chemie-International Edition*, 47(16):2986–2989, 2008.
- [36] S. T. Yang, E. Zaitseva, L. V. Chernomordik, and K. Melikov. Cell-penetrating peptide induces leaky fusion of liposomes containing late endosome-specific anionic lipid. *Biophysical Journal*, 99(8):2525–2533, 2010.
- [37] P. E. G. Thoren, D. Persson, E. K. Esbjorner, M. Goksor, P. Lincoln, and B. Norden. Membrane binding and translocation of cell-penetrating peptides. *Biochemistry*, 43(12):3471–3489, 2004.
- [38] SD Krämer and H Wunderli-Allenspach. No entry for tat (44–57) into liposomes and intact mdck cells: novel approach to study membrane permeation of cell-penetrating peptides. *Biochimica et Biophysica Acta (BBA)-Biomembranes*, 1609(2):161–169, 2003.
- [39] C. Ciobanasu, J. P. Siebrasse, and U. Kubitscheck. Cell-penetrating hiv1 tat peptides can generate pores in model membranes. *Biophysical Journal*, 99(1):153–62, 2010.
- [40] Philip A Gurnev, Sung-Tae Yang, Kamran C Melikov, Leonid V Chernomordik, and Sergey M Bezrukov. Cationic cell-penetrating peptide binds to planar lipid bilayers containing negatively charged lipids but does not induce conductive pores. *Biophysical journal*, 104(9):1933–1939, 2013.
- [41] H. D. Herce, A. E. Garcia, J. Litt, R. S. Kane, P. Martin, N. Enrique, A. Rebolledo, and V. Milesi. Arginine-rich peptides destabilize the plasma membrane, consistent with a pore formation translocation mechanism of cell-penetrating peptides. *Biophysical Journal*, 97(7):1917–1925, 2009.
- [42] Y. C. Su, A. J. Waring, P. Ruchala, and M. Hong. Membrane-bound dynamic structure of an arginine-rich cell-penetrating peptide, the protein transduction domain of hiv tat, from solid-state nmr. *Biochemistry*, 49(29):6009–6020, 2010.

- [43] S. Shojania and J. D. O’Neil. Hiv-1 tat is a natively unfolded protein - the solution conformation and dynamics of reduced hiv-1 tat-(1-72) by nmr spectroscopy. *Journal of Biological Chemistry*, 281(13):8347–8356, 2006.
- [44] P. Bayer, M. Kraft, A. Ejchart, M. Westendorp, R. Frank, and P. Rosch. Structural studies of hiv-1 tat protein. *Journal of Molecular Biology*, 247(4):529–535, 1995.
- [45] H. D. Herce and A. E. Garcia. Molecular dynamics simulations suggest a mechanism for translocation of the hiv-1 tat peptide across lipid membranes. *Proceedings of the National Academy of Sciences of the United States of America*, 104(52):20805–20810, 2007.
- [46] S. Yesylevskyy, S. J. Marrink, and A. E. Mark. Alternative mechanisms for the interaction of the cell-penetrating peptides penetratin and the tat peptide with lipid bilayers. *Biophysical Journal*, 97(1):40–49, 2009.
- [47] SL Barna, MW Tate, SM Gruner, and EF Eikenberry. Calibration procedures for charge-coupled device x-ray detectors. *Review of Scientific Instruments*, 70(7):2927–2934, 1999.
- [48] Y. Lyatskaya, Y. F. Liu, S. Tristram-Nagle, J. Katsaras, and J. F. Nagle. Method for obtaining structure and interactions from oriented lipid bilayers. *Physical Review E*, 63(1):0119071–0119079, 2001.
- [49] Y. F. Liu and J. F. Nagle. Diffuse scattering provides material parameters and electron density profiles of biomembranes. *Physical Review E*, 69(4):040901–040904(R), 2004.
- [50] Yufeng Liu. *NEW METHOD TO OBTAIN STRUCTURE OF BIOMEMBRANES USING DIFFUSE -RAY SCATTERING: APPLICATION TO FLUID PHASE DOPC LIPID BILAYERS*. PhD thesis, Carnegie Mellon University, 2003.
- [51] John F Nagle and Stephanie Tristram-Nagle. Structure of lipid bilayers. *Biochimica et Biophysica Acta (BBA)-Reviews on Biomembranes*, 1469(3):159–195, 2000.

- [52] Norbert Kuerka, John F. Nagle, Jonathan N. Sachs, Scott E. Feller, Jeremy Pencer, Andrew Jackson, and John Katsaras. Lipid bilayer structure determined by the simultaneous analysis of neutron and x-ray scattering data. *Biophysical Journal*, 95(5):2356 – 2367, 2008.
- [53] Stephanie Tristram-Nagle, Yufeng Liu, Justin Legleiter, and John F. Nagle. Structure of gel phase DMPC determined by x-ray diffraction. *Biophysical Journal*, 83(6):3324 – 3335, 2002.
- [54] Anthony R. Braun, Jonathan N. Sachs, and John F. Nagle. Comparing simulations of lipid bilayers to scattering data: The gromos 43a1-s3 force field. *The Journal of Physical Chemistry B*, 117(17):5065–5072, 2013.
- [55] <http://seal.web.cern.ch/seal/documents/minuit/mnusersguide.pdf>.
- [56] <http://lcgapp.cern.ch/project/cls/work-packages/mathlibs/minuit/index.html>.
- [57] Berk Hess, Carsten Kutzner, David van der Spoel, and Erik Lindahl. Gromacs 4: Algorithms for highly efficient, load-balanced, and scalable molecular simulation. *Journal of Chemical Theory and Computation*, 4(3):435–447, 2008.
- [58] Joakim P. M. Jmbeck and Alexander P. Lyubartsev. Derivation and systematic validation of a refined all-atom force field for phosphatidylcholine lipids. *The Journal of Physical Chemistry B*, 116(10):3164–3179, 2012.
- [59] Joakim P. M. Jmbeck and Alexander P. Lyubartsev. An extension and further validation of an all-atomistic force field for biological membranes. *Journal of Chemical Theory and Computation*, 8(8):2938–2948, 2012.
- [60] Viktor Hornak, Robert Abel, Asim Okur, Bentley Strockbine, Adrian Roitberg, and Carlos Simmerling. Comparison of multiple amber force fields and development of improved protein backbone parameters. *Proteins: Structure, Function, and Bioinformatics*, 65(3):712–725, 2006.
- [61] W. L. Jorgensen, J. Chandrasekhar, J. D. Madura, R. W. Impey, and M. L. Klein. Comparison of simple potential functions for simulating liquid water. *Journal of Chemical Physics*, 79(2):926–935, 1983.

- [62] Norbert Kuerka, John Katsaras, and JohnF. Nagle. Comparing membrane simulations to scattering experiments: Introducing the simtoexp software. *Journal of Membrane Biology*, 235(1):43–50, 2010.
- [63] Shuichi Miyamoto and Peter A Kollman. Settle: an analytical version of the shake and rattle algorithm for rigid water models. *Journal of computational chemistry*, 13(8):952–962, 1992.
- [64] B. Hess, H. Bekker, H. J. C. Berendsen, and J. G. E. M. Fraaije. Lincs: A linear constraint solver for molecular simulations. *J Comput Chem*, 18(12):1463–1472, 1997.
- [65] Tom Darden, Darrin York, and Lee Pedersen. Particle mesh ewald: An $n \log(n)$ method for ewald sums in large systems. *The Journal of chemical physics*, 98(12):10089–10092, 1993.
- [66] Giovanni Bussi, Davide Donadio, and Michele Parrinello. Canonical sampling through velocity rescaling. *The Journal of chemical physics*, 126(1):014101, 2007.
- [67] Michele Parrinello and Aneesur Rahman. Polymorphic transitions in single crystals: A new molecular dynamics method. *Journal of Applied physics*, 52(12):7182–7190, 1981.
- [68] Norbert Kučerka, Yufeng Liu, Nanjun Chu, Horia I Petrache, Stephanie Tristram-Nagle, and John F Nagle. Structure of fully hydrated fluid phase DMPC and DLPC lipid bilayers using X-ray scattering from oriented multilamellar arrays and from unilamellar vesicles. *Biophysical journal*, 88(4):2626–2637, 2005.
- [69] Norbert Kučerka, Stephanie Tristram-Nagle, and John F Nagle. Closer look at structure of fully hydrated fluid phase dppc bilayers. *Biophysical journal*, 90(11):L83–L85, 2006.
- [70] Norbert Kučerka, Stephanie Tristram-Nagle, and John F Nagle. Structure of fully hydrated fluid phase lipid bilayers with monounsaturated chains. *The Journal of membrane biology*, 208(3):193–202, 2005.

- [71] Stephanie Tristram-Nagle, Chao-Ping Yang, and John F Nagle. Thermodynamic studies of purple membrane. *Biochimica et Biophysica Acta (BBA)-Biomembranes*, 854(1):58–66, 1986.
- [72] <http://www.basic.northwestern.edu/biotools/proteinCalc.html>.
- [73] A. C. V. Johansson and E. Lindahl. The role of lipid composition for insertion and stabilization of amino acids in membranes. *Journal of Chemical Physics*, 130(18), 2009.
- [74] S. Tristram-Nagle and J. F. Nagle. Hiv-1 fusion peptide decreases bending energy and promotes curved fusion intermediates. *Biophysical Journal*, 93(6):2048–2055, 2007.
- [75] L. B. Li, I. Vorobyov, and T. W. Allen. Potential of mean force and pk(a) profile calculation for a lipid membrane-exposed arginine side chain. *Journal of Physical Chemistry B*, 112(32):9574–9587, 2008.
- [76] I. Vorobyov, L. B. Li, and T. W. Allen. Assessing atomistic and coarse-grained force fields for protein-lipid interactions: The formidable challenge of an ionizable side chain in a membrane. *Journal of Physical Chemistry B*, 112(32):9588–9602, 2008.
- [77] J. L. MacCallum, W. F. D. Bennett, and D. P. Tieleman. Distribution of amino acids in a lipid bilayer from computer simulations. *Biophysical Journal*, 94(9):3393–3404, 2008.
- [78] E. V. Schow, J. A. Freites, P. Cheng, A. Bernsel, G. von Heijne, S. H. White, and D. J. Tobias. Arginine in membranes: The connection between molecular dynamics simulations and translocon-mediated insertion experiments. *Journal of Membrane Biology*, 239(1-2):35–48, 2011.
- [79] W. C. Wimley, T. P. Creamer, and S. H. White. Solvation energies of amino acid side chains and backbone in a family of host-guest pentapeptides. *Biochemistry*, 35(16):5109–5124, 1996.
- [80] W. C. Wimley and S. H. White. Experimentally determined hydrophobicity scale for proteins at membrane interfaces. *Nature Structural Biology*, 3(10):842–848, 1996.

- [81] B. Roux. Lonely arginine seeks friendly environment. *Journal of General Physiology*, 130(2):233–236, 2007.
- [82] W. Kabsch and C. Sander. Dictionary of protein secondary structure: pattern recognition of hydrogen-bonded and geometrical features. *Biopolymers*, 22(12):2577–637, 1983.
- [83] D. Choi, J. H. Moon, H. Kim, B. J. Sung, M. W. Kim, G. Y. Tae, S. K. Satija, B. Akgun, C. J. Yu, H. W. Lee, D. R. Lee, J. M. Henderson, J. W. Kwong, K. L. Lam, K. Y. C. Lee, and K. Shin. Insertion mechanism of cell-penetrating peptides into supported phospholipid membranes revealed by x-ray and neutron reflection. *Soft Matter*, 8(32):8294–8297, 2012.
- [84] K. Huang and A. E. Garcia. Free energy of translocating an arginine-rich cell-penetrating peptide across a lipid bilayer suggests pore formation. *Biophysical Journal*, 104(2):412–420, 2013.
- [85] Martin J. Janiak, Donald M. Small, and G. Graham Shipley. Nature of the thermal pretransition of synthetic phospholipids: dimyristoyl- and dipalmitoyl-lecithin. *Biochemistry*, 15(21):4575–4580, 1976.
- [86] Martin J Janiak, Donald M Small, and G Graham Shipley. Temperature and compositional dependence of the structure of hydrated dimyristoyl lecithin. *Journal of Biological Chemistry*, 254(13):6068–6078, 1979.
- [87] Haruhiko Yao, Sinzi Matuoka, Boris Tenchov, and Ichiro Hatta. Metastable ripple phase of fully hydrated dipalmitoylphosphatidylcholine as studied by small angle x-ray scattering. *Biophysical journal*, 59(1):252–255, 1991.
- [88] W J Sun, S Tristram-Nagle, R M Suter, and J F Nagle. Structure of the ripple phase in lecithin bilayers. *Proceedings of the National Academy of Sciences*, 93(14):7008–7012, 1996.
- [89] Beth A Cunningham, Ari-David Brown, David H Wolfe, W Patrick Williams, and Anthony Brain. Ripple phase formation in phosphatidylcholine: Effect of acyl chain relative length, position, and unsaturation. *Physical Review E*, 58(3):3662, 1998.

- [90] Kell Mortensen, Walter Pfeiffer, Erich Sackmann, and Wolfgang Knoll. Structural properties of a phosphatidylcholine-cholesterol system as studied by small-angle neutron scattering: ripple structure and phase diagram. *Biochimica et Biophysica Acta (BBA)-Biomembranes*, 945(2):221–245, 1988.
- [91] Jeremy P Bradshaw, Michael S Edenborough, Philip JH Sizer, and Anthony Watts. Observation of rippled dioleoylphosphatidylcholine bilayers by neutron diffraction. *Biochimica et Biophysica Acta (BBA)-Biomembranes*, 987(1):111–114, 1989.
- [92] JT Woodward IV and JA Zasadzinski. Amplitude, wave form, and temperature dependence of bilayer ripples in the p β phase. *Physical Review E*, 53(4):R3044, 1996.
- [93] PC Mason, BD Gaulin, RM Epand, GD Wignall, and JS Lin. Small angle neutron scattering and calorimetric studies of large unilamellar vesicles of the phospholipid dipalmitoylphosphatidylcholine. *Physical Review E*, 59(3):3361, 1999.
- [94] M. P. Hentschel and F. Rustichelli. Structure of the ripple phase P'_β in hydrated phosphatidylcholine multimembranes. *Phys. Rev. Lett.*, 66:903–906, Feb 1991.
- [95] John Katsaras, Stephanie Tristram-Nagle, Yufeng Liu, RL Headrick, E Fontes, PC Mason, and John F Nagle. Clarification of the ripple phase of lecithin bilayers using fully hydrated, aligned samples. *Physical Review E*, 61(5):5668, 2000.
- [96] Kheya Sengupta, V. A. Raghunathan, and John Katsaras. Structure of the ripple phase of phospholipid multibilayers. *Phys. Rev. E*, 68:031710, Sep 2003.
- [97] Li Li and Ji-Xin Cheng. Coexisting stripe-and patch-shaped domains in giant unilamellar vesicles. *Biochemistry*, 45(39):11819–11826, 2006.
- [98] Alex H. de Vries, Serge Yefimov, Alan E. Mark, and Siewert J. Marrink. Molecular structure of the lecithin ripple phase. *Proceedings of the National Academy of Sciences of the United States of America*, 102(15):5392–5396, 2005.
- [99] Olaf Lenz and Friederike Schmid. Structure of symmetric and asymmetric “ripple” phases in lipid bilayers. *Phys. Rev. Lett.*, 98:058104, Jan 2007.

- [100] C-M Chen, TC Lubensky, and FC MacKintosh. Phase transitions and modulated phases in lipid bilayers. *Physical Review E*, 51(1):504, 1995.
- [101] J. Katsaras and V. A. Raghunathan. Molecular chirality and the ripple phase of phosphatidylcholine multibilayers. *Phys. Rev. Lett.*, 74:2022–2025, Mar 1995.
- [102] S. A. Tristram-Nagle. Preparation of oriented, fully hydrated lipid samples for structure determination using x-ray scattering. *Methods Mol Biol*, 400:63–75, 2007.
- [103] http://henke.lbl.gov/optical_constants.
- [104] M.C. Wiener, R.M. Suter, and J.F. Nagle. Structure of the fully hydrated gel phase of dipalmitoylphosphatidylcholine. *Biophysical Journal*, 55(2):315 – 325, 1989.
- [105] Thalia T Mills, Gilman ES Toombes, Stephanie Tristram-Nagle, Detlef-M Smilgies, Gerald W Feigenson, and John F Nagle. Order parameters and areas in fluid-phase oriented lipid membranes using wide angle x-ray scattering. *Biophysical journal*, 95(2):669–681, 2008.
- [106] George H Vineyard. Grazing-incidence diffraction and the distorted-wave approximation for the study of surfaces. *Physical Review B*, 26(8):4146, 1982.
- [107] CE Miller, J Majewski, EB Watkins, DJ Mulder, T Gog, and TL Kuhl. Probing the local order of single phospholipid membranes using grazing incidence x-ray diffraction. *Physical review letters*, 100(5):058103, 2008.
- [108] S Tristram-Nagle, R Zhang, RM Suter, CR Worthington, WJ Sun, and JF Nagle. Measurement of chain tilt angle in fully hydrated bilayers of gel phase lecithins. *Biophysical journal*, 64(4):1097–1109, 1993.
- [109] Bertram Eugene Warren. *X-ray Diffraction*. Courier Dover Publications, 1969.
- [110] W-J Sun, RM Suter, MA Knewton, CR Worthington, S Tristram-Nagle, R Zhang, and JF Nagle. Order and disorder in fully hydrated unoriented bilayers of gel-phase dipalmitoylphosphatidylcholine. *Physical Review E*, 49(5):4665, 1994.

- [111] Alejandro B. Rodriguez-Navarro. Registering pole figures using an X-ray single-crystal diffractometer equipped with an area detector. *Journal of Applied Crystallography*, 40(3):631–634, Jun 2007.
- [112] Jessy L. Baker, Leslie H. Jimison, Stefan Mannsfeld, Steven Volkman, Shong Yin, Vivek Subramanian, Alberto Salleo, A. Paul Alivisatos, and Michael F. Toney. Quantification of thin film crystallographic orientation using x-ray diffraction with an area detector. *Langmuir*, 26(11):9146–9151, 2010. PMID: 20361783.